

# Chapter 4

## Multi-scale modelling of dry granular flows

### 4.1 Introduction

The dynamics of a homogeneous granular flow involve at least three distinct scales: the *microscopic scale*, which is characterised by the contact between grains, the *meso-scale* that represents micro-structural effects such as grain rearrangement, and the *macroscopic scale*, where geometric correlations can be observed (see Figure 4.1). Conventionally, granular flows are modelled as a continuum because they exhibit many collective phenomena. However, on a grain scale, the granular materials exhibit complex solid-like and/or fluid-like behaviour. Recent studies, however, suggest that a continuum law may be unable to capture the effect of inhomogeneities at the grain scale level, such as orientation of force chains, which are micro-structural effects. Discrete element methods (DEM) are capable of simulating these micro-structural effects, however they are computationally expensive. In the present study, a multi-scale approach is adopted, using both DEM and continuum techniques, to better understand the rheology of granular flows and the limitations of continuum models.

### 4.2 Granular column collapse

The collapse of a granular column on a horizontal surface is a simple case of granular flow, however a proper model that describes the flow dynamics is still lacking. Granular flow is modelled as a frictional dissipation process in continuum mechanics but studies showing the lack of influence of inter-particle friction on the energy dissipation and spreading dynamics is surprising. In the present study, the generalised interpolation material point method (GIMPM),

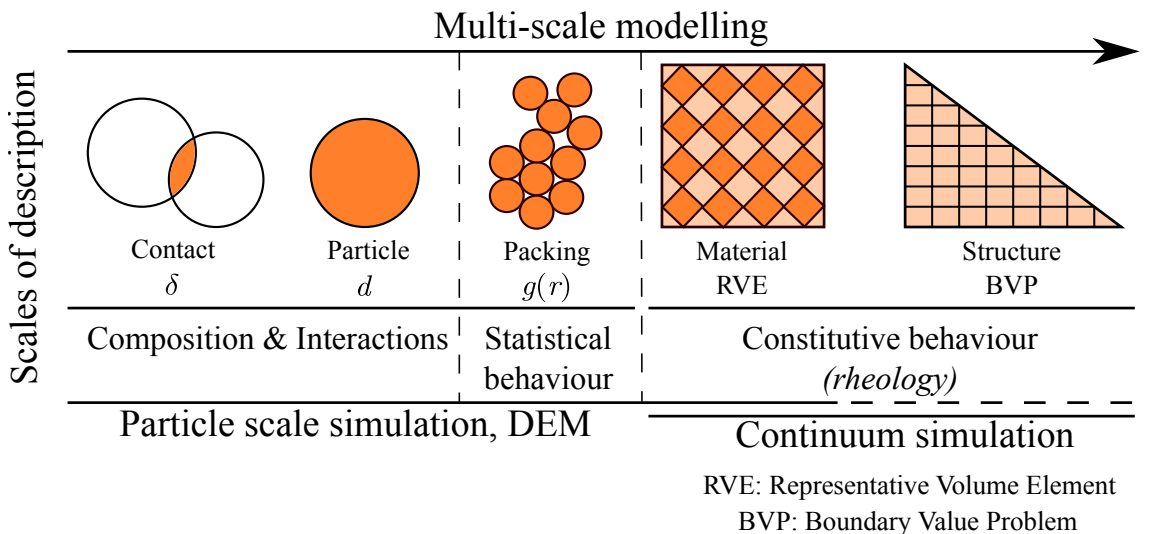


Figure 4.1 Multi-scale modelling of granular materials

- <sup>1</sup> a hybrid Eulerian – Lagrangian approach, is implemented with Mohr-Coloumb failure criterion
- <sup>2</sup> to describe the continuum behaviour of quasi-two dimensional collapse of granular columns.
- <sup>3</sup> The granular column collapse is also simulated using DEM to understand the micro-mechanics
- <sup>4</sup> of the flow.

<sup>5</sup> The granular column collapse experiment involves filling a cylinder of height  $H_0$  and width  
<sup>6</sup>  $L_0$  with a granular material of mass ‘m’. The granular column is then released *en masse*  
<sup>7</sup> by quickly removing the cylinder, thus allowing the granular material to collapse onto the  
<sup>8</sup> horizontal surface, forming a deposit having a final height  $H_f$  and radius  $L_f$ . A computational  
<sup>9</sup> study on an equivalent two-dimensional configuration (circular disks) was carried out using  
<sup>10</sup> Discrete Element and Continuum (MPM) approaches.

<sup>11</sup> Lajeunesse et al. (2004) performed axis-symmetric and plane strain tests on granular  
<sup>12</sup> column collapse. Granular materials when released suddenly on a horizontal surface exhibit  
<sup>13</sup> transient flow. The mechanism of flow initiation, spreading dynamics and energy dissipation  
<sup>14</sup> are studied. The experimental configuration used by Lajeunesse et al. (2004) is shown in  
<sup>15</sup> Figure 4.2. Granular material of mass ‘M’ was poured into a container to form a rectangular  
<sup>16</sup> heap of length ‘ $L_i$ ’, height ‘ $H_i$ ’ and thickness ‘W’. The internal friction angle and the wall  
<sup>17</sup> friction between the wall and the glass beads measured by Lajeunesse et al. (2004) are listed  
<sup>18</sup> in Table 4.1. The gate was then quickly removed to release the granular mass that spreads in  
<sup>19</sup> the horizontal channel until it comes to rest. The final run-out distance ‘ $L_f$ ’ and the collapsed  
<sup>20</sup> height ‘ $H_f$ ’ were measured. The run-out distance and collapse height were found to exhibit  
<sup>21</sup> power law relation with the initial aspect ratio ‘ $a$ ’ ( $= H_i/L_i$ ) of the column.

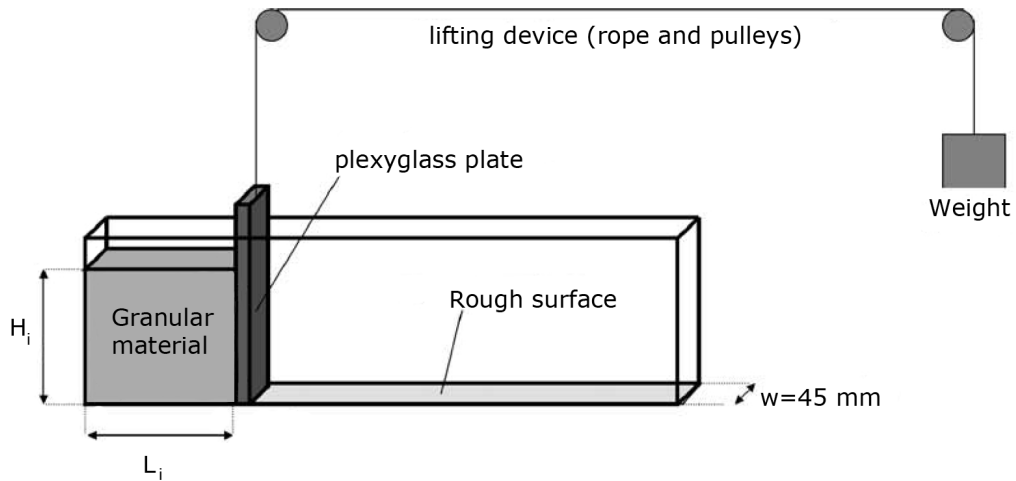


Figure 4.2 Schematic of experimental configuration for 2-D collapse in a rectangular channel, ([Lajeunesse et al., 2004](#))

Table 4.1 Material properties of glass ballotini, ([Lajeunesse et al., 2004](#))

Parameter	Value
Mean diameter	1.15 mm
Repose angle	$22 \pm 0.5^\circ$
Avalanche angle	$27.4 \pm 0.5^\circ$
Wall friction angle	$24.8 \pm 0.2^\circ$

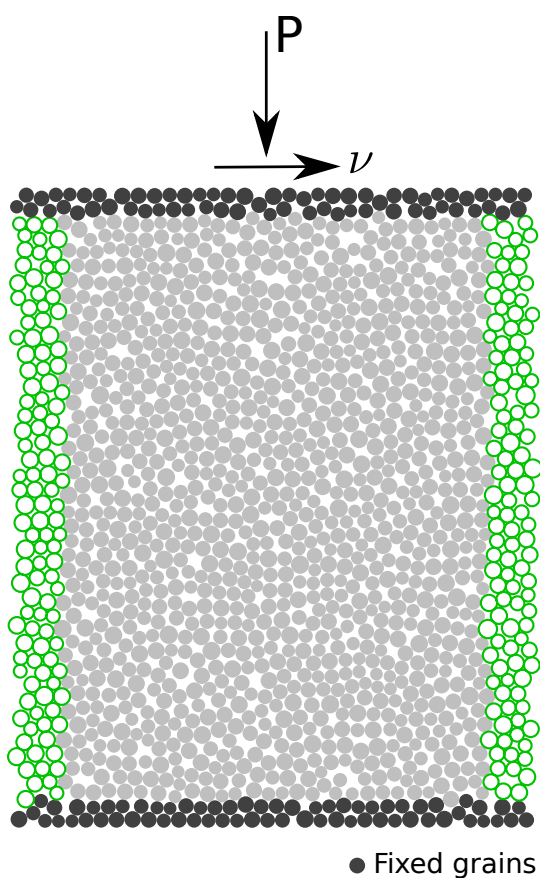


Figure 4.3 Shear test periodic boundary condition

In this study, numerical simulations of the granular column collapse experiments are performed by varying the initial aspect ratio of the column. Discrete Element Method simulations involve modelling the granular column as individual particles. The granular column is prepared by randomly packing poly-disperse grains on a regular lattice and allowing them to undergo free fall due to gravity, forming a randomly packed granular column (see

Krishna Kumar Soundararajan: Add Chapter reference

The grains are allowed to reach a stable equilibrium after undergoing some elastic compressions due to gravity. The overlaps between particles are determined by the stiffness  $k_n$  of the spring in the normal direction. Typically, average overlaps in the range 0.1 to 1.0% are desirable and the spring constant is chosen to produce particle overlaps in this range. The stiffness is determined using the following equation:

$$k_n = \frac{2\pi G}{(1-\nu)[2\ln(\frac{2r}{A}) - 1]} \quad (4.1)$$

$$A = \left[ \frac{2r(1-\nu)f_n}{\pi G} \right]^{\frac{1}{2}} \quad (4.2)$$

where  $f_n$  is the normal contact force;  $G$  is the shear modulus;  $\nu$  is the Poisson's ratio and  $r$  is the radius of the grain. A simpler form of stiffness for a spherical grain is defined as:

$$k_n = 4ER \quad (4.3)$$

where  $E$  is the Young's modulus of the material and  $R$  is the radius of the grain. The normal damping coefficient  $C_n$  is chosen to give a required coefficient of restitution  $\varepsilon$  (defined as the ratio of the post-collisional to pre-collisional normal component of the relative velocity) for the materials involved:

$$C_n = 2\gamma\sqrt{m_{ij}k_n} \quad (4.4)$$

$$\text{where } \gamma = -\frac{\ln(\varepsilon)}{\sqrt{\pi^2 + \ln^2(\varepsilon)}}, \quad \text{and} \quad m_{ij} = \frac{m_i m_j}{m_i + m_j} \quad (4.5)$$

Discrete Element Method simulations were carried out with columns having different initial aspect ratio ' $a$ ', varying from 0.2 to 10. In order to study the effect of crystallisation on the run-out distance, 10 more MD simulations were carried out on granular columns composed of grains arranged on a hexagonal lattice. In order to maintain a threshold amount of grains, in all the cases the columns contain at least 1000 grains, which is the safe lower limit for DEM as suggested by [Oda and Iwashita \(1999\)](#). The micro-mechanical parameters used in this study are presented in Table 4.2. Due to the unsteady nature of the flow, the grains get dispersed on

Table 4.2 Micromechanical parameters used in Discrete Element Method simulations

Parameter	Value
Young's modulus of glass bead	$70 \times 10^9 \text{ N m}^{-2}$
Poisson's ratio	0.22 - 0.24
Diameter of glass beads	0.92 to 1.38 mm
Normal and shear stiffness of grains	$1.6 \times 10^8 \text{ N m}^{-1}$
Normal and shear stiffness of wall	$4 \times 10^8 \text{ N m}^{-1}$
Inter-particle friction coefficient, $\mu$	0.53
Wall friction coefficient	0.466
Coefficient of restitution, $\Gamma$	0.6

Table 4.3 Parameters used in continuum simulations

Parameter	Value
Number of material points representing an actual particle	4
Material point spacing	0.575 mm
Number of material points per mesh	16
Young's Modulus, E	$1.98 \times 10^6 \text{ Pa}$
Poisson's ratio, $\nu$	0.22 to 0.24
Friction angle, $\phi$	$23.0^\circ$
Dilatancy angle, $\Phi$	$0^\circ$
Density, $\rho$	$1800 \text{ kg m}^{-3}$
Wall friction	0.466
Time step increment	$1.0 \times 10^{-6} \text{ s}$

- <sup>1</sup> the horizontal plane as discrete bodies start to separate from the main mass, hence the run-out  
<sup>2</sup> distance is calculated as the position of the farthest grain which has at least one contact with the  
<sup>3</sup> main mass. A plane strain collapse of granular column is simulated as a continuum using MPM.  
<sup>4</sup> The effect of number of material points on the accuracy of the simulation was discussed in  
<sup>5</sup> Chapter 4. [Guilkey et al. \(2003\)](#) suggests at least four particles per cell for problems involving  
<sup>6</sup> large deformations. 10 MPM simulations of the granular column collapse were performed using  
<sup>7</sup> Mohr-Coulomb constitutive law by varying the initial aspect ratio, to understand the difference  
<sup>8</sup> between the particle and continuum scale description of granular flows. The parameters used  
<sup>9</sup> for the continuum analyses are presented in Table. 4.3. The Young's modulus of the granular  
<sup>10</sup> assembly is determined by performing a uni-axial compression of the granular column in  
<sup>11</sup> Discrete Element Method.

### 4.2.1 Deposit morphology

The variation of the normalized final run-out distance,  $\Delta L = (L_f - L_i)/L_i$ , with the initial aspect ratio ‘a’ of the column is presented in Figure 4.4. Similar to the experimental results, a power law relationship is observed between the normalized run-out distance and the initial aspect ratio of the column. However, the molecular dynamics simulations with random packing of grains overestimate the run-out distance by a factor of 1.2. In the present study, the following scaling law for the run-out is observed.

$$\frac{L_f - L_i}{L_i} \approx \begin{cases} 1.67a, & a \lesssim 2.3 \\ 2.5a^{2/3}, & a \gtrsim 2.3 \end{cases} \quad (4.6)$$

The run-out distance observed in the case of hexagonal packing of grains matches the experimental run-out distance observed by [Lajeunesse et al. \(2004\)](#). However, the Discrete Element Method simulations performed with random packing predict longer run-out distances in comparison with the experimental data. The difference in the run-out distance can be attributed to the variation in the packing of grains in the granular column. Although, experimental data corresponds to granular column collapse in a rectangular channel, the collapse is not a pure two-dimensional collapse as in the case of numerical simulations. This can cause some variation in the run-out distance. [Balmforth and Kerswell \(2005\)](#) observed that the material property affects the final run-out distance and included a pre-factor ‘ $\lambda$ ’ in the scaling law, which is in contrast to the observation made by [Lube et al. \(2005\)](#). The scaling law observed in the present study for the random packing is identical to the scaling law observed by [Lajeunesse et al. \(2004\)](#), except for the pre-factor in the scaling law, indicating a strong correlation between the run-out distance and the material property. [Daerr and Douady \(1999\)](#) also observed the effect of initial packing density and the internal structure on the behaviour of granular flows. The continuum description of the granular column collapse using Material Point Method shows good agreement with the experimental results for columns with lower aspect ratio (‘ $a$ ’  $\lesssim 2.3$ ), however it exhibits a significant increase in the run-out distance beyond the aspect ratio of 2.3. [Bandara \(2013\)](#) also observed a jump in the run-out distance at the initial aspect ratio of 2.

In order to understand the mechanism of the run-out in a granular column collapse, it is essential to study the relation between the final collapsed height of the granular column and its initial aspect ratio. Figure 4.5 shows the variation of the normalized final height with the initial aspect ratio of the column. The final height predicted by the Discrete Element Method and the MPM simulations matches the experimental data for granular columns with aspect ratio below 0.7, which indicates that the initial density of the column has negligible effect on the final collapse height. The scaling of final height of the column with the initial aspect ratio of

1 the column can be written as:

$$2 \quad \frac{H_f}{L_i} \propto \begin{cases} a, & a \lesssim 0.7 \\ 3 \quad a^{2/3}, & a \gtrsim 0.7 \end{cases} \quad (4.7)$$

4 The Material Point Method predicts a higher final height of the column in comparison with  
5 the particular simulations that should result in shorter run-outs, however it is inconsistent with  
6 the observations. In case of granular columns with smaller aspect ratios, only a tiny portion of  
7 the total mass is mobilized and the rest remains static, thus predicting the final collapse height  
8 accurately. The final height of a column is controlled by the amount of static region in the  
9 granular column collapse, while the run-out distance is essentially a function of the flowing  
10 mass. Hence, it is essential to compare the evolution of flow and the internal flow structure  
11 in the Discrete Element Method and Material Point Method simulations to understand the  
12 limitations of both the continuum and discrete element approaches.

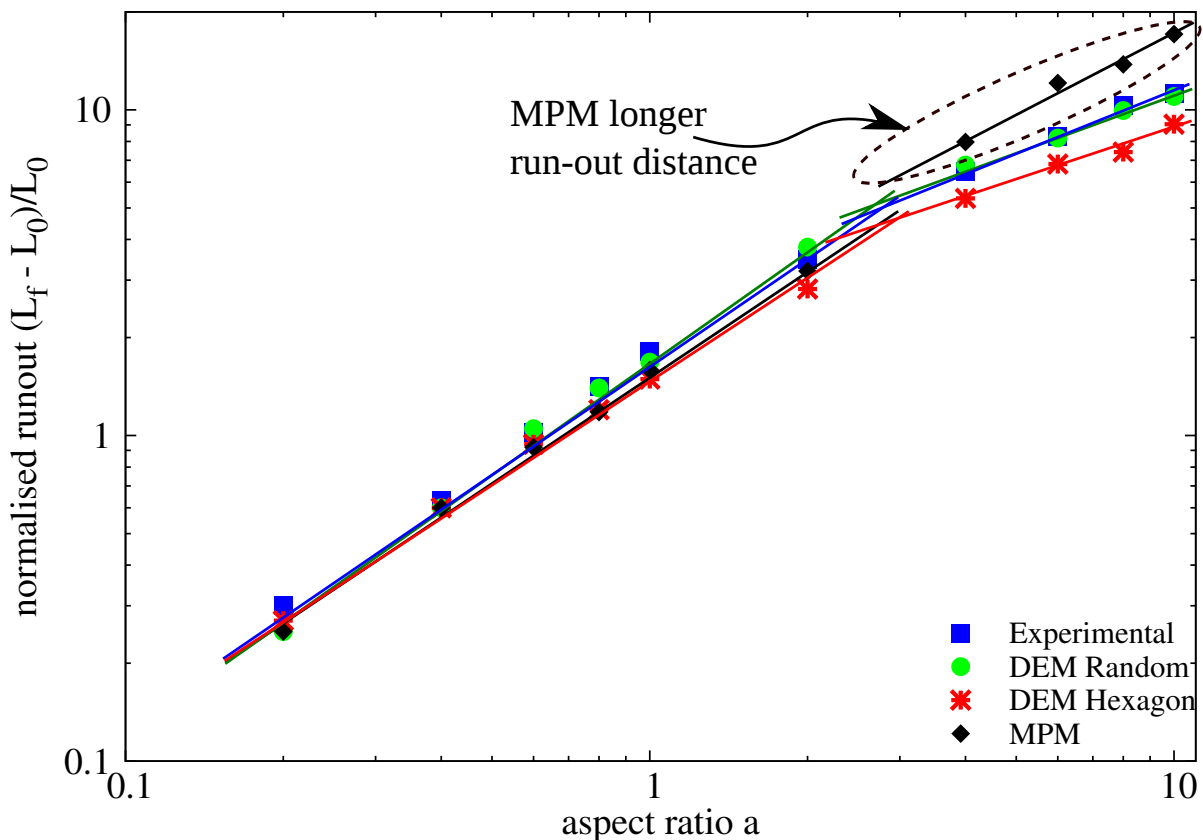


Figure 4.4 Normalised final run-out distance for columns with different initial aspect ratio

## 4.2 Granular column collapse

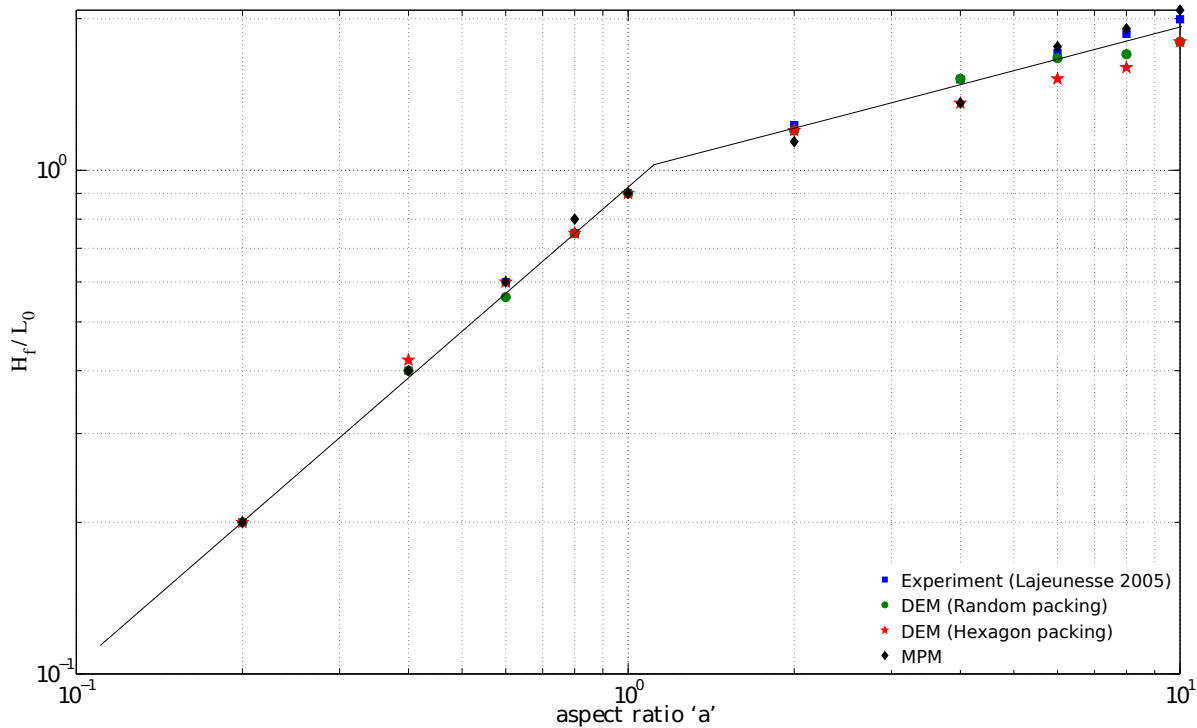


Figure 4.5 Normalised final collapse height for columns with different initial aspect ratio

### 4.2.2 Flow evolution and internal flow structure

For a fixed granular material and substrate properties, the flow dynamics and the final deposit morphology do not depend on the volume of granular material released, but depend only on the aspect ratio ‘ $a$ ’ of the column. A power law relationship is observed between the run-out distance and the initial aspect ratio of the column. A transition in the run-out behaviour at an aspect ratio of 2.3 indicates a change in the flow dynamics. For smaller aspect ratios, the granular mass fails through avalanching of flanks producing a truncated cone-like deposit ( $‘a’ < 0.7$ ) or conical deposit ( $‘a’ > 0.7$ ). At smaller values of aspect ratios, the flow is initiated by failure at the edge of the pile along a well-defined fracture surface. The grains located above the failure surface move “*en masse*” leaving a static region underneath the failure surface. After a transient time of order  $\tau_c$ , defined as  $\sqrt{H_i/g}$ , the flow is fully developed. The velocity profile along the granular column at critical time  $\tau_c$  is presented in Figure 4.6. At critical time, the velocity field depends only on the position of the grain along the sliding mass. The maximum velocity is observed at the front of the flowing mass corresponding to that of a plug flow in horizontal direction. Particulate and continuum simulations yield similar run-out distance at critical time. Unlike particulate simulations, the Material point method predicts that the maximum horizontal velocity occurs at the top of the sliding mass. Behind the fast flowing

front, the flow is localized in the mass above the failure surface and the velocity profiles are locally parallel to the failure plane. The flow is composed of upper linear part and a lower exponential tail in the static granular bed. The velocity profile is similar to steady granular surface flow as observed by [Lajeunesse et al. \(2004\)](#).

For columns with lower initial aspect ratios, the run-out distance is proportional to the mass flowing above the failure surface. To understand the amount of mass mobilized during a collapse, the angle of the failure surface has to be studied. Figure 4.6 shows a distinct failure surface when the flow is fully developed at critical time  $\tau_c$ . The angle of the failure surface is found to be about  $55^\circ$ . The failure surface begins from the toe of the column and protrudes inwards at an angle of  $50$  to  $55^\circ$ . For columns with lower aspect ratios, the formation of the “truncated conical deposit” or “conical deposit” depends only on the initial length of the column, as the angle of the failure surface is found to be independent of the aspect ratio. The failure angle is consistent with the interpretation in terms of *active Coulomb failure* ([Lajeunesse et al., 2004](#)), which leads to a predicted failure angle  $\theta_y = 45^\circ + \delta/2$ , where  $\delta$  is the internal friction angle of the granular material. In the present study, the friction angle of the glass beads is  $22^\circ$ , which leads to  $\theta_y = 45^\circ + 22^\circ/2 = 56^\circ$ , which is in good agreement with the numerical simulations and experimental observations by [Lajeunesse et al. \(2004\)](#). Contrary to the suggestion of [Lajeunesse et al. \(2004\)](#), the fracture angle is found to have no direct effect on the transition between the truncated cone and the conical deposit occurring at an aspect ratio of 0.7. [Schaefer \(1990\)](#) observed the onset of instabilities in a narrow wedges of  $56$  to  $65^\circ$  for Cambridge type constitutive models that describes granular flows. This observation matches well with the failure angle observed in the present study. The final profile of the collapsed granular column with an initial aspect ratio of 0.4 is shown in Figure 4.7. The failure surface is distinct and the hexagonal dense packing of grains has a steeper failure surface in comparison with the random packing. The variation observed in the angle of the failure surface causes a difference in the amount of mobilized mass above the failure surface, and in turn in the run-out distance. The lower value of run-out distance observed in the case of hexagonal packing of grains can be attributed to the crystallisation effects. crystallisation is the formation of large-scale lattice structures during the flow, resulting in non-generic flow patterns. crystallisation is found to have a significant effect on the final state of the granular column. [Lacaze and Kerswell \(2009\)](#) observed that poly-disperse grains have lesser tendency to crystallize especially in the case of columns with larger aspect ratio.

For larger aspect ratios, the flow is still initiated by a well defined failure surface as can be seen in Figure 4.8. However, in this case the initial granular column is much higher than the top of the failure surface. Due to gravity most of the grains in the column fall in the vertical direction consuming the column along their way. When they reach the vicinity of the failure

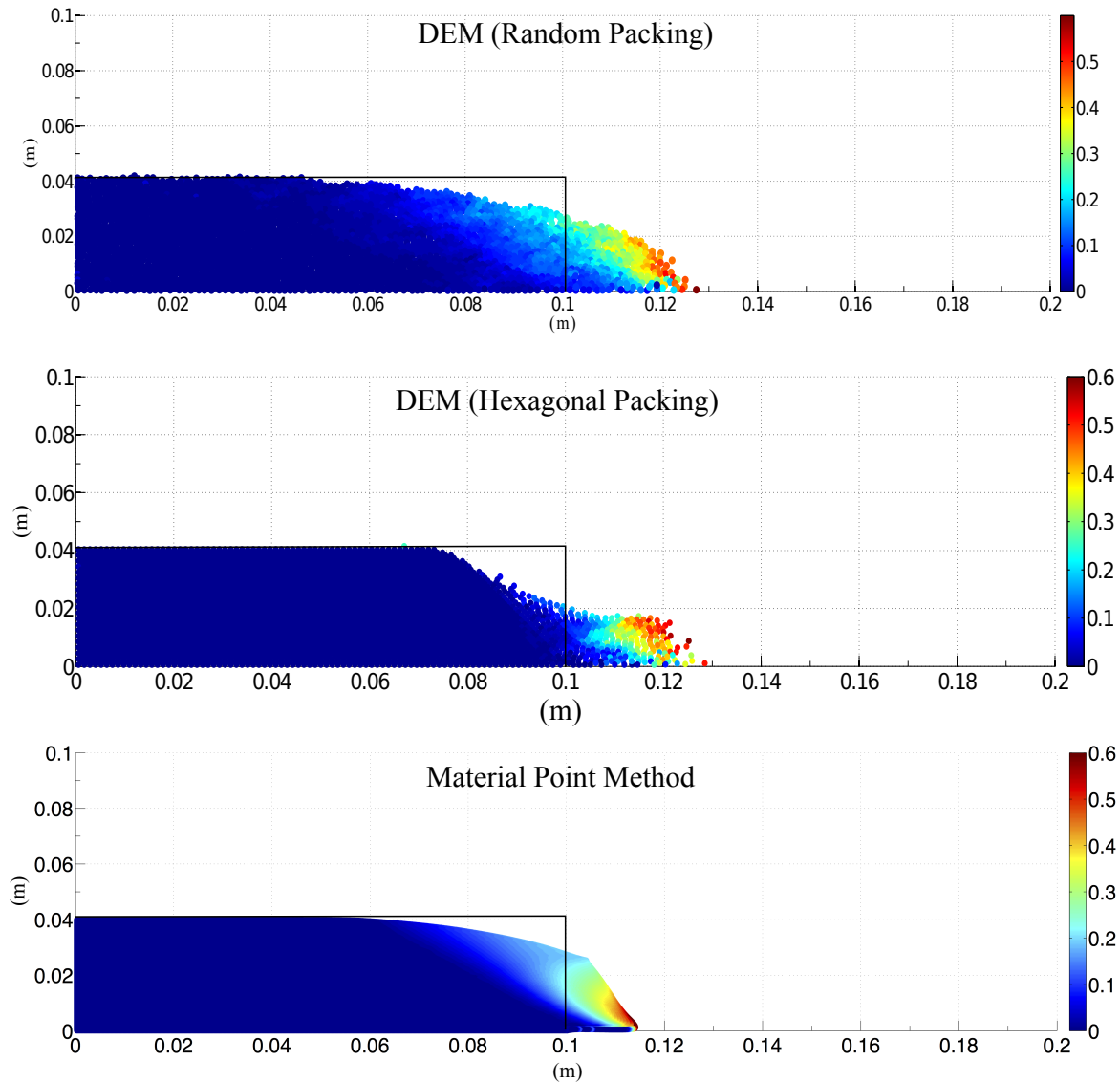


Figure 4.6 Velocity profile of a granular column collapse ( $a' = 0.4 \& t = \tau_c$ )

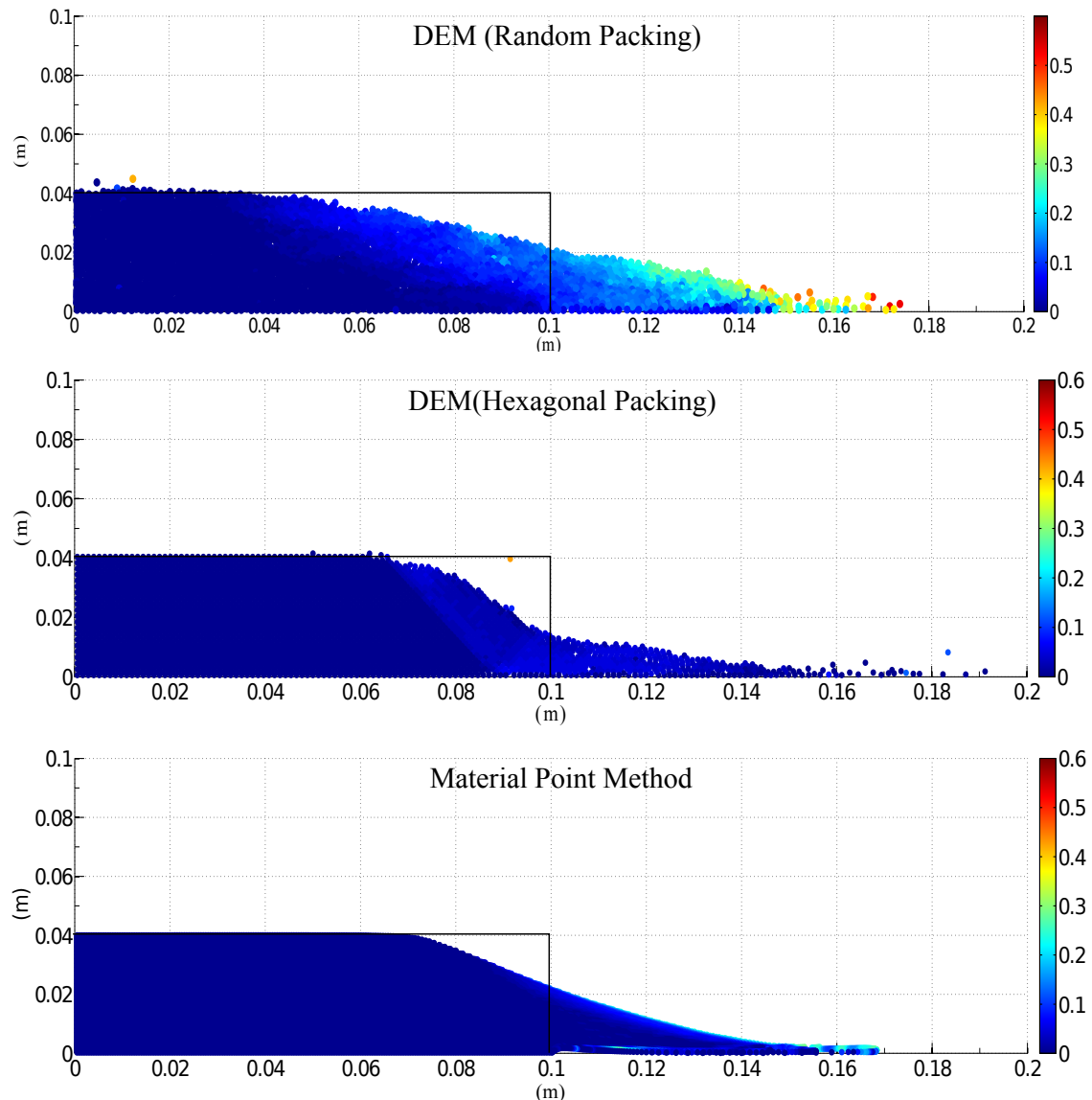


Figure 4.7 Velocity profile of a granular column collapse ( $a' = 0.4 \& t = 3 \times \tau_c$ )

surface, the flow gets deviated along the horizontal direction releasing a huge amount of kinetic energy gained during the free fall. For larger aspect ratio ( $a > 0.7$ ), the resulting static region is a cone, the final height of the cone, i.e.,  $H_f$  lies above the summit of the failure surface. Hence, a different evolution is observed from that of the axis-symmetric geometry (Lube et al., 2005), where the final height coincides with the summit of the failure surface forming a truncated conical deposit. Lajeunesse et al. (2004) articulated the variation in the deposit morphology between the axis-symmetric case and the rectangular collapse to be a geometrical effect rather than as an experimental artefact. The final profile of the collapsed granular column with an initial aspect ratio of 6 is presented in Figure 4.9. An initial failure surface starting from the toe end of the column at an angle of about  $55^\circ$  can be observed at critical time  $\tau_c$ . As the collapse of the granular collapse progresses, successive failure planes parallel to the initial failure surface are formed and shear failure occurs along these planes. The presence of several shear bands in the final profile of the collapsed granular column confirms the hypothesis. Crystallisation in hexagonal packing causes a significant effect on the run-out distance by forming series of parallel shear bands. However, the Material Point Method fails to capture the formation of shear bands during the collapse. This observation throws light on the mechanics of propagation of shear bands in massive landslides such as the Storegga submarine landslide. The flow behaviour becomes similar to that of columns with lower aspect ratio as the flow starts descending along the failure plane. Regardless of the experimental configuration and the initial aspect ratio of the columns, the flow is initiated by a well-defined rupture surface, above which the material slides down leaving a static region underneath the failure plane. Depending on the aspect ratio of the column, two asymptotic behaviours are observed. For smaller aspect ratios, the flow is dominated by friction and by the pressure gradient for larger aspect ratio.

To study the flow dynamics of granular columns with different aspect ratios, the flow front  $L(t)$  and the maximum height of column  $H(t)$  are tracked. The evolution of scaled height ( $H_f/L_i$ ) and the run-out distance  $(L_f - L_i)/L_i$  with time for granular columns with an initial aspect ratio of 0.4 and 6 are presented in Figures 4.10 and 4.11. Time is scaled with respect to the critical time  $\tau_c$ , defined as the time at which the flow is fully mobilized. Three distinct regions can be observed in the flow evolution of granular column collapse regardless of the initial aspect ratio of the column. An initial transient acceleration phase is observed for a time  $0.8\tau_c$ . This phase is followed by a heap movement of granular materials at the foot with a constant spreading velocity  $V$  for about  $2\tau_c$ . When time ' $t$ ' >  $\tau_c$ , the velocity varies linearly with depth in the flowing layer and decreases exponentially with depth near the static layer. This velocity profile is similar to those observed in steady granular surface flows (Lajeunesse et al., 2004). Most of the run-out happens during this phase. The final phase involves deceleration of the flow front and the flow comes to rest after  $0.6\tau_c$ . The spreading of the granular column ceases after a time

in the order of  $3\tau_c$  for all values of aspect ratios, however some motion still persists along the free surface behind the flow front for a much longer time due to internal rearrangement, the duration of which can last up to  $t \approx 6\tau_c$ . For smaller aspect ratios, the critical time is evaluated as the point of intersection of the scaled run-out and height. The critical time predicted for both hexagonal and random packing of grains matches the experimental observations. However, the Material Point Method overestimates the critical time by a factor of 1.25, which means that it takes longer for the flow to be fully mobilized. However, the actual run-out duration is short and the granular materials comes to rest abruptly at about  $t = 3\tau_c$ . For columns with larger aspect ratios, the continuum and particulate approaches simulate similar flow evolution behaviour for times up to  $3\tau_c$ , beyond which particulate simulations stabilise and come to rest, while the flow continues to evolve in MPM simulations resulting in larger run-outs than expected. The flow tends to come to rest at time  $t = 6\tau_c$ . The three phases in a granular flow can be distinctly observed in the flow evolution plot for a granular column with initial aspect ratio of 6 (see Figure figure 4.11). For larger aspect ratios, the flow evolution behaviour observed in the case of random packing matches the experimental observation by Lajeunesse et al. (2004). Hexagonal packing predicts longer time for the flow to evolve, which can be attributed to the increase in the internal resistance due to crystallisation of grains. MPM overestimates the critical time by 50%, however has the same value of run-out as the particulate simulations, at time  $t = 3\tau_c$ , beyond which the material continues to flow until it ceases at  $6\tau_c$ . In order to understand the flow dynamics in the case of Material Point Method it is important to study the effect of different parameters on the deposit morphology.

### 4.2.3 Energy dissipation mechanism

The time evolution of the flow exhibited three distinct stages during the collapse of a granular column. Studying the energy dissipation mechanism provides useful insight into the flow dynamics. shows the time evolution of potential energy ( $E_p$ ) and kinetic energy ( $E_k$ ) normalized by the initial potential energy  $E_o$ .

$$E_p = \sum_{p=1}^{N_p} m_p g h_p \quad (4.8)$$

$$E_{ki} = \frac{1}{2} \sum_{p=1}^{N_p} m_p v_p^2 \quad (4.9)$$

where  $N_p$  is the total number of particles,  $m_p$  is the mass of a particle ‘ $p$ ’,  $h_p$  is the height and  $v_p$  is the velocity of the particle ‘ $p$ ’. It can be observed from the figure that the initial potential energy stored in the particle is converted to kinetic energy which is dissipated as the granular

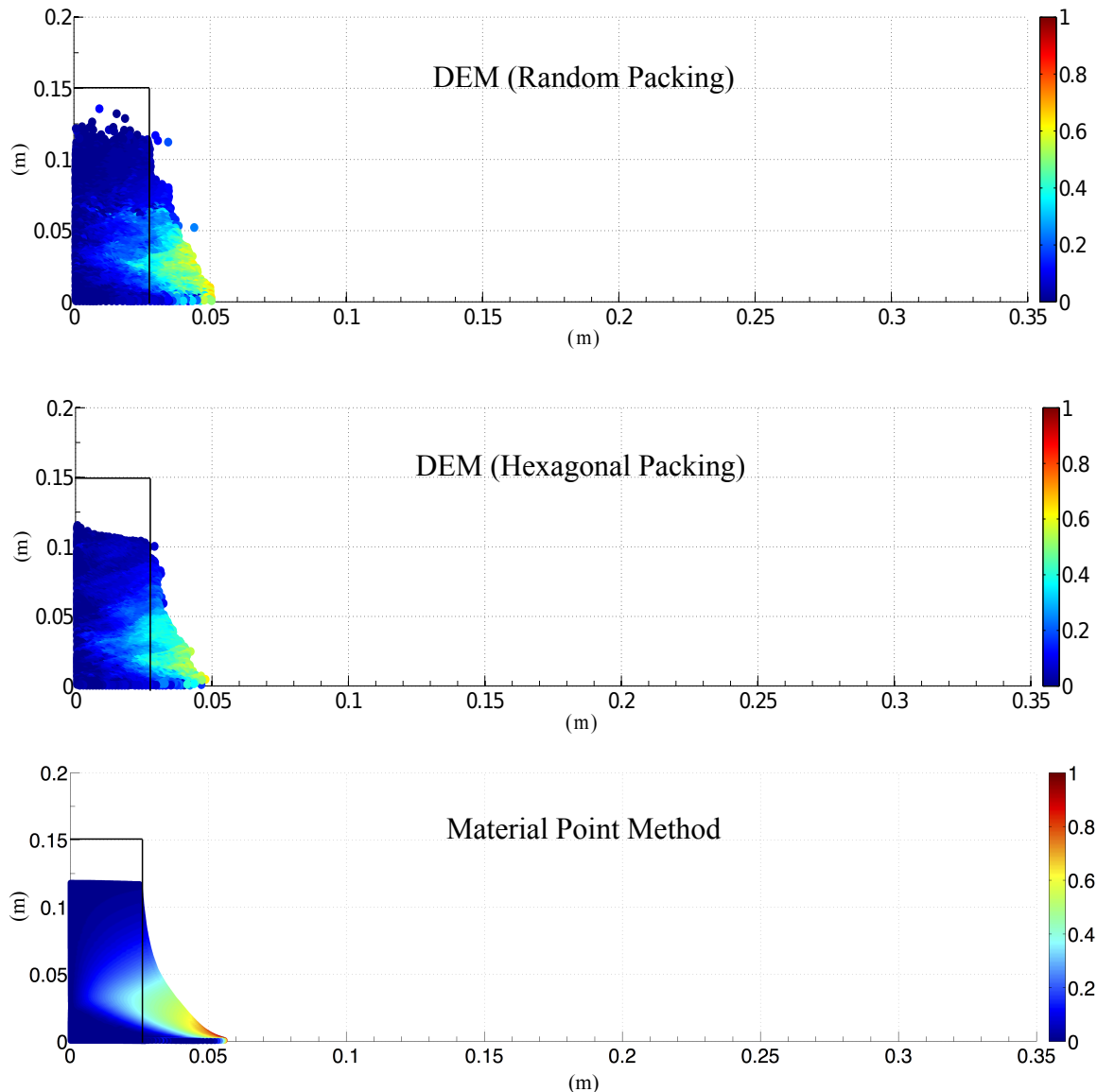


Figure 4.8 Velocity profile of a granular column collapse (' $a' = 6 \& t = \tau_c$ )

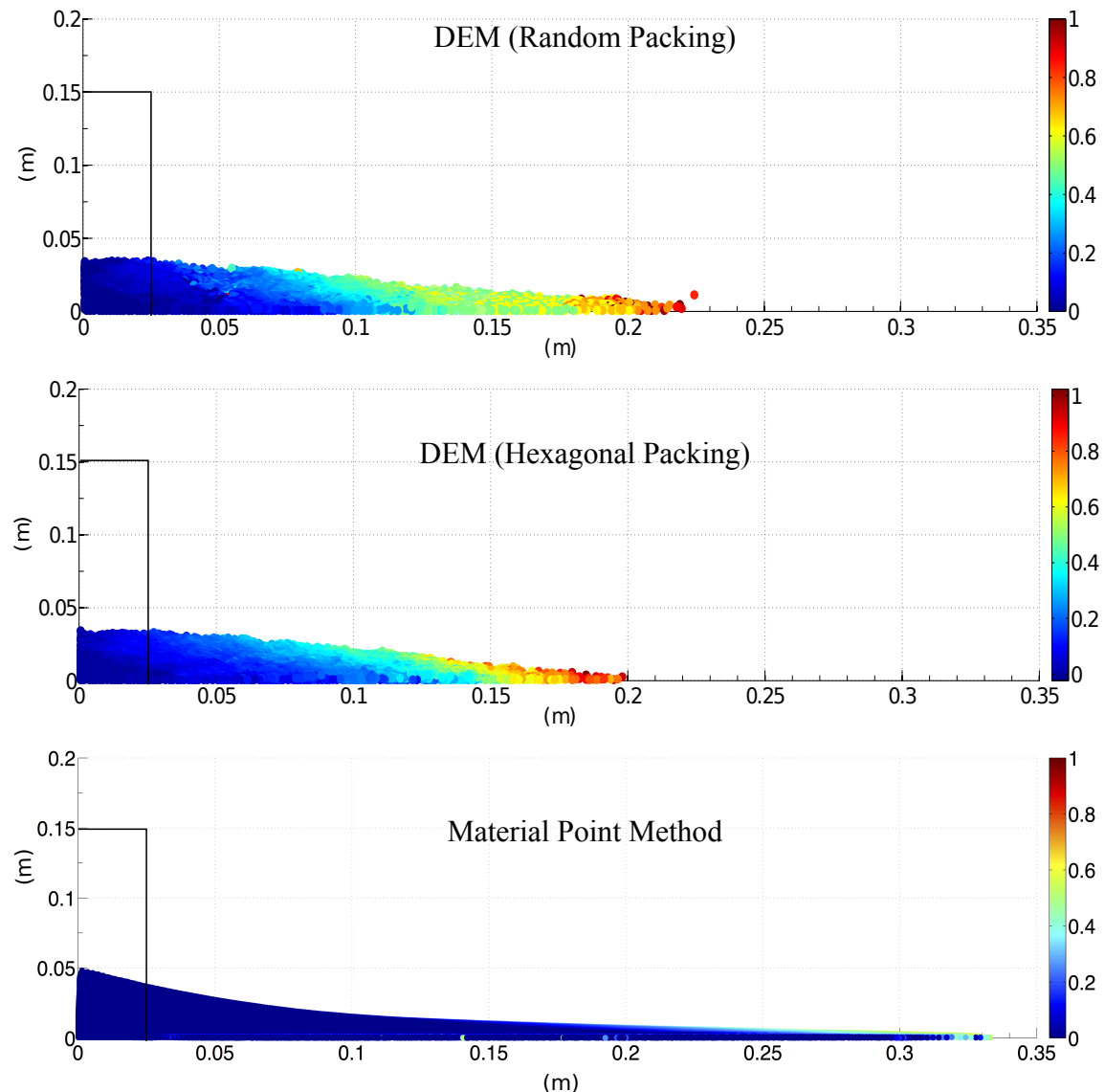
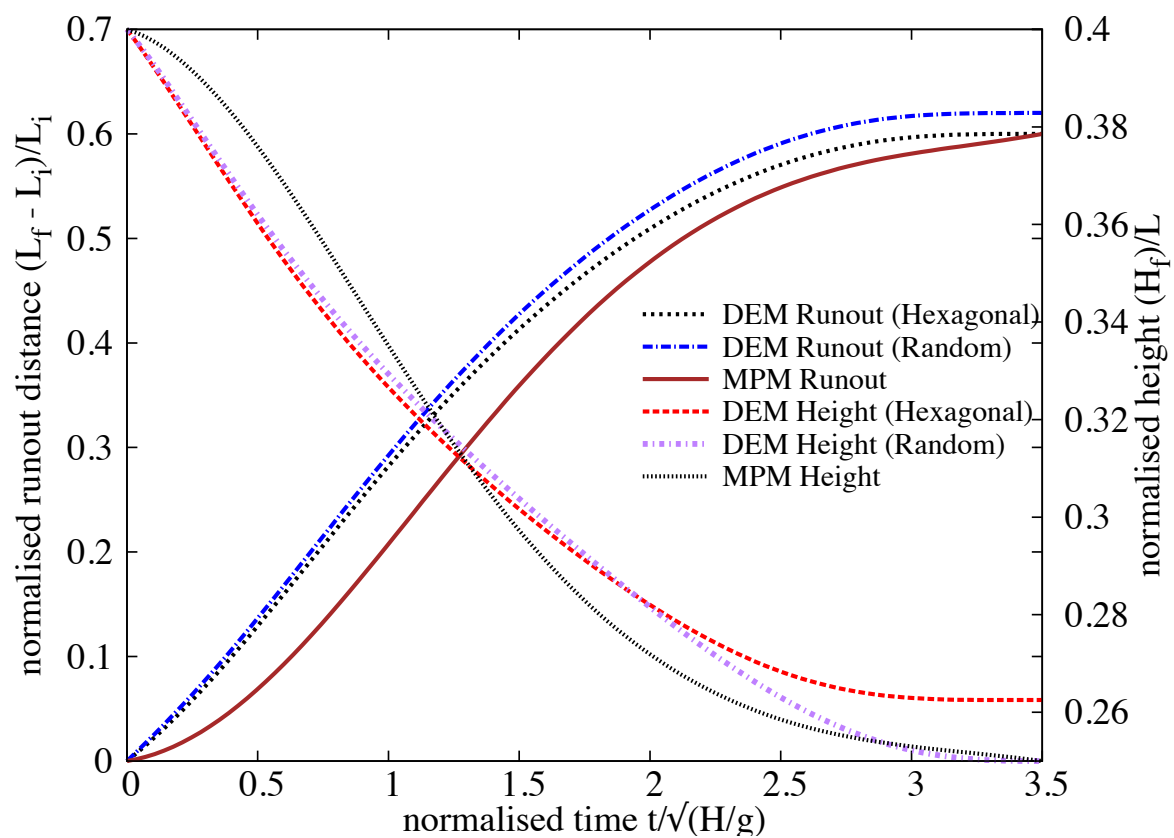
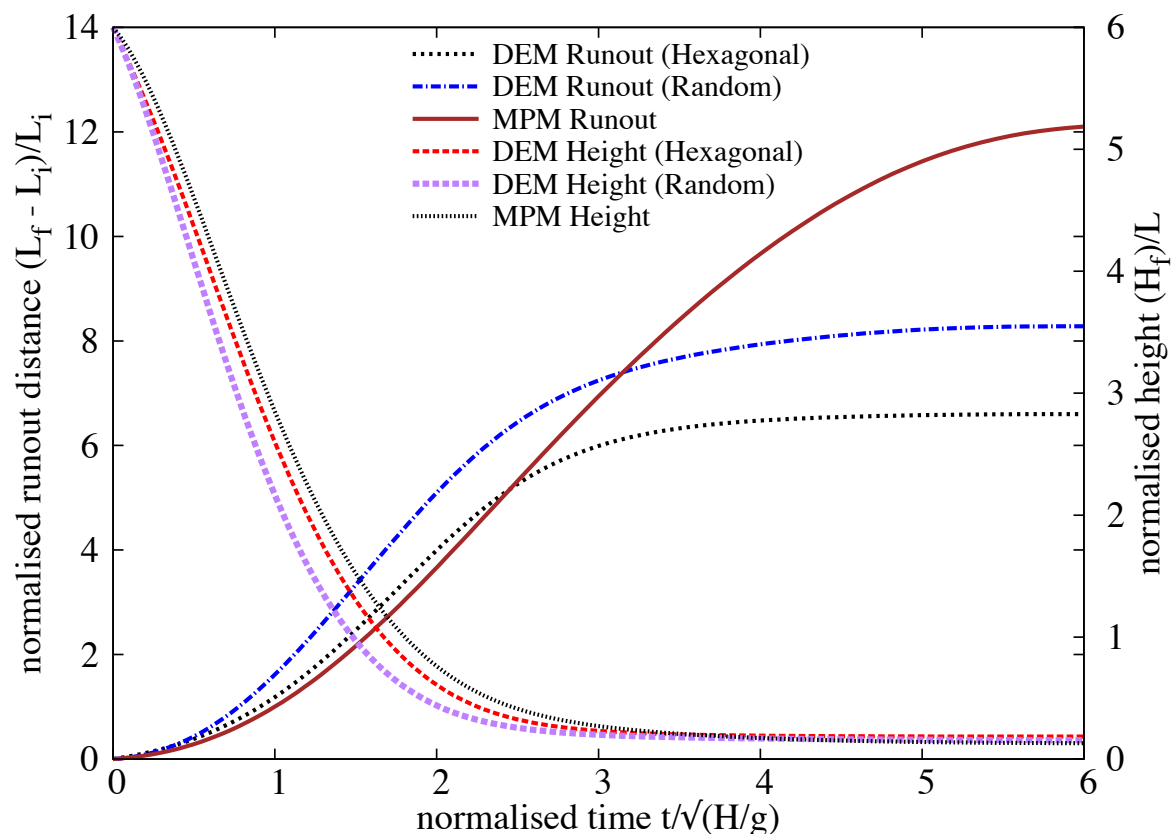


Figure 4.9 Velocity profile of a granular column collapse ( $a' = 6$  &  $t = 3 \times \tau_c$ )

Figure 4.10 Flow evolution of a column with ' $a'$  = 0.4



material flows down. Three successive stages can be identified in the granular column collapse. In the initial acceleration stage ( $t < 0.8\tau_c$ ), the initial potential energy stored in the grains is converted into vertical motion. In the second stage, the grains undergo collisions with the bottom plane and/or with neighbouring grains, and the stored potential energy is converted into horizontal motion. In the third stage, the grains eventually leave the base area of the column and flow sideways. As the process involves collective dynamics of all the particles, it is difficult to predict the exact trajectory of a grain, however, the overall dynamics can be explained. To explain the dissipation of energy during the collapse, Staron et al. (2005) assumed that the total initial potential energy stored in the system is completely dissipated through friction over the entire run-out distance as:

$$\mu m_0 g \times (L_f - L_i) = m_0 g H_o \quad (4.10)$$

where  $\mu$  is the friction coefficient. The model predicts well the flow dynamics for columns with larger aspect ratios, as most of the initial potential energy is dissipated during the collapse involving the entire column. However, for columns with smaller aspect ratios, only a portion of the mass above the failure surface is involved in the flow. Hence, the energy dissipation should involve only the grains lying above the failure surface. A mathematical model, which considers the grains lying above the failure surface, will be derived to predict the flow dynamics of the granular column collapse for different aspect ratios.

## 4.3 Slopes subjected to impact loading

### 4.3.1 Numerical procedures

The numerical samples are composed of  $\sim 13000$  disks with a uniform distribution of diameters by volume fractions in the range  $[d_{min}, d_{max}]$  with  $d_{max} = 1.5d_{min}$ . The mean particle diameter and mass are  $d \simeq 0.0025$  m and  $m \simeq 0.0123$  kg, respectively. The particles are first poured uniformly into a rectangular box of given width and then the right-hand side wall is shifted further to the right to allow the particles to spread. A half-pile is obtained when all particles come to rest; see Fig. ???. This procedure leads to a mean packing fraction  $\simeq 0.83$ .

The initial static pile is set into motion by applying a constant horizontal gradient  $v_{0x}(y) = k(y_{max} - y)$  with  $k > 0$ . Such a configuration mimics the energy transfer mechanism of a horizontal quake along the bottom of the pile. We are interested in the evolution of the geometry of the pile and its total kinetic energy as a function of the initial input energy  $E_0$ . The run-out distance  $R_f$  is the distance of the rightmost particles from the left wall when the pile comes to rest. It will be normalized by the initial extension  $R_0$  of the pile, as in the experiments

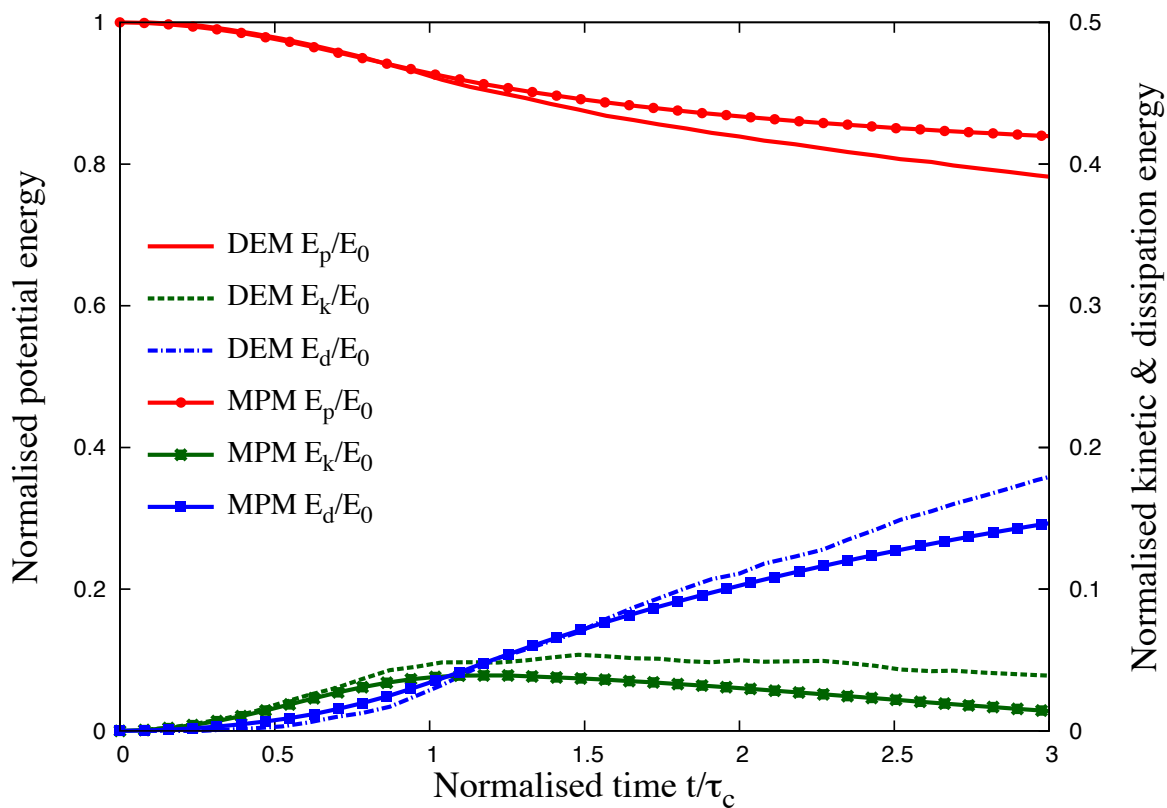
Figure 4.12 Energy evolution of a column with ' $a'$  = 0.4

Figure 4.13 Energy evolution of a column with ' $a'$  = 6

1 of collapsing columns. The total run-out duration  $t_f$  is the time that the pile takes to reach its  
 2 final run-out distance  $R_f$ .

3 The initial static pile is set into motion by applying a horizontal velocity  $v_{0x}(y)$  to all  
 4 particles during a short interval of time. Different velocity fields were tested: 1) The same  
 5 velocity  $v_{0x}(y) = v_0$  applied to all particles, 2) The same velocity  $v_{0x}(y) = v_0$  applied to a  
 6 column of particles next to the left wall, 3) a constant velocity gradient  $v_{0x}(y) = k(y_{max} - y)$   
 7 with  $k > 0$ . The first two pushing modes mimic the case of a pile impacted from the left  
 8 by a moving mass (tsunami, debris...) whereas the last mode represents energy transfer by  
 9 horizontal quake of the bottom line. We will compare briefly below the effect of different  
 10 pushing modes, but later we will mainly explore the third mode. We are interested in the  
 11 evolution of the geometry of the pile and its total kinetic energy as a function of the initial  
 12 energy input  $E_0$ . The run-out distance  $R_f$  is the distance of the rightmost particles from the left  
 13 wall when the pile comes to rest. It will be normalized by the initial extension  $R_0$  of the pile, as  
 14 in the experiments of collapsing columns. The total run-out duration  $t_f$  is the time that the pile  
 15 takes to reach its final run-out distance  $R_f$ .

16 For grain scale simulations, classical Discrete Element Method and Contact Dynamics  
 17 approach is used. A detailed description of the Contact Dynamics method can be found in [Jean](#)  
 18 ([1999](#)); [Moreau](#) ([1993](#)); [Radjai and Dubois](#) ([2011](#)); [Radjai and Richefeu](#) ([2009](#)). This method  
 19 is based on implicit time integration of the equations of motion and a nonsmooth formulation  
 20 of mutual exclusion and dry friction between particles. The CD method requires no elastic  
 21 repulsive potential and no smoothing of the Coulomb friction law for the determination of  
 22 forces. For this reason, the simulations can be performed with large time steps compared to  
 23 molecular dynamics simulations. The unknown variables are particle velocities and contact  
 24 forces, which are calculated at each time step by taking into account the conservation of  
 25 momenta and the constraints due to mutual exclusion between particles and the Coulomb  
 26 friction. We use an iterative research algorithm based on a nonlinear Gauss-Seidel scheme.  
 27 The only contact parameters within the CD method are the friction coefficient  $\mu_s$ , the normal  
 28 restitution coefficient  $e_n$  and the tangential restitution coefficient  $e_t$  between particles. We will  
 29 investigate the effect of these parameters on the evolution of kinetic energy and the profile of  
 30 the pile.

31 The natural units of our system are the mean particle diameter  $d$ , mean particle mass  $m$   
 32 and gravity  $g$ . For this reason, in the following we normalize the lengths by  $d$ , the times by  
 33  $(d/g)^{1/2}$ , the velocities by  $(gd)^{1/2}$  and the energies by  $mgd$ . Video samples of the simulations  
 34 analyzed in this paper can be found by following the link <http://www.cgp-gateway.org/ref018>.

### 4.3.2 Evolution of pile geometry and run-out

In this section, we consider the spreading process following the initial energy input into the pile. Fig. 4.3.2 shows several snapshots of the pile for an initial input energy  $E_0 = 61$  (in dimensionless units). The pile is sheared from the bottom to the top, thus leaving a cavity in the vicinity of the left wall. The cavity is partially filled while the pile continues to spread to the right.

In this section, we consider the spreading process following the initial energy input into the pile. Fig. 4.3.2 shows several snapshots of the pile for each pushing mode and for the same initial energy  $E_0 = 61$  (in dimensionless units). In mode 1, where the same velocity is imparted to all particles, the whole pile moves away from the left wall over a short distance and then it spreads out and declines in slope. The spreading continues farther until the slope nearly declines to zero. In mode 2, where the velocity is applied to a column of particles next to the left wall, the particles belonging to the column are literally expelled from the pile. They fall back farther way on the pile after a ballistic travel above the pile. At the same time, the right side of the pile slightly spreads away while the left side is filled by the particles rolling down into the gap left by the column. In mode 3, the pile is sheared from the bottom to the top, leaving thus a cavity in the vicinity of the left wall. The cavity is partially filled while the pile continues to spread.

All pushing modes involve a transient with a sharp change of the geometry of the pile followed by continuous spreading to the right. In mode 2, most of the energy is carried away by the ejected particles. In mode 1, the pile has a rigid-body velocity component and moves away from the left wall, but shows an efficient energy transfer leading to a long run-out distance. The transient is more energy consuming in mode 3 compared to mode 1. For this reason, the run-out distance in mode 3 is long but shorter than in mode 1. In the following, we analyze in more detail the evolution of the pile in mode 3, which mimics a horizontal quake from the bottom and, despite the creation of a cavity, remains always in contact with the left wall irrespective of the input energy.

Figure 4.4 shows the normalized run-out distance  $(R_f - R_0)/R_0$  and total run-out time  $t_f$  as a function of the input energy  $E_0$ . We observe two regimes both characterized by a power-law run-out distance and time as a function of  $E_0$ . In the first regime, corresponding to the range of low input energies  $E_0 < 40 \text{ mgd}$ , the run-out distance varies as  $R_f \propto (E_0)^\alpha$  with  $\alpha \simeq 0.61 \pm 0.04$  over nearly one decade while the duration keeps a constant value  $t_f \simeq 60 (d/g)^{0.5}$  irrespective of the value of  $E_0$ ! The error on the value of the exponent represents the confidence interval of linear fits on the logarithmic scale. An average run-out speed can be defined from the ratio  $v_s = (R_f - R_0)/t_f$ . According to the data, we have  $v_s \propto (E_0)^{0.61 \pm 0.04}$ . Since the initial average velocity varies as  $v_0 \propto (E_0)^{0.5}$ , this difference between the values of the exponents suggests

that the mobilized mass during run-out declines when the input energy is increased. As we shall see below, the constant run-out time reflects also the collapse of the particles into the cavity left behind the pile.

In the second regime, corresponding to the range of high input energies  $E_0 > 40 \text{ mgd}$ , the run-out distance varies as  $R_f \propto (E_0)^{\alpha'}$  over one decade with  $\alpha' \simeq 0.77 \pm 0.03$  while the duration increases as  $t_f \propto (E_0)^{\beta'}$  with  $\beta' \simeq 0.21 \pm 0.04$ . Hence, in this regime the average run-out speed varies as  $v_s \propto (E_0)^{0.56 \pm 0.07}$ . This exponent is close to the value 0.5 in  $v_0 \propto (E_0)^{0.5}$ , and hence, within the confidence interval of the exponents, in the second regime we may assume  $\beta' \simeq \alpha' - 0.5$  and  $v_s \propto v_0$ .

It is worth noting that a similar power-law dependence of the run-out distance and time were found in the case of collapsing columns of grains with respect to the initial aspect ratio [Topin et al. \(2012\)](#). In the column geometry, the particles spread away owing to the kinetic energy acquired during gravitational collapse of the column. Topin et al. found that the run-out distance varies as a power law of the available peak kinetic energy at the end of the free-fall stage with an exponent  $\simeq 0.5$ . This value is below those obtained here for both regimes. This is, however, physically plausible since the distribution of particle kinetic energies at the end of the collapse is more chaotic than in our simulations where the energy is supplied from the very beginning in a well-defined shear mode. As pointed out by [Staron et al. \(2005\)](#), the distribution of kinetic energies is an essential factor for the run-out distance.

### 4.3.3 Decay of kinetic energy

The nontrivial evolution of the pile geometry in two regimes suggests that the energy supplied to the pile is not simply dissipated by shear and friction with the bottom plane. We also need to split the kinetic energy into its different components ( $x$ ,  $y$  and rotation) of the velocity field. The input energy is in the  $x$  component, but due to both the creation of a cavity next to the left wall and the rolling of the particles down the free surface of the pile and between particles, a fraction of the energy is first transferred to the  $y$  component of the velocity field and dissipated during the transient. In this section, we analyze these features in order to arrive in a picture consistent with the evolution of the pile shape.

The decay of the total kinetic energy  $E$  is displayed in Fig. ??(a) for values of the input energy  $E_0$ . We observe an initial fast drop of  $E$  followed by a regular fall-off until the end of the run-out. This regular fall-off occurs clearly with two different functional forms, thus revealing two stages in the evolution of the pile. Fig. ??(b) shows the same plots normalized by  $E_0$ . We see that all plots corresponding to the first regime (low energies) collapse nearly on to a single time evolution. This is consistent with the fact that, as previously shown, in this regime the run-

## 4.3 Slopes subjected to impact loading

## 25

out time  $t_f$  is independent of the input energy. In contrast, the plots corresponding to the second regime (high energies) collapse only at the beginning of run-out, i.e. for  $t < t_1 \simeq 7.5 (d/g)^{0.5}$ .

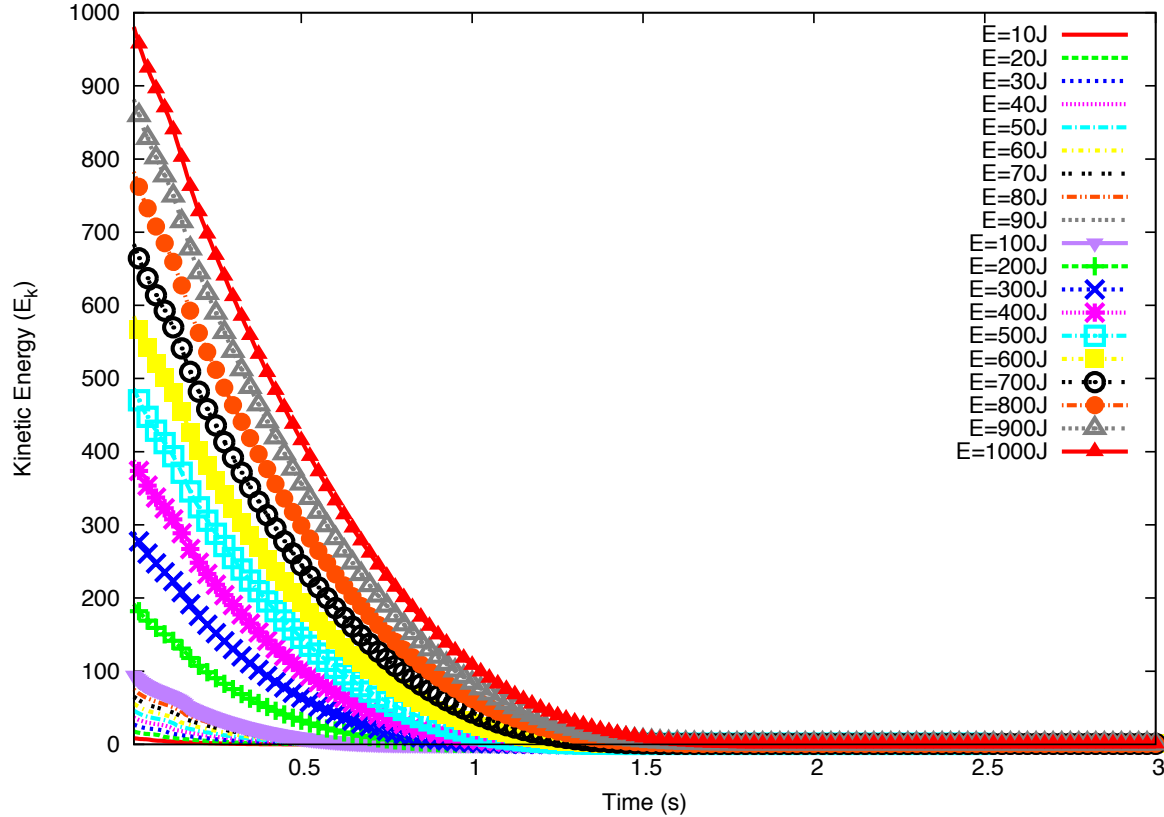


Figure 4.14 Evolution of total kinetic energy with time

?? displays the evolution of kinetic energy in the translational ( $E_x$  and  $E_y$ ) and rotational ( $E_\theta$ ) degrees of freedom of the particles.  $E_x$  decays as the total energy, but  $E_y$  and  $E_\theta$  increase and pass through a peak before decaying rapidly to a negligibly small level. The transient is best observed for  $E_y$ , which has significant values only for  $t < t_1$ . This energy represents the proportion of kinetic energy transferred to the  $y$  component of the velocity field due to the destabilization of the pile and collapse of particles in the cavity behind the pile. We note that the lower  $E_0$ , the higher the peak value of  $E_y/E_0$ . This means that, at low values of the input energy a larger fraction of input energy  $E_0$  is consumed in the destabilization process whereas at a high level of input energy, most of it is dissipated in the spreading phase. For this reason, the total duration  $t_1$  of this destabilization transient is nearly the same in both regimes and its value is controlled by the gravity rather than the input energy. The height of the pile being of the order of  $80 d$ , the total free-fall time for a particle located at this height is  $\simeq 12 (d/g)^{0.5}$ , which is of the same order as  $t_1$ . As to the rotational energy, its contribution both to the transient stage and spreading appears to be negligible.

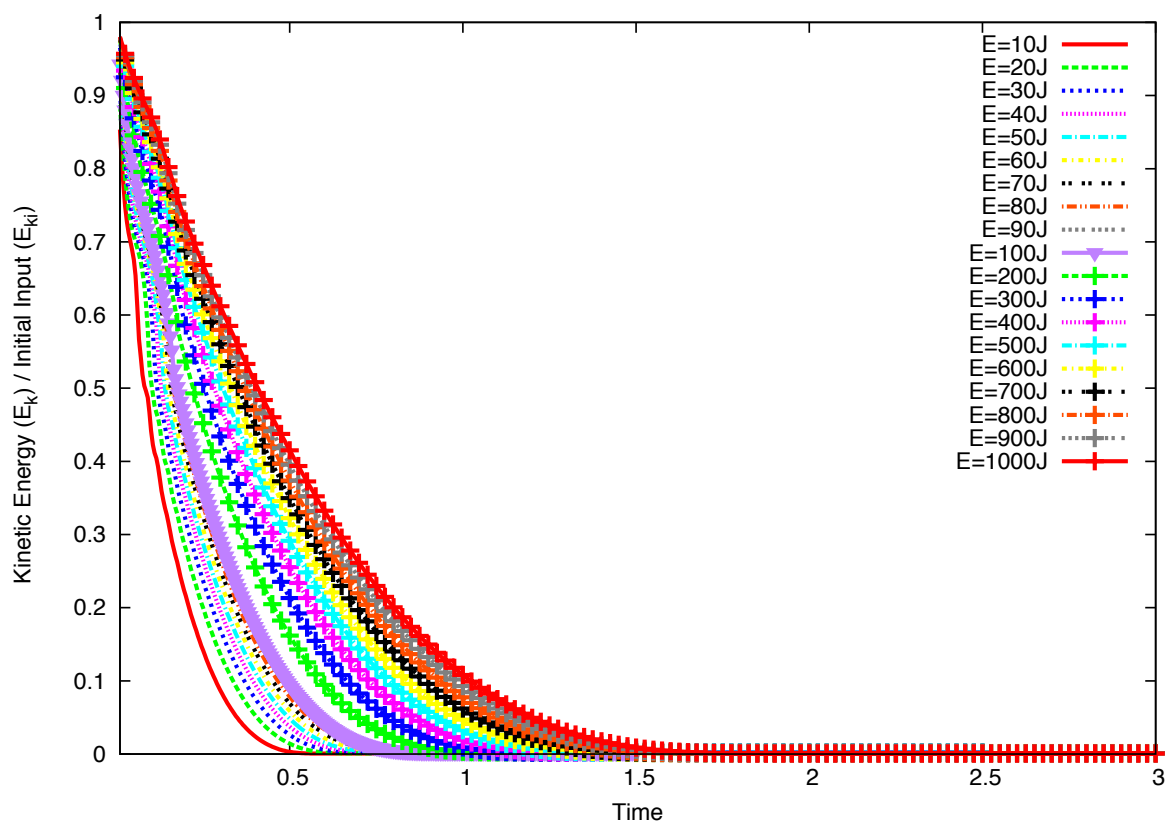


Figure 4.15 Evolution of normalised kinetic energy with time

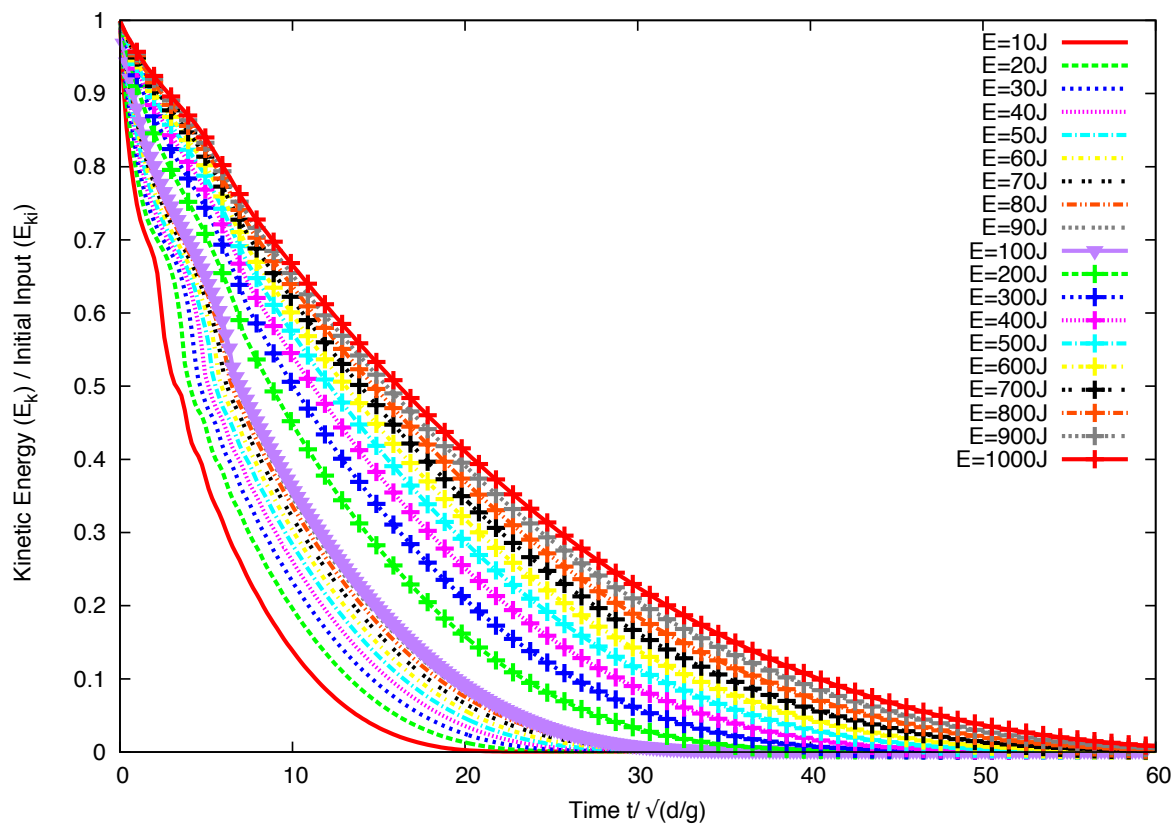


Figure 4.16 Evolution of normalised kinetic energy with normalised time

To analyze the second phase in the second regime, we now consider only the kinetic energy available at the end of the transient. This energy is responsible for most of the run-out and hence it is expected to control the run-out distance and time. Fig. ??(a) shows the evolution of  $E_x'$  normalized by  $E_{x0}'$  as a function of time. The plots have seemingly the same aspect but they show different decay times. A decay time  $\tau$  can be defined as the time required for  $E_x'$  to decline by a factor 1/2. Fig. ??(b) shows the same data in which the time  $t'$  elapsed since  $t_1$  is normalized by  $\tau$ . Interestingly, now all the data nicely collapse on the same curve. We checked that this curve can not be fitted by simple functional forms such as variants of exponential decay. This means that the spreading of the pile is not a self-similar process in agreement with the fact that the energy fades away in a finite time  $t'_f$ .

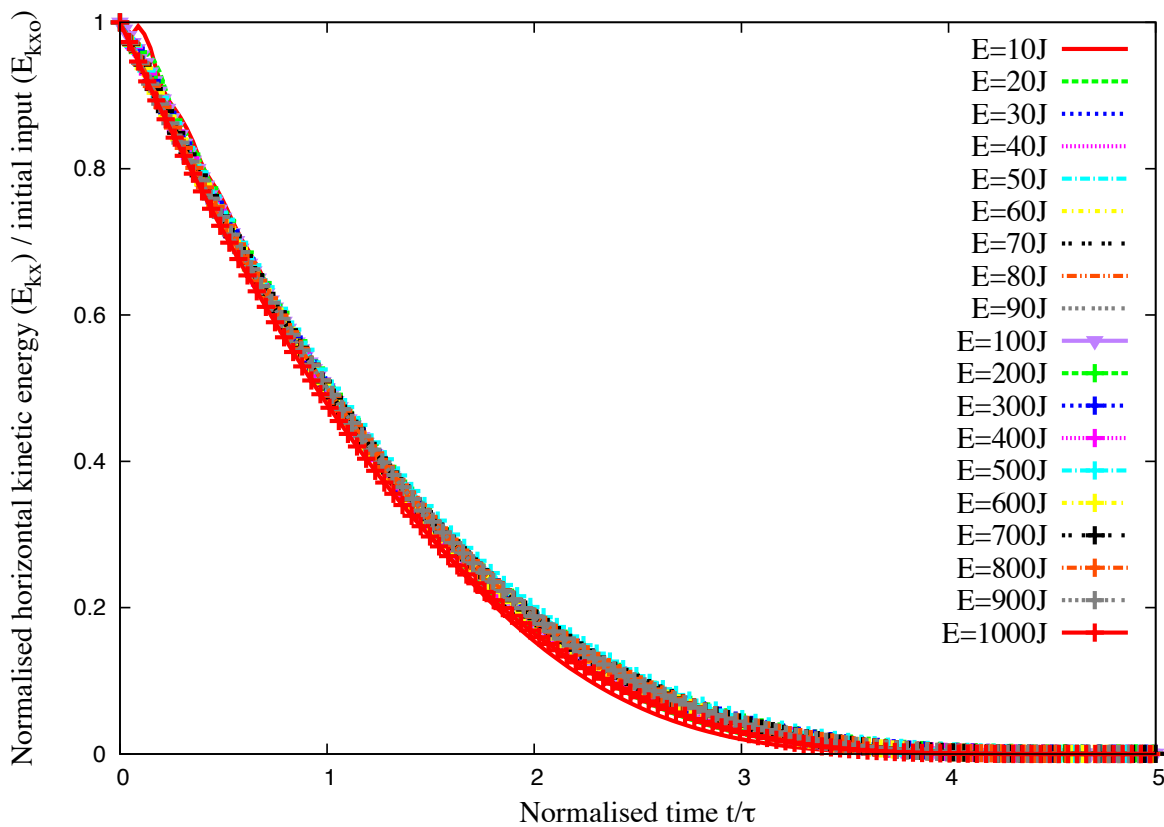


Figure 4.17 Evolution of kinetic energy in the  $x$  component of the velocity field normalized by the available kinetic energy at the end of the transient as a function of normalized time.

The scaling of the data with the decay time  $\tau$  suggests also that the run-out time  $t'_f$  since the beginning of the second phase might be a simple function of  $\tau$ . Figure 4.17 shows both  $t'_f$  and  $\tau$  as a function of  $E_{x0}'$ , where we observe a power law for both times over nearly one decade. The run-out time  $t'_f \propto (E_{x0}')^{\beta'}$  has the same exponent  $\beta' \simeq 0.21 \pm 0.03$  as  $t_f$  as a function of  $E_0$  (see Fig. 4.4). For the decay time we have  $\tau \propto (E_{x0}')^{\beta''}$  with  $\beta'' \simeq 0.28 \pm 0.03$ . The relation

between the two times can thus be expressed as

$$t'_f = k \tau (E'_{x0})^{\beta'' - \beta'}, \quad (4.11)$$

where  $k \simeq 5 \pm 0.4$  and  $\beta'' - \beta' \simeq -0.05 \pm 0.06$ . This value is small enough to be neglected within the confidence interval of our data. It is therefore plausible to assume that the run-out time is a multiple of the decay time and the spreading process is controlled by a single time. We however note that a weak dependence on the energy  $E'_{x0}$  is consistent with the fact that the whole available energy at the beginning of the second phase is not dissipated in the spreading process (calculated from the position of the tip of the pile) since the pile keeps deforming by the movements of the particles at the free surface even when the tip comes to rest. This can explain the small difference between the two exponents as observed here.

#### 4.3.4 Effect of friction

The run-out distance and time and the dissipation of kinetic energy are controlled by the input energy and collective dynamics of the whole pile, as it was analyzed in the previous sections. But they are expected to depend also on the friction. We performed a series of simulations with different values of base friction. The results are shown in Fig. ?? for the profiles of the pile and evolution of the kinetic energy in time. We see no difference in the results for different values of  $e_n = e_t$ . This is a consequence of the fact that, even at large input energies, the pile remains in a dense state so that multiple collisions inside the pile occur at small time scales compared to the deformation time. When the restitution coefficients are increased, more collisions occur during a longer time interval but the overall energy dissipation rate by collisions remains the same. This effect is a seminal example of collective effects which erase the influence of local parameters at the macroscopic scale. In contrast with the restitution coefficients, however, the effect of the friction coefficient is quite important for the run-out, as observed in Fig. ?? for both the energy decay and geometrical profile of the pile. Both the run-out distance and decay time decrease as the friction coefficient is increased. This effect is much more pronounced at low values of the friction coefficient. The run-out time, for example, is reduced by a factor 4 as  $\mu_s$  is increased from 0.1 to 0.4 while the run-out times and profiles do not change much for  $\mu_s = 0.7$ . This “saturation effect” was evidenced in a systematic way in simple shear tests and explained by the observation that the dissipation rate may reach a saturation point where the dilation of the granular material and rolling of the particles change in response to the increase of the friction coefficient Estrada et al. (2008).

The choice of this geometry was motivated by our main goal to focus on the effect of an input energy on the consecutive dynamics of a granular material. For the range of input energies

1 investigated in this pushing test by means of contact dynamics simulations, we observed a  
2 power-law dependence of the run-out distance and time with non-trivial exponents. This is  
3 a central result of this work as it reveals that the power-law behaviour is a generic feature of  
4 granular dynamics. The values of the exponents are not simple functions of the geometry.

5 We also evidenced two regimes with different values of the exponents: a low-energy  
6 regime and a high-energy regime. The first regime reflects mainly the destabilization of the  
7 pile by the quake with a run-out time independent of the input energy whereas the second  
8 regime is governed by the spreading dynamics induced by the higher value of the input energy.  
9 We showed that the evolution of the pile in this high-energy regime can be described by a  
10 characteristic decay time and the energy available at the end of the first stage where the pile is  
11 destabilized by the quake.

12 This work may be pursued along two directions: 1) experimental realization of a similar  
13 setup with different modes of energy injection and 2) investigating the effect of various particle  
14 shapes or the presence of an ambient fluid. Although numerical simulations are generally  
15 reliable with realistic results found in the past studies of steady flows, we believe that the  
16 transients are more sensitive situations than steady states and the experiments are necessary  
17 for checking the validation of the results suggested by the simulations. Provided a convenient  
18 method is used for supplying kinetic energy homogeneously into a pile, our configuration is  
19 also interesting for the investigation of the behavior of a pile immersed in a viscous fluid.

20 **4.3.5 Effect of material points**

21 **4.4 Summary**

22 Multi-scale simulation of granular column collapse was performed to understand the ability and  
23 limitations of continuum models to capture the micro-mechanics of dense granular flows. The  
24 run-out behaviour predicted by both continuum and DEM simulations matches for columns  
25 with small aspect ratios, where the dissipation is predominantly frictional. However, MPM  
26 predicts larger run-out distances for columns with higher aspect ratios. Energy evolution  
27 studies using DEM simulations reveal that the run-out behaviour is independent of frictional  
28 properties of the granular material and collision predominates the initial free-fall regime. The  
29 lack of a collisional energy dissipation mechanism in MPM results in over prediction of run-out  
30 distances.

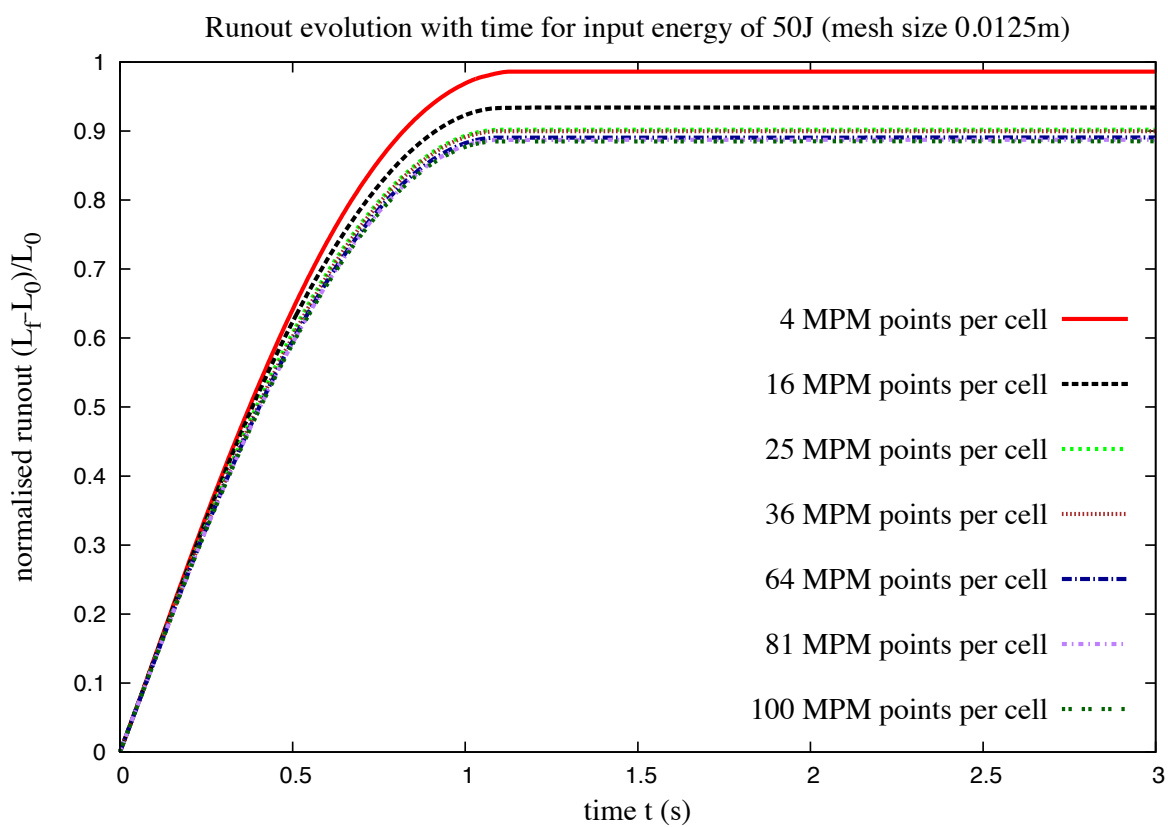


Figure 4.18 Evolution of run-out with time for varying material points per cell ( $E_0 = 12.7mgd$ ).

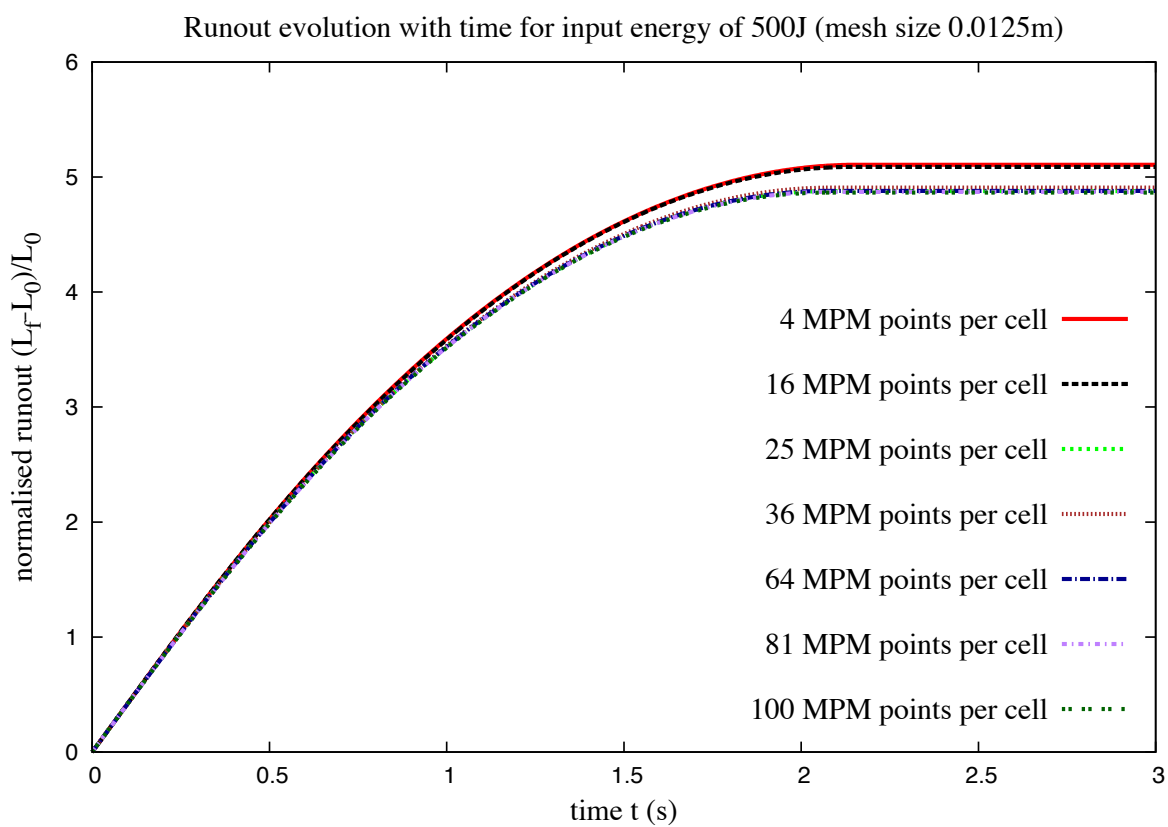


Figure 4.19 Evolution of run-out with time for varying material points per cell ( $E_0 = 152mgd$ ).

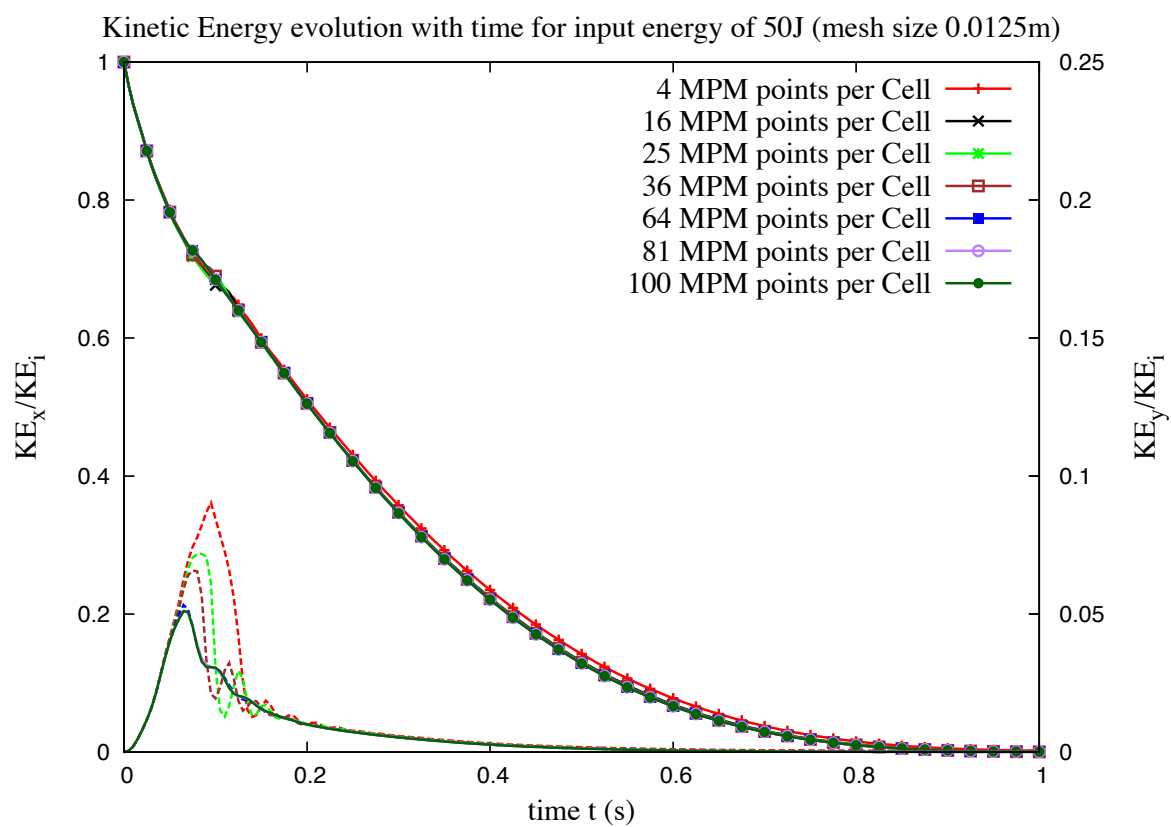


Figure 4.20 Evolution of kinetic energy with time for varying material points per cell ( $E_0 = 12.7mgd$ ).

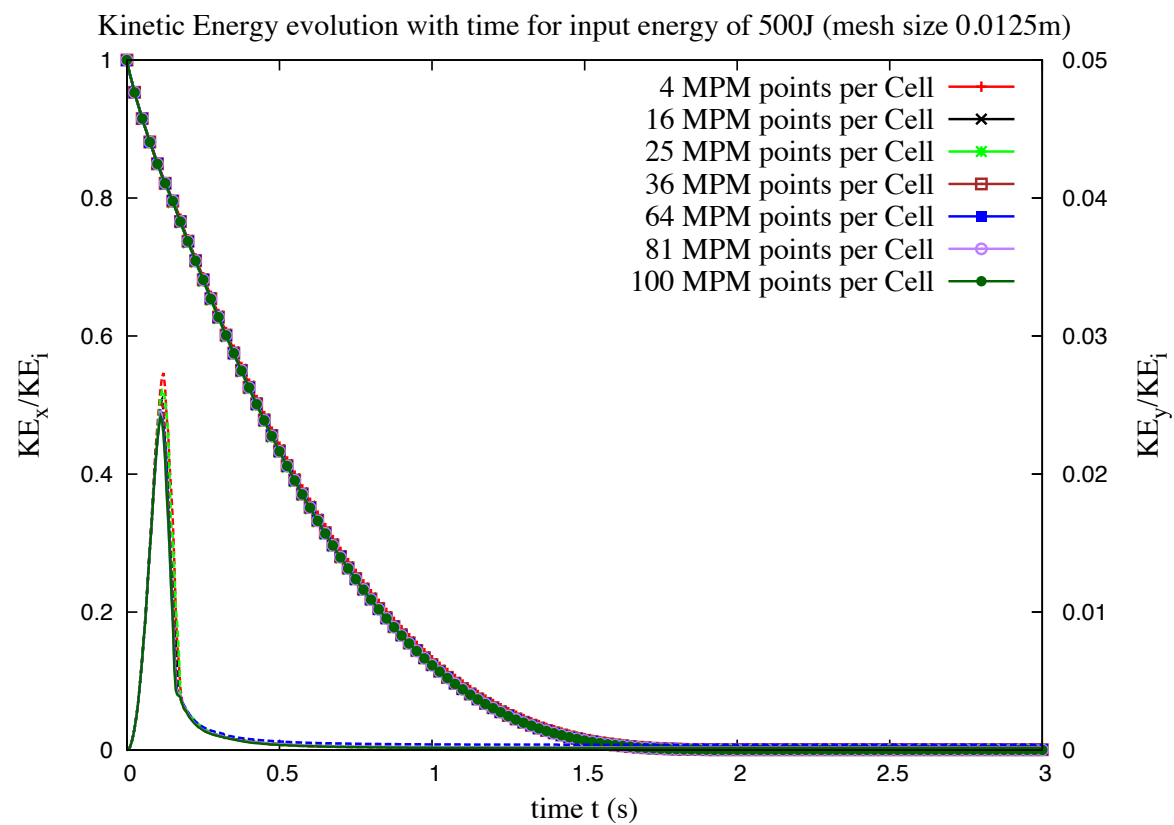


Figure 4.21 Evolution of kinetic with time for varying material points per cell ( $E_0 = 152mgd$ ).

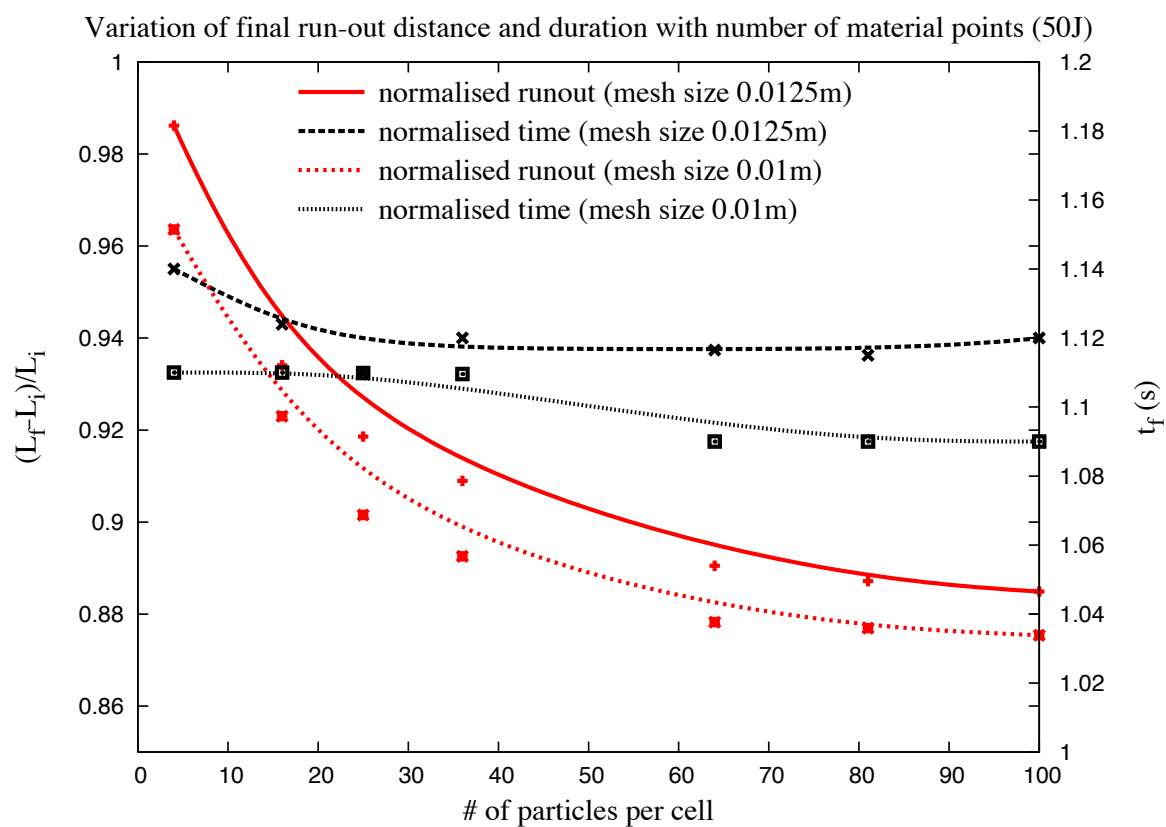


Figure 4.22 Evolution of run-out and duration of flow for varying material points per cell ( $E_0 = 12.7 \text{ mgd}$ ).

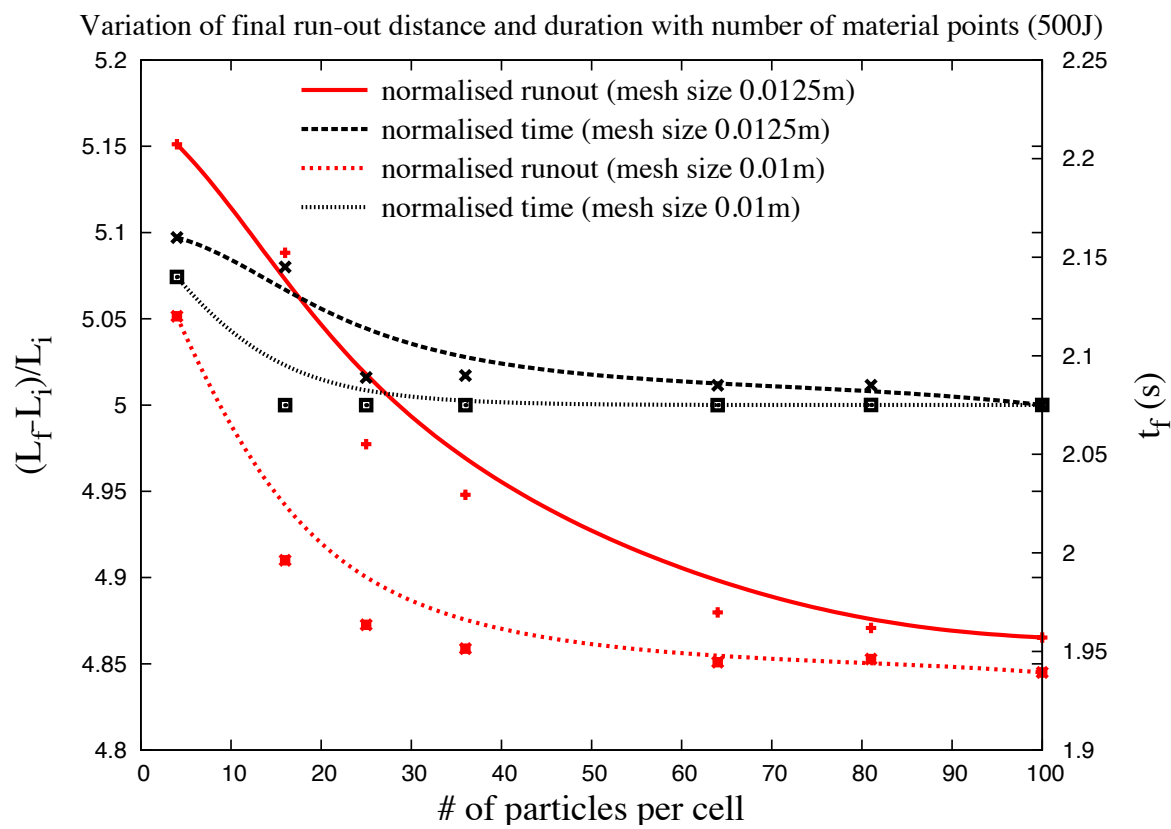


Figure 4.23 Evolution of run-out and duration of flow for varying material points per cell ( $E_0 = 152mgd$ ).

# Chapter 5

## Numerical modelling of fluid–grain interactions

### 5.1 Fluid simulation using lattice Boltzmann method

Grain–fluid systems can be found in many scientific and engineering applications, such as suspensions, fluidised beds, sediment transport, and geo-mechanical problems. In general, the fundamental physical phenomena in these systems are not well understood mainly due to the intricate complexity of grain–fluid interactions and the lack of powerful analysis tools (Han et al., 2007a). In addition to the interaction among soil grains, the motion of soil grains is mainly driven by gravity and the hydrodynamic force exerted by the fluid. The fluid flow pattern can be significantly affected by the presence of soil grains and this often results in a turbulent flow. Hence, the development of an effective numerical framework for modelling both the fluid flow patterns and the grain–fluid interactions is very challenging.

Development of a numerical framework depends crucially on the size of the soil grains relative to the domain/mesh size (Feng et al., 2007). Traditionally, the Navier-Stokes equation is solved by a grid-based Computational Fluid Dynamics (CFD) method, such as the Finite Volume Method, FVM, (Capelatro and Desjardins, 2013) or a mesh-free technique such as Smooth Particle Hydrodynamics (SPH) (Sun et al., 2013). The grid size in FVM or the smooth length in SPH for discretisation of the Navier-Stokes equation is at least an order of magnitude larger than the grain diameter (Xiong et al., 2014).

In situations where the average domain concentration phase is far from dilute, the computational effort is mostly devoted to the grain dynamics. The hydrodynamic forces on the soil grains are applied based on an empirical relation using the domain-averaged local porosity of the soil grains in the grid. As a result, developing a fast fluid hydrodynamics solver

1 is unimportant for dense flows. However, most geo-mechanical problems involve complex  
 2 interactions between the solid and the fluid phase. This requires accurate modelling of the fluid  
 3 flow pattern. Additionally, geophysical problems, such as submarine landslides and debris flow  
 4 have a relatively large simulation domain, which requires parallel computation. Implementing  
 5 traditional grid-based CFD methods face great challenges on multi-processor systems (Xiong  
 6 et al., 2014). Although mesh-free approaches are free from the problem of parallel scalability,  
 7 its modelling accuracy and speed are relatively low when compared to grid-based CFD methods.  
 8 Therefore, an accurate, fast and a highly scalable scheme is required to model fluid - grain  
 9 systems in geo-mechanics.

10 The Navier-Stokes equation describes the motion of a non-turbulent Newtonian fluid. The  
 11 equation is obtained by applying Newton's second law to the fluid motion, together with an  
 12 assumption that the fluid stress is the sum of the viscous term, proportional to the gradient of  
 13 the velocity, and the pressure term. Conventional CFD methods compute pertinent flow fields,  
 14 such as velocity  $u$  and pressure  $p$ , by numerically solving the Navier-Stokes equation in space  $x$   
 15 and time  $t$ . Alternatively, the transport equation or the Boltzmann equation, which deals with a  
 16 single particle distribution function  $f(x, \xi, t)$  in phase space  $(x, \xi)$  and time  $t$ , can be used to  
 17 solve various problems in fluid dynamics.

18 The Lattice Boltzmann Method (LBM) (Chen and Doolen, 1998; Han et al., 2007b; He and  
 19 Luo, 1997a,b; Mei et al., 2000; Zhou et al., 2012) is an alternative approach to the classical  
 20 Navier-Stokes solvers for fluid flows. LBM works on an equidistant grid of cells, called lattice  
 21 cells, which interact only with their direct neighbours. In LBM, the discretisation of continuum  
 22 equations is based on microscopic models and mesoscopic continuum theories. LBM is a  
 23 special discretising scheme of the Boltzmann equation where the particle distribution functions  
 24 (mass fractions) collide and propagate on a regular grid. The important aspect, however, is  
 25 the *discretisation of the velocity*, which means that the particle velocities are restricted to a  
 26 predefined set of orientations.

27 The theoretical premises of the LB equation are that (1) hydrodynamics is insensitive to  
 28 the details of microscopic physics, and (2) hydrodynamics can be preserved so long as the  
 29 conservation laws and associated symmetries are respected in the microscopic and mesoscopic  
 30 level. Therefore, the computational advantages of LBM are achieved by drastically reducing  
 31 the particle velocity space  $\xi$  to only a very few discrete points without seriously degrading  
 32 the hydrodynamics (Mei et al., 2000). This is possible because LBM rigorously preserves the  
 33 hydrodynamic moments of the distribution function, such as mass density and momentum fluxes,  
 34 and the necessary symmetries (He and Luo, 1997a,b). LBM has evolved as a comprehensive  
 35 fluid solver and its theoretical aspects link well with the conventional central finite difference  
 36 scheme (Cook et al., 2004).

### 5.1.1 Formulation

LBM is a ‘micro-particle’ based numerical time-stepping procedure for the solution of incompressible fluid flows. Consider a 2D incompressible fluid flow with density  $\rho$  and kinematic viscosity  $\nu$ , in a rectangular domain  $D$ . The fluid domain is divided into rectangular grids or lattices, with the same grid length ‘ $h$ ’ in both  $x$ - and  $y$ -directions (see figure 5.1).

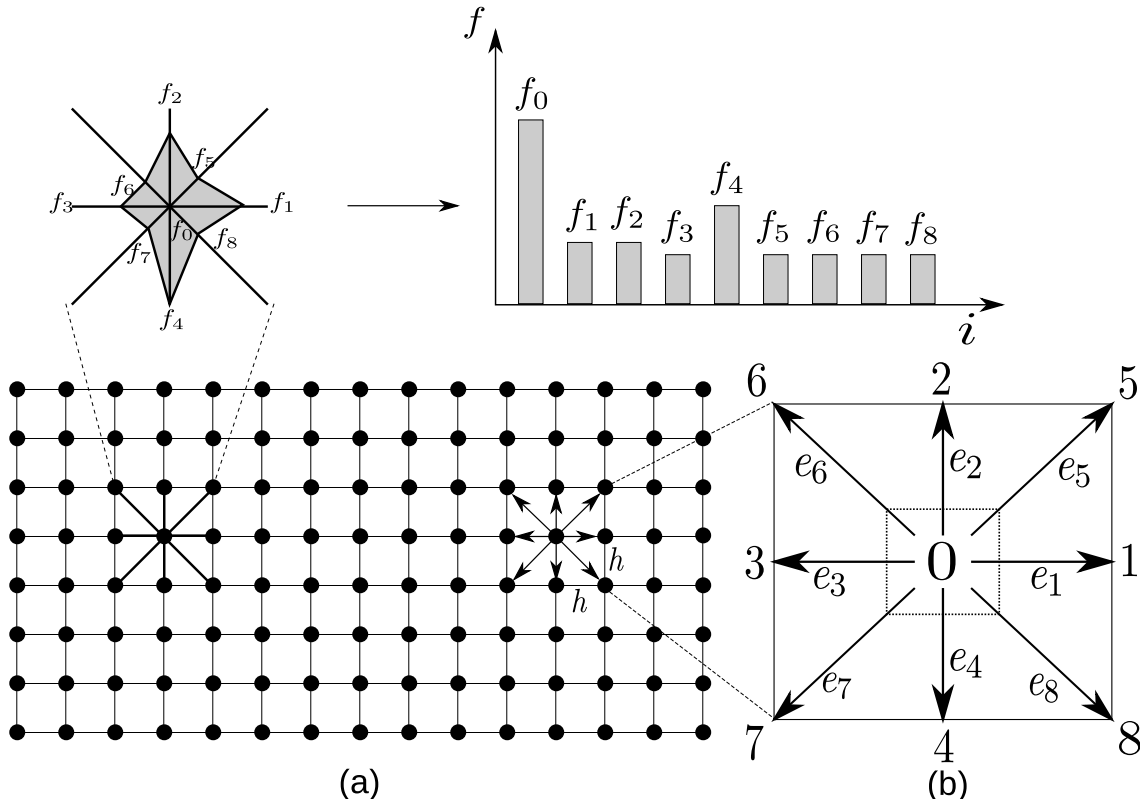


Figure 5.1 The Lattice Boltzmann discretisation and D2Q9 scheme: (a) a standard LB lattice and histogram views of the discrete single particle distribution function/direction-specific densities  $f_i$ ; (b) D2Q9 model.

These lattices are usually classified in the literature using the  $D\alpha Q\beta$ -notation, where  $\alpha$  denotes the space dimensionality and  $\beta$  is the number of discrete velocities (but also including the possibility of having particles at rest) within the momentum discretisation. The most common lattices are the  $D2Q9$  and the  $D3Q19$ -models, see He et al. (1997). The present study focuses on two-dimensional problems, hence the  $D2Q9$  momentum discretisation is adopted.

LBM discretises the Boltzmann equation in space to a finite number of possible particle spatial positions, microscopic momenta, and time. Particle positions are confined to the lattice nodes. The fluid particles at each node are allowed to move to their eight intermediate neighbours with eight different velocities  $e_i (i = 1, \dots, 8)$ . A particle can remain at its own node,

- which is equivalent to moving with zero velocity  $e_o$ . The particle mass is uniform, hence these microscopic velocities and momentum are always effectively equivalent (Han et al., 2007b). Referring to the numbering system shown in figure 5.1, the nine discrete velocity vectors are defined as

$$\begin{cases} e_0 = (0, 0); \\ e_1 = C(1, 0); e_2 = C(0, 1); e_3 = C(-1, 0); e_4 = C(0, -1); \\ e_5 = C(1, 1); e_6 = C(-1, 1); e_7 = C(-1, -1); e_8 = C(1, -1), \end{cases} \quad (5.1)$$

where  $C$  is the lattice speed that is defined as  $C = h/\Delta t$ , and  $\Delta t$  is the discrete time step. The primary variables in LB formulation are called the *fluid density distribution functions*,  $f_i$ , each representing the probable amount of fluid particles moving with the velocity  $e_i$  along the direction  $i$  at each node. The macroscopic variables are defined as functions of the particle distribution function (see figure 5.1)

$$\begin{cases} \rho = \sum_{i=0}^{\beta-1} f_i & \text{(macroscopic fluid density)} \\ \text{and} \\ \overrightarrow{u} = \frac{1}{\rho} \sum_{i=0}^{\beta-1} f_i \overrightarrow{e}_i & \text{(macroscopic velocity)}, \end{cases} \quad (5.2)$$

where  $i \in [0, \beta - 1]$  is an index spanning the discretised momentum space. There are nine fluid density distribution functions,  $f_i (i = 0, \dots, 8)$ , associated with each node in the *D2Q9* model. The evolution of the density distribution function at each time step for every lattice point is governed by

$$f_i(\mathbf{x} + \mathbf{e}_i \Delta t, t + \Delta t) = f_i(\mathbf{x}, t) - \frac{1}{\tau} [f_i(\mathbf{x}, t) - f_i^{eq}(\mathbf{x}, t)] \quad (i = 0, \dots, 8), \quad (5.3)$$

where for any grid node  $\mathbf{x}$ ,  $\mathbf{x} + \mathbf{e}_i \Delta t$  is its nearest node along the direction  $i$ .  $\tau$  is a non-dimensional relaxation time parameter, which is related to the fluid viscosity; and  $f_i^{eq}$  is termed as the equilibrium distribution function that is defined as

$$\begin{cases} f_0^{eq} = w_0 \rho (1 - \frac{3}{2C^2} \mathbf{v} \cdot \mathbf{v}) \\ \text{and} \\ f_i^{eq} = w_i \rho (1 + \frac{3}{C^2} \mathbf{e}_i \cdot \mathbf{v} \frac{9}{2C^2} (\mathbf{e}_i \cdot \mathbf{v})^2 - \frac{3}{2C^2} \mathbf{v} \cdot \mathbf{v}) \quad (i = 0, \dots, 8), \end{cases} \quad (5.4)$$

## 5.1 Fluid simulation using lattice Boltzmann method

## 41

in which,  $w_i$  represents the fixed weighting values:

$$w_0 = \frac{4}{9}, \quad w_{1,2,3,4} = \frac{1}{9}, \quad \text{and} \quad w_{5,6,7,8} = \frac{1}{36}. \quad (5.5)$$

The right-hand side of [eq. 5.3](#) is often denoted as  $f_i(\mathbf{x}, t_+)$  and termed the post collision distribution. LBM ensures conservation of total mass and total momentum of the fluid particles at each lattice node (see [eq. 5.3](#)). The lattice Boltzmann modelling consists of two phases: *collision* and *streaming*. The collision phase computed in the right-hand side of [eq. 5.3](#) involves only those variables that are associated with each node  $\mathbf{x}$ , and therefore is a local operation. The streaming phase then explicitly propagates the updated distribution functions at each node to its neighbours  $\mathbf{x} + e_i \Delta t$ , where no computations are required and only data exchange between neighbouring nodes are necessary. These features, together with the explicit time-stepping nature and the use of a regular grid, make LB computationally efficient, simple to implement and easy to parallelise ([Han et al., 2007b](#)).

The streaming step involves the translation of the distribution functions to their neighbouring sites according to the respective discrete velocity directions, as illustrated in figure [5.2](#) in the *D2Q9* model. The collision step, (see figure [5.3](#)) consists of re-distribution the local discretised Maxwellian equilibrium functions in such a way that local mass and momentum are invariants. In incompressible flows, the energy conservation is equivalent to the momentum conservation ([He et al., 1997](#)).

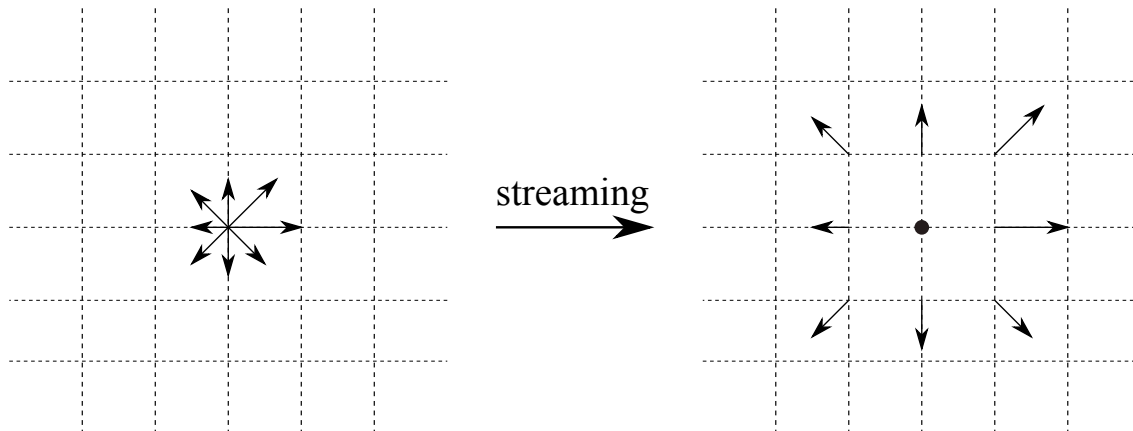


Figure 5.2 Illustration of the streaming process on a *D2Q9* lattice. The magnitude of the distribution functions remains unchanged, but they move to a neighbouring node according to their direction.

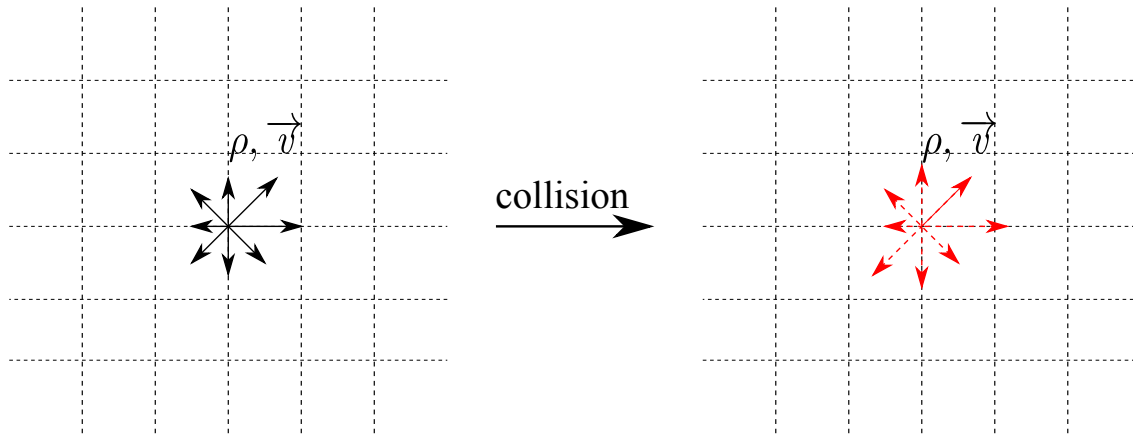


Figure 5.3 Illustration of the collision process on a  $D2Q9$  lattice. The local density  $\rho$  and velocity  $v$  are conserved, but the distribution functions change according to the relaxation to local Maxwellian rule.

<sup>1</sup> The standard macroscopic fluid variables, such as density  $\rho$  and velocity  $v$ , can be recovered  
<sup>2</sup> from the distribution functions as

$$\rho = \sum_{i=0}^8 f_i, \quad \text{and} \quad \rho \mathbf{v} = \sum_{i=0}^8 f_i e_i. \quad (5.6)$$

<sup>4</sup> The fluid pressure field ‘ $p$ ’ is determined by the equation of state

$$p = C_s^2 \rho, \quad (5.7)$$

<sup>6</sup> where  $C_s$  is termed the fluid speed of sound and is related to the lattice speed  $C$  as

$$C_s = C/\sqrt{3}. \quad (5.8)$$

<sup>8</sup> The kinematic viscosity of the fluid  $\nu$  is implicitly determined by the model parameters  $h$ ,  
<sup>9</sup>  $\Delta t$  and  $\tau$  as

$$\nu = \frac{1}{3}(\tau - \frac{1}{2}) \frac{h^2}{\Delta t} = \frac{1}{3}(\tau - \frac{1}{2}) Ch, \quad (5.9)$$

<sup>11</sup> which indicates that these three parameters are related to each other and have to be appropriately  
<sup>12</sup> selected to represent the correct fluid viscosity. An additional constraint to the parameter  
<sup>13</sup> selection is the lattice speed  $C$ , which must be sufficiently large in comparison to the maximum  
<sup>14</sup> fluid velocity  $v_{max}$ , to ensure accuracy of the solution. The ‘computational’ Mach number,  $M_a$ ,  
<sup>15</sup> defined as

$$M_a = \frac{v_{max}}{C}. \quad (5.10)$$

Theoretically, for an accurate solution, the Mach number is required to be  $<< 1$ . In practice,  $M_a$  should be at least smaller than 0.1 (He et al., 1997). From a computational point of view, it is more convenient to choose  $h$  and  $\tau$  as two independent parameters and  $\Delta t$  as the derived parameter

$$\Delta t = (\tau - \frac{1}{2}) \frac{h^2}{3v}. \quad (5.11)$$

It can be observed that  $\tau$  has to be greater than 0.5 (He et al., 1997). Since there is no a priori estimation available to determine appropriate values of  $h$  and  $\tau$ , for a given fluid flow problem and a known fluid viscosity  $v$ , a *trial and error* approach is employed to ensure a smaller *Mach Number*. This is similar to choosing an appropriate Finite Element mesh size, without using automatic adaptive mesh techniques.

### 5.1.2 Lattice Boltzmann - Multi-Relaxation Time (LBM-MRT)

The Lattice Boltzmann Bhatnagar-Gross-Krook (LGBK) method is capable of simulating various hydrodynamics, such as multiphase flows and suspensions in fluid (Succi, 2001; Succi et al., 1989). However, LBM suffers from numerical instability when the dimensionless relaxation time  $\tau$  is close to 0.5. The Lattice Boltzmann Method – Multi-Relaxation Time (LBM-MRT) overcomes the deficiencies of linearised single relaxation LBM-BGK approach, such as the fixed Prandtl number ( $Pr=v/\kappa$ ), where the thermal conductivity ‘ $\kappa$ ’ is unity (Liu et al., 2003). LBM-MRT offers better numerical stability and has more degrees of freedom. In LBM-MRT the advection is mapped onto the momentum space by a linear transformation and the flux is finished within the velocity space (Du et al., 2006).

The lattice Boltzmann equation with multiple relaxation time approximation is written as

$$f_\alpha(\mathbf{x} + \mathbf{e}_i \Delta_t, t + \Delta_t) - f_\alpha(\mathbf{x}, t) = -\mathbf{S}_{\alpha i}(f_i(\mathbf{x}, t) - f_i^{eq}(\mathbf{x}, t)), \quad (5.12)$$

where  $\mathbf{S}$  is the collision matrix. The nine eigen values of  $\mathbf{S}$  are all between 0 and 2 so as to maintain linear stability and separation of scales. This ensures that the relaxation times of non-conserved quantities are much faster than the hydrodynamic time scales. The LGBK model is a special case in which the nine relaxation times are all equal and the collision matrix  $\mathbf{S} = \frac{1}{\tau} \mathbf{I}$ , where  $\mathbf{I}$  is the identity matrix. The evolutionary progress involves two steps, advection and flux:

$$f_\alpha^+(\mathbf{x}, t) - f_\alpha(\mathbf{x}, t) = -\mathbf{S}_{\alpha i}(f_i(\mathbf{x}, t) - f_i^{eq}(\mathbf{x}, t)) \quad (5.13)$$

$$f_\alpha(\mathbf{x} + e_\alpha \Delta_t, t + \Delta_t) = f_\alpha^+(\mathbf{x}, t). \quad (5.14)$$

<sup>1</sup> The advection (eq. 5.13) can be mapped to the momentum space by multiplying with a  
<sup>2</sup> transformation matrix  $\mathbf{M}$ . The evolutionary equation of LBM–MRT is written as

$$\mathbf{f}(\mathbf{x} + \mathbf{e}_i \Delta_t, t + \Delta_t) - \mathbf{f}(\mathbf{x}, t) = -\mathbf{M}^{-1} \hat{\mathbf{S}}(\hat{\mathbf{f}}(\mathbf{x}, t) - \hat{\mathbf{f}}^{eq}(\mathbf{x}, t)), \quad (5.15)$$

<sup>4</sup> where  $\mathbf{M}$  is the transformation matrix mapping a vector  $\mathbf{f}$  in the discrete velocity space  $\mathbb{V} = \mathbb{R}^b$   
<sup>5</sup> to a vector  $\hat{\mathbf{f}}$  in the moment space  $\mathbb{V} = \mathbb{R}^b$ .

$$\hat{\mathbf{f}} = \mathbf{M}\mathbf{f}, \quad (5.16)$$

$$\mathbf{f}(\mathbf{x}, t) = [f_0(\mathbf{x}, t), f_1(\mathbf{x}, t), \dots, f_8(\mathbf{x}, t)]^T. \quad (5.17)$$

<sup>9</sup> The collision matrix  $\hat{\mathbf{S}} = \mathbf{M}\mathbf{S}\mathbf{M}^{-1}$  in moment space is a diagonal matrix:

$$\hat{\mathbf{S}} = \text{diag}[s_1, s_2, s_3, \dots, s_9].$$

<sup>11</sup> The transformation matrix  $\mathbf{M}$  can be constructed via Gram-Schmidt orthogonalisation procedure.  
<sup>12</sup> The general form of the transformation matrix  $\mathbf{M}$  can be written as

$$\mathbf{M} = [|p\rangle, |e\rangle, |e^2\rangle, |u_x\rangle, |q_x\rangle, |u_y\rangle, |q_y\rangle, |p_{xx}\rangle, |p_{xy}\rangle]^T, \quad (5.18)$$

<sup>14</sup> whose elements are,

$$|p\rangle = |e_\alpha|^0 \quad (5.19a)$$

$$|e\rangle_\alpha = Qe_\alpha^2 - b_2 \quad (5.19b)$$

$$|e^2\rangle_\alpha = a_1(Qe_\alpha^4 - b_6) + a_2(Qe_\alpha^4 - b_6) \quad (5.19c)$$

$$|u_x\rangle_\alpha = e_{\alpha,x} \quad (5.19d)$$

$$|q_x\rangle_\alpha = (b_1 e_\alpha^2 - b_3) e_{\alpha,x} \quad (5.19e)$$

$$|u_y\rangle_\alpha = e_{\alpha,y} \quad (5.19f)$$

$$|q_y\rangle_\alpha = (b_1 e_\alpha^2 - b_3) e_{\alpha,y} \quad (5.19g)$$

$$|p_{xx}\rangle_\alpha = de_{\alpha,x}^2 - e_\alpha^2 \quad (5.19h)$$

$$|p_{xy}\rangle_\alpha = e_{\alpha,x} e_{\alpha,y}, \quad (5.19i)$$

<sup>25</sup> where  $d = 2$  and  $Q = 9$ ,  $b_1 = \sum_{\alpha=1}^Q e_{\alpha,x}^2$ ,  $b_2 = \sum_{\alpha=1}^Q e_\alpha^2$ ,  $b_3 = \sum_{\alpha=1}^Q e_\alpha^2 e_{\alpha,x}^4$ ,  $a_1 = ||e^2||^2$ , and  
<sup>26</sup>  $a_2 = \sum_{\alpha=0}^{Q-1} (Qc_\alpha^2 - b_2) \times (Qc_\alpha^4 - b_6)$ .

## 5.1 Fluid simulation using lattice Boltzmann method

45

Explicitly, the transformation matrix can be written as

$$\mathbf{M} = \begin{bmatrix} 1 & 1 & 1 & 1 & 1 & 1 & 1 & 1 & 1 \\ -4 & -1 & -1 & -1 & -1 & 2 & 2 & 2 & 2 \\ 4 & -2 & -2 & -2 & -2 & 1 & 1 & 1 & 1 \\ 0 & 1 & 0 & -1 & 0 & 1 & -1 & -1 & 1 \\ 0 & -2 & 0 & 2 & 0 & 1 & -1 & -1 & 1 \\ 0 & 0 & 1 & 0 & -1 & 1 & 1 & -1 & -1 \\ 0 & 0 & -2 & 0 & 2 & 1 & 1 & -1 & -1 \\ 0 & 1 & -1 & 1 & -1 & 0 & 0 & 0 & 0 \\ 0 & 0 & 0 & 0 & 0 & 1 & 1 & 1 & 1 \end{bmatrix}. \quad (5.20)$$

The corresponding equilibrium distribution functions in moment space  $\widehat{\mathbf{f}}^{eq}$  is given as

$$\widehat{\mathbf{f}}^{eq} = [\rho_0, e^{eq}, e^{2eq}, u_x, q_x^{eq}, q_y^{eq}, p_{xx}^{eq}, p_{xy}^{eq}]^T, \quad (5.21)$$

where

$$e^{eq} = \frac{1}{4}\alpha_2 p + \frac{1}{6}\gamma_2(u_x^2 + y_y^2) \quad (5.22a)$$

$$e^{2eq} = \frac{1}{4}\alpha_3 p + \frac{1}{6}\gamma_4(u_x^2 + y_y^2) \quad (5.22b)$$

$$q_x^{eq} = \frac{1}{2}c_1 u_x \quad (5.22c)$$

$$q_y^{eq} = \frac{1}{2}c_2 u_y \quad (5.22d)$$

$$p_{xx}^{eq} = \frac{3}{2}\gamma_1(u_x^2 - u_y^2) \quad (5.22e)$$

$$p_{xy}^{eq} = \frac{3}{2}\gamma_3(u_x u_y). \quad (5.22f)$$

To get the correct hydrodynamic equation, the values of the co-efficients are chosen as  $\alpha_2 = 24$ ,  $\alpha_3 = -36$ ,  $c_1 = c_2 = -2$ ,  $\gamma_1 = \gamma_3 = 2/3$ ,  $\gamma_2 = 18$  and  $\gamma_4 = -18$ . The values of the elements in the collision matrix are:  $s_8 = s_9 = \tau$  and  $s_1 = s_4 = s_6 = 1.0$  and the others vary between 1.0 and 2.0 for linear stability. Through the Chapman-Enskog expansion (Du et al., 2006), the incompressible Navier-Stokes equation can be recovered and the viscosity is given as

$$\nu = c_s^2 \Delta t (\tau - 0.5). \quad (5.23)$$

### **5.1.3 Boundary conditions**

Boundary conditions (BC) form an important part of any numerical technique. In many cases, the boundary conditions can strongly influence the accuracy of the algorithm. Velocity and pressure are not the primary variables in LBM, hence the standard pressure, velocity, and mixed boundary conditions cannot be imposed directly. Alternative conditions in terms of the distribution functions are adopted to describe the boundary conditions.

#### **7 Periodic boundary condition**

The simplest type of boundary condition is the periodic boundary. In this case, the domain is folded along the direction of the periodic boundary pair. For boundary nodes, the neighbouring nodes are on the opposite boundary, using the normal referencing of neighbours (see figure 5.1a). From the perspective of submarine landslide modelling, the periodic boundary conditions are useful for preliminary analysis, as they imply a higher degree of symmetry of the fluid domain. Further information on the periodic boundary condition can be found in Aidun et al. (1998).

#### **14 No-slip boundary condition**

The most commonly adopted BC in the lattice Boltzmann approach is the no-slip BC, especially the simple bounce-back rule, which is quite elegant and surprisingly accurate. The basic idea is that the incoming distribution functions at a wall node are reflected back to the original fluid nodes, but with the direction rotated by  $\pi$  radians. The bounce-back boundary condition is one of the benefits of LBM, as it is trivial to implement and it allows one to effortlessly introduce obstacles into the fluid domain. However, the boundary conditions have been proven to be only first-order accurate in time and space (Pan et al., 2006). A straightforward improvement is to consider the wall-fluid interface to be situated halfway between the wall and the fluid lattice nodes (Ziegler, 1993). It involves defining the *solid* nodes as those lying within the stationary wall regions, and the *fluid* nodes otherwise. Then, if  $i$  is the direction between a fluid node  $n_1$  and a solid node  $n_2$ , the bounce-back rule requires that the incoming fluid particle from  $n_1$  to  $n_2$  be reflected back along the direction it came from, i.e.,

$$f_{-i}(\mathbf{x}, t + \Delta t) = f_i(\mathbf{x}, t_+), \quad (5.24)$$

where  $-i$  denotes the opposite direction of  $i$ . The bounce back rule is illustrated in figure 5.4. This simple rule ensures that no tangential velocity exists along the fluid-wall interface, thereby a non-slip condition is imposed, and can be extended to any shapes or objects in a fluid flow (Han et al., 2007a; Zou and He, 1997). The slip boundary conditions have similar treatment to the

## 5.1 Fluid simulation using lattice Boltzmann method

47

non-slip condition, except that the distribution functions are reflected in the boundary instead of bounce-back ([Succi, 2001](#)). 1  
2

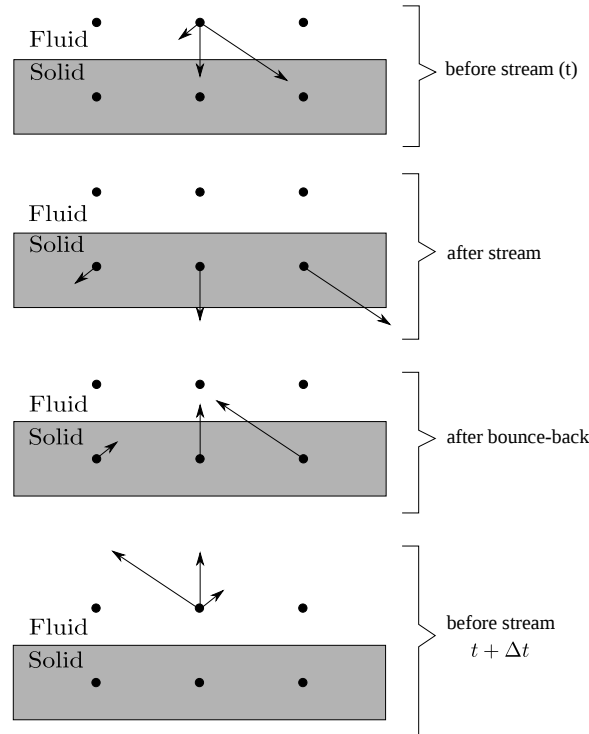


Figure 5.4 Half-way bounce back algorithm for the  $D2Q9$  model adopted after [Sukop and Thorne \(2006\)](#).

## Pressure and velocity boundary condition

The pressure (Dirichlet) boundary condition can be imposed in lattice Boltzmann by specifying a fluid density at the pressure boundary ([Zou and He, 1997](#)). To impose a pressure boundary along the  $y$ -direction (for example, consider the left hand side inlet boundary in figure 5.5), a density  $\rho = \rho_{in}$  is specified from which the velocity is computed. The vertical component of the velocity on the boundary is set as zero,  $u_y = 0$ . After streaming,  $f_2, f_3, f_4, f_6$ , and  $f_7$  are known,  $u_x$  and  $f_1, f_5, f_8$  are to be determined from [eq. 5.2](#) as 3  
4  
5  
6  
7  
8  
9

$$f_1 + f_5 + f_8 = \rho_{in} - (f_0 + f_2 + f_3 + f_4 + f_6 + f_7) \quad (5.25) \quad 10$$

$$f_1 + f_5 + f_8 = \rho_{in} u_x + (f_3 + f_6 + f_7) \quad (5.26) \quad 11$$

$$f_5 - f_8 = f_2 - f_4 + f_6 - f_7, \quad (5.27) \quad 12$$

<sup>1</sup> Consistency of equations (5.25) and (5.26) gives

$$\text{2} \quad u_x = 1 - \frac{[f_0 + f_2 + f_4 + 2 * (f_3 + f_6 + f_7)]}{\rho_{in}}. \quad (5.28)$$

<sup>3</sup> The bounce-back rule for the non-equilibrium part of the particle distribution normal to the  
<sup>4</sup> inlet is used to find  $f_1 - f_1^{eq} = f_3 - f_3^{eq}$ . The values of  $f_5$  and  $f_8$  can be obtained from  $f_1$ :

$$\begin{aligned} \text{5} \quad f_1 &= f_3 + \frac{2}{3}\rho_{in}u_x \\ \text{6} \quad f_5 &= f_7 - \frac{1}{2}(f_2 - f_4) + \frac{1}{6}\rho_{in}u_x \\ \text{7} \quad f_8 &= f_6 + \frac{1}{2}(f_2 - f_4) + \frac{1}{6}\rho_{in}u_x. \end{aligned} \quad (5.29)$$

<sup>9</sup> The corner node at inlet needs some special treatment. Considering the bottom node at inlet  
<sup>10</sup> as an example, after streaming,  $f_3, f_4, f_7$  are known;  $\rho$  is defined, and  $u_x = u_y = 0$ . The particle  
<sup>11</sup> distribution functions  $f_1, f_2, f_5, f_6$ , and  $f_8$  are to be determined. The bounce-back rule for the  
<sup>12</sup> non-equilibrium part of the particle distribution normal to the inlet and the boundary is used to  
<sup>13</sup> find

$$\text{14} \quad f_1 = f_3 + (f_1^{eq} - f_3^{eq}) = f_3 \quad (5.30)$$

$$\text{15} \quad f_2 = f_4 + (f_1^{eq} - f_3^{eq}) = f_4. \quad (5.31)$$

<sup>17</sup> Using these we can compute

$$\text{18} \quad f_5 = f_7 \quad (5.32)$$

$$\text{19} \quad f_6 = f_8 = \frac{1}{2}[\rho_{in} - (f_1 + f_2 + f_3 + f_4 + f_5 + f_6 + f_7 + f_8)]. \quad (5.33)$$

<sup>21</sup> Similar procedure can be applied to the top inlet node and the outlet nodes. Von Neumann  
<sup>22</sup> boundary conditions constrain the flux at the boundaries. A velocity vector  $u = [u_0 \ v_0]^T$  is  
<sup>23</sup> specified, from which the density and pressure are computed based on the domain. The velocity  
<sup>24</sup> boundary condition can be specified in a similar way (Zou and He, 1997). The pressure  
<sup>25</sup> and velocity boundary conditions contribute additional equation(s) to determine the unknown  
<sup>26</sup> distribution functions. In the case of velocity boundary, the boundary condition equation is  
<sup>27</sup> sufficient to determine the unknown distribution functions in the D2Q9 model, however the  
<sup>28</sup> pressure boundary conditions require additional constitutive laws to determine the unknown  
<sup>29</sup> distribution functions.

Table 5.1 LBM parameters used in simulating laminar flow through a circular pipe.

Parameter	Value
Density $\rho$	$1000 \text{ kg m}^{-3}$
Relaxation parameter $\tau$	0.51
Kinematic viscosity	$1 \times 10^{-6} \text{ m}^2 \text{ s}^{-1}$
Grid resolution ‘h’	$1^{-2} \text{ m}$
Number of steps	50,000
Error in predicting horizontal velocity	0.009 %

## 5.2 Validation of the lattice Boltzmann method

To verify the incompressible LBM model implemented in the above section, numerical simulation of a transient development of steady state Poiseuille flow in a straight channel is performed. At  $t = 0$ , the LBM water particles ( $\rho = 1000 \text{ kg/m}^3$ ) are simulated to flow through a channel of width ‘H’ (= 0.4 m) and simulation length ‘L’ (2.5H) under constant body force. Periodic boundary conditions are applied at either end of the channel and the pressure gradient is set to zero, which simulates the condition of a continuous flow of fluid in a closed circular pipe. The length ‘L’ has no effect on the simulation as no streamwise variation is detected in the solution. The parameters adopted in LBM simulation are presented in table 5.1. Sufficient time is allowed for the flow to travel beyond the required development length so that the flow is laminar (Durst et al., 2005). The development length  $X_D$  required for a flow to be fully laminar is

$$X_D/H = [(0.619)^{1.6} + (0.0567R_e)^{1.6}]^{1/1.6}, \quad (5.34)$$

where  $R_e$  is the Reynolds number. The velocity profile at steady state is presented in figure 5.5. A maximum horizontal velocity of  $0.037863 \text{ m s}^{-1}$  is observed along the center-line of the channel. The maximum horizontal velocity is compared with the closed-form based on the Haygen-Poiseuille flow equation for no-slip boundary condition (Willis et al., 2008)

$$U_x = \frac{\Delta P}{2\mu L} \left[ \frac{H^2}{4} - y^2 \right], \quad (5.35)$$

where  $v_x$  is the horizontal velocity (m/s);  $\Delta P$  is the pressure gradient,  $\mu$  dynamic viscosity of the fluid. LBM predicts the maximum horizontal velocity within an error of 0.009 %.

In order to further validate the accuracy of the lattice Boltzmann code, the transient development of the Poiseuille’s flow is compared with the CFD simulation performed using ANSYS Fluent. Finite Volume Method is a common CFD technique, which involves solving

- 1 the governing partial differential equation (Navier-Stokes) over the discretised control volume.  
 2 This guarantees the conservation of fluxes over a particular control volume. The finite volume  
 3 equations yield governing equations of the form

4

$$\frac{\partial}{\partial t} \int \int \int Q dV + \int \int F dA = 0, \quad (5.36)$$

5

- 6 where  $Q$  is the vector of conserved variables,  $F$  is the vector of fluxes in the Navier-Stokes  
 7 equation,  $V$  is the volume of control volume element, and  $A$  is the surface area of the control  
 8 volume element.

9 A 2D rectangular plane of length 1 m and height 0.04 m is discretised into 400 cells  
 10 of size  $1^{-2}$  m (see figure 5.6). A constant velocity is applied at the inlet. Water ( $\rho =$   
 11  $998.2 \text{ kg/m}^3$ , viscosity ' $\eta'$  =  $1 \times 10^{-3} \text{ Ns/m}^2$ ) is allowed to flow through the channel and  
 12 it develops into a fully laminar flow. The least squares approach was adopted to solve the  
 13 gradient, and a maximum of 100 iteration steps were carried out until the solution converged.

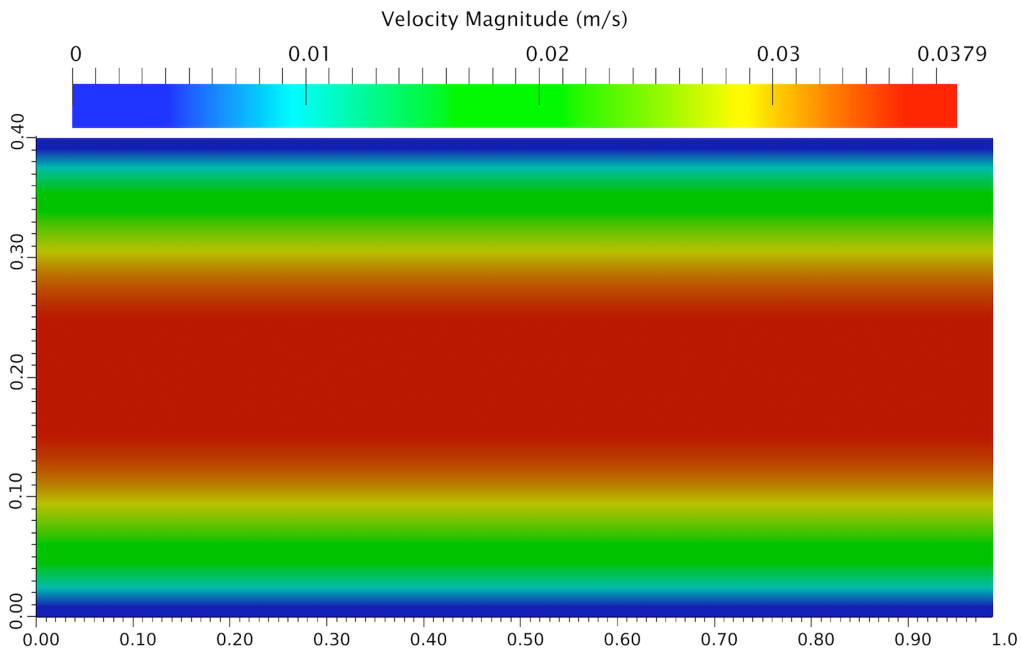


Figure 5.5 Velocity profile: LBM Simulation of a laminar flow through a channel.

14 The velocity profile obtained from the CFD simulation at cross-section ‘L/4’ is shown  
 15 in figure 5.7. Figure 5.8 compares the development of computed velocity profiles with the  
 16 analytical solution. At normalised time  $t = 1$ , the flow approaches steady state. It can be  
 17 observed that LBM has excellent agreement with CFD and the analytical solution at various  
 18 stages of flow evolution.

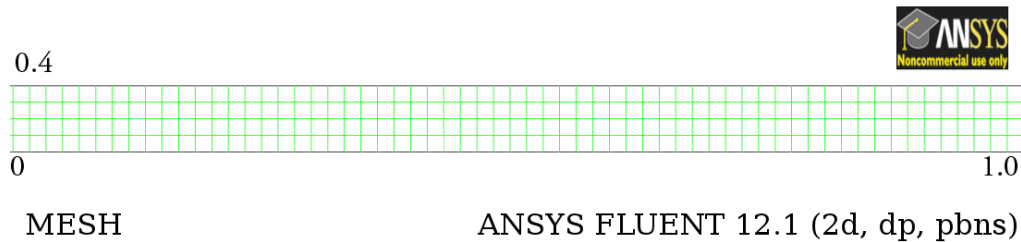


Figure 5.6 Finite Volume mesh used in the CFD analysis of laminar flow through a channel.

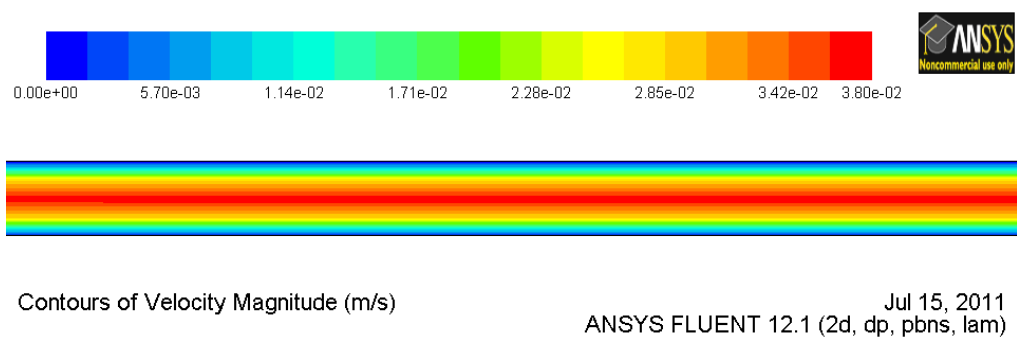


Figure 5.7 Velocity profile: CFD analysis of laminar flow through a channel.

In order to study the capability of the lattice Boltzmann technique to simulate fluid–solid interaction, LB simulation of a fluid flow around a rectangular obstacle is compared with the CFD technique. A solid wall of height ‘H/2’ is placed at length ‘L/4’ in the channel. Bounce-back algorithm is employed to model the fluid-wall interaction in LBM. In the CFD model, the control volume is discretised into 10,000 cells. A constant velocity is applied in the inlet and the horizontal velocity profile is recorded. Both, CFD and LBM simulations were performed to study the influence of a solid wall on the fluid flow behaviour.

The horizontal velocity profile obtained after 50,000 LBM iterations is presented in figure 5.9. LBM is able to capture the velocity shedding around the edges of the wall. The velocity profile obtained from the CFD analysis is presented in figure 5.10. The horizontal velocity profile at ‘L/4’ at  $t = 1$  is shown in figure 5.11. The maximum horizontal velocity from the CFD analysis is 0.3% higher in comparison with the LBM simulation. The discrepancy in the horizontal velocity profile (figure 5.11) can be attributed to the relaxation parameter used in the LBM, which is obtained by a trial and error procedure. The velocity profile obtained from the LBM simulation compares qualitatively with the FE analysis performed by [Zhong and Olson \(1991\)](#). Thus, it can be concluded that the lattice Boltzmann method is a suitable form of numerical representation of the Navier-Stokes equation to model fluid – solid interactions.

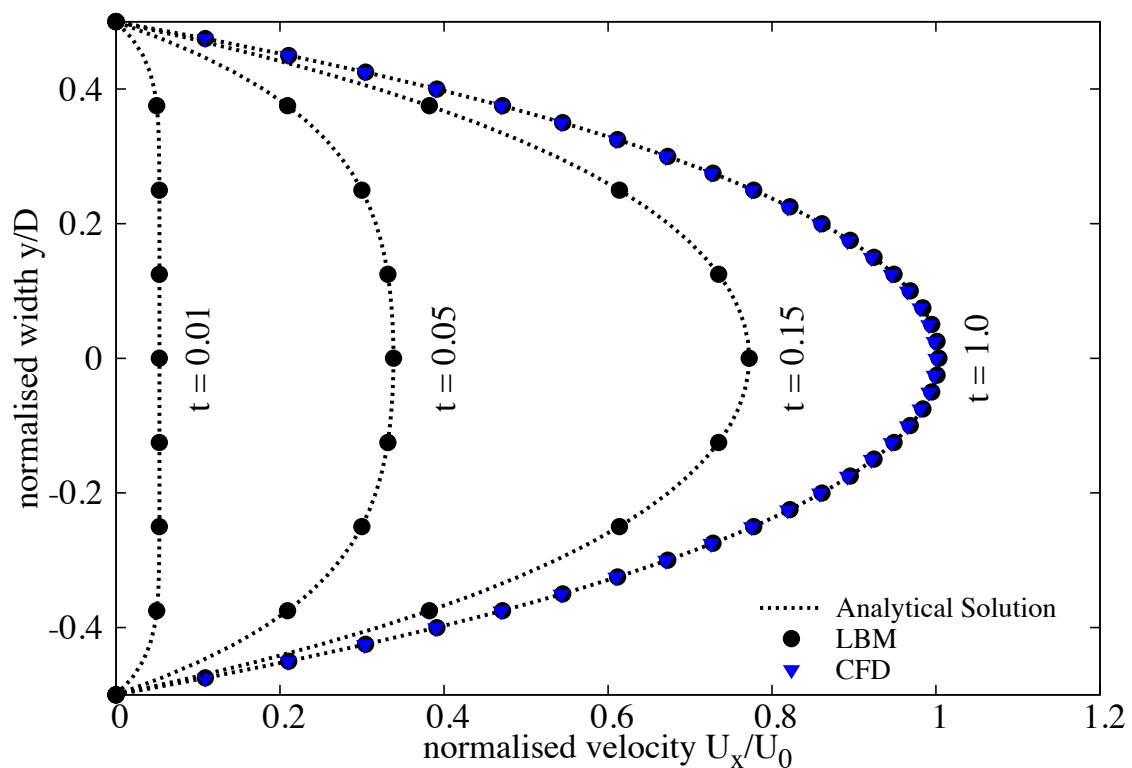


Figure 5.8 Development of the Poiseuille velocity profile in time: comparison between LBM simulation, CFD simulation and the analytical solution. Time is made dimensionless by  $H/U_0$ .

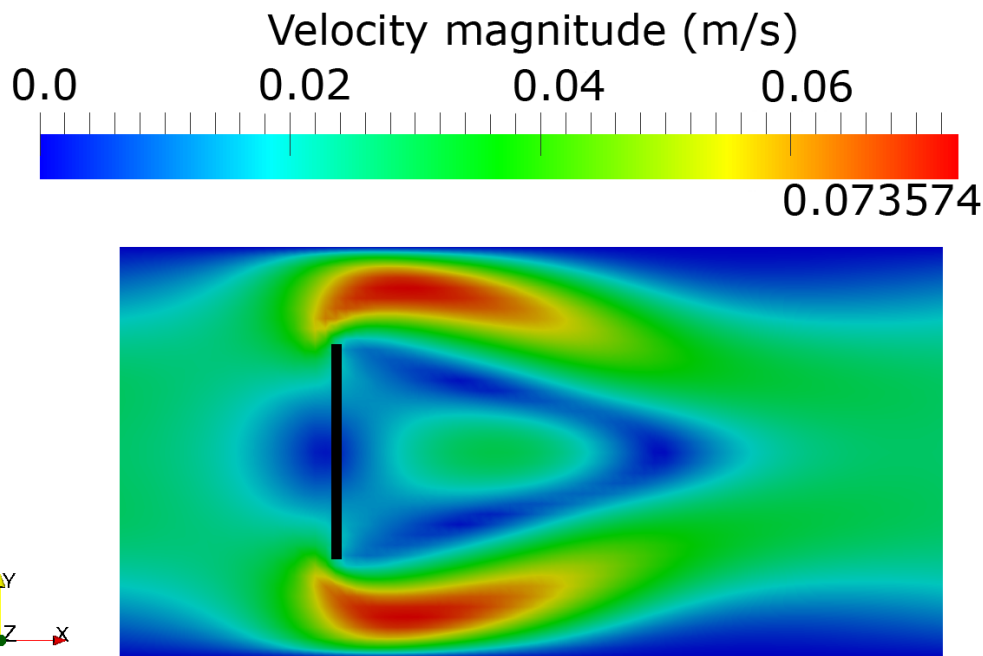


Figure 5.9 LBM simulation of velocity profile for a laminar flow through a pipe with an obstacle at L/4.

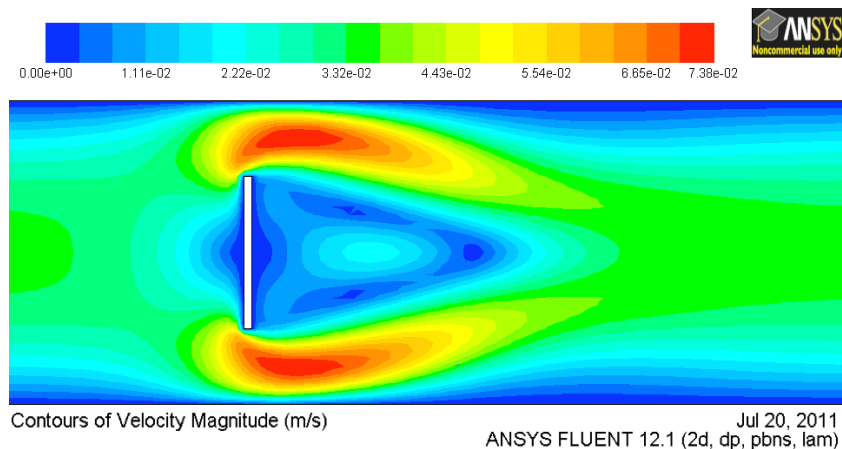


Figure 5.10 CFD simulation of velocity contour for a laminar flow through a pipe with an obstacle at L/4.

### 5.3 Turbulence in lattice Boltzmann method

The above formulation of lattice Boltzmann has been successfully applied to many fluid flow problems, however it is restricted to flows with low Reynolds number. Modelling fluids with low viscosity like water and air remains a challenge, necessitating very small values of  $h$ , and/or  $\tau$  very close to 0.5 (He et al., 1997). The standard lattice Boltzmann can deal with laminar

1

2

3

4

5

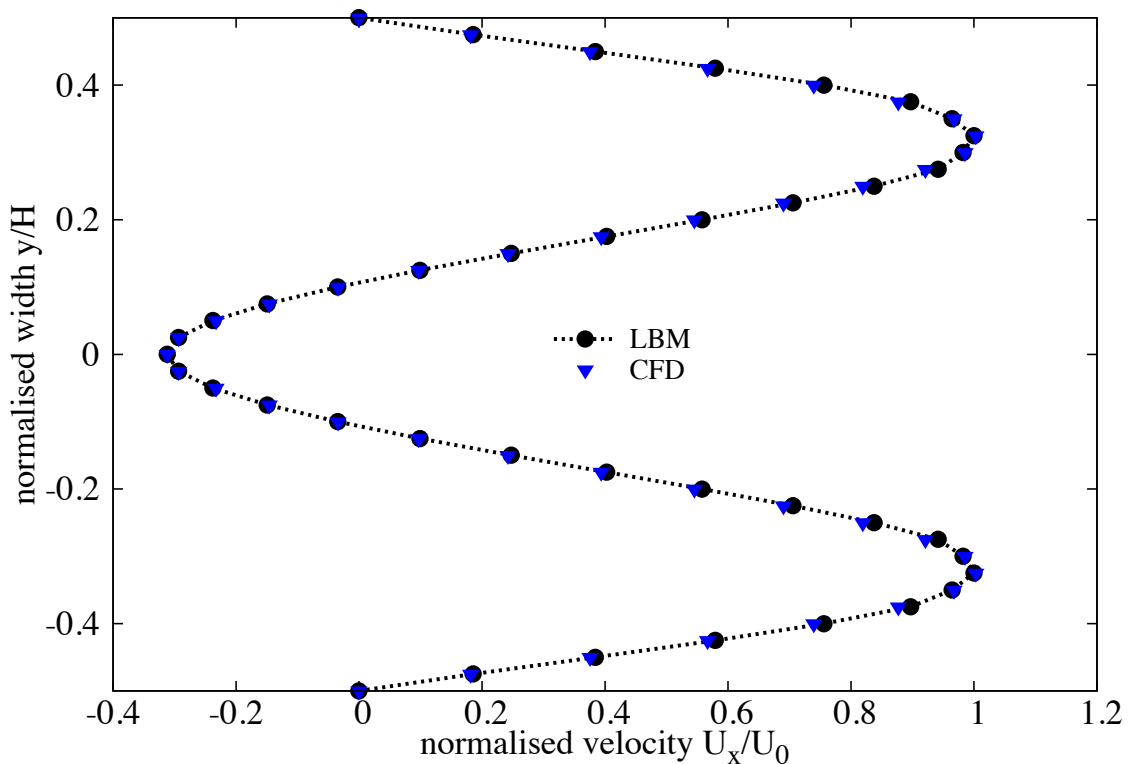


Figure 5.11 LBM and CFD simulation of a flow around an obstacle.

flows, while practical problems with small kinematic viscosity are often associated with flows having large Reynolds numbers, i.e. flows which are unsteady or turbulent in nature. The turbulent flows are characterised by the occurrence of eddies with multiple scales in space, time and energy.

The large eddy simulation (LES) is the most widely adopted approach to solve turbulent flow problems. It directly solves the large scale eddies, which carry the predominant portion of the energy, and the smaller eddies are modelled using a sub-grid approach. The separation of scales is achieved by filtering of the Navier-Stokes equations, from which the resolved scales are directly obtained. The unresolved scales are modelled by a one-parameter Smagorinski sub-grid methodology, which assumes that the Reynolds stress tensor is dependent only on the local strain rate (Smagorinsky, 1963). It involves parametrising the turbulent energy dissipation in the flows, where the larger eddies extract energy from the mean flow and ultimately transfer some of it to the smaller eddies which, in turn, pass the energy to even smaller eddies, and so on up to the smallest scales. At the smallest scale, the eddies convert the kinetic energy into the internal energy of the fluid. At this scale, the viscous friction dominates the flow (Frisch and Kolmogorov, 1995).

In the Smagorinsky model, the turbulent viscosity  $\nu$  is related to the strain rate  $S_{ij}$  and a filtered length scale ‘ $h$ ’ as follows

$$S_{ij} = \frac{1}{2}(\partial_i u_j + \partial_j u_i) \quad (5.37)$$

$$\nu_t = (S_c h)^2 \bar{S} \quad (5.38)$$

$$\bar{S} = \sqrt{\sum_{i,j} \tilde{S}_{i,j} \tilde{S}_{i,j}}, \quad (5.39)$$

where  $S_c$  is the Smagorinsky constant, which is close to 0.03 (Yu et al., 2005). The effect of the unresolved scale motion is taken into account by introducing an effective collision relaxation time scale  $\tau_t$ , so that the total relaxation time  $\tau_*$  is written as

$$\tau_* = \tau + \tau_t, \quad (5.40)$$

where  $\tau$  and  $\tau_t$  are respectively the standard relaxation times corresponding to the true fluid viscosity  $\nu$  and the turbulence viscosity  $\nu_t$ , defined by a sub-grid turbulence model. The new

1 viscosity  $\nu_*$  corresponding to  $\tau_*$  is defined as

$$\begin{aligned} 2 \quad \nu_* &= \nu + \nu_t \\ 3 \quad &= \frac{1}{3}(\tau_* - \frac{1}{2})C^2\Delta t = \frac{1}{3}(\tau + \tau_t - \frac{1}{2})C^2\Delta t \end{aligned} \quad (5.41)$$

$$\begin{aligned} 4 \quad \nu_t &= \frac{1}{3}\tau_t C^2\Delta t. \\ 5 \end{aligned} \quad (5.42)$$

6 The Smagorinski model is easy to implement and the lattice Boltzmann formulation remains  
 7 unchanged, except for the use of a new turbulence-related viscosity  $\tau_*$ . The component  $s_1$  of  
 8 the collision matrix becomes  $s_1 = \frac{1}{\tau + \tau_t}$ .

9 The effectiveness of LBM-LES model in simulating unsteady flows is verified by modelling  
 10 the Kármán vortex street. In fluid dynamics, a Kármán vortex street is a repeating pattern of  
 11 vortices caused by unsteady separation of fluid flow around circular obstacles. A vortex street  
 12 will only be observed above a limiting value of Reynolds number of 90. The Reynolds number  
 13 is computed based on the cylinder diameter ‘D’ and the mean flow velocity  $U$  of the parabolic  
 14 inflow profile:

$$\begin{aligned} 15 \quad Re &= \frac{UD}{\nu}. \\ 16 \end{aligned} \quad (5.43)$$

16 LBM particles are simulated to flow through a 2D rectangular channel with an aspect ratio  
 17 ‘L/H’ of 2.5. A cylinder of diameter ‘d’ = 0.27H is placed at H/2. The pressure gradient at  
 18 the inlet and the outlet is varied to create flows with different mean velocities. Numerical  
 19 simulations of vortex shedding behind a circular obstacle are carried out for three different  
 20 fluid flow regimes (Reynolds number of 55, 75, and 112). The fully developed fluid flows for  
 21 different Reynolds numbers are shown in figure 5.12. It can be observed from figure 5.12 that  
 22 the von Kármán vortex street can only be observed at high a Reynolds number of 112 ( $Re >$   
 23 90), which shows the ability of the LBM turbulence model to capture instabilities in fluid flow.

24 One important quantity taken into account in the present analysis is the Strouhal number  $St$ ,  
 25 a dimensionless number describing oscillating unsteady flow dynamics. The Strouhal number  
 26 is computed from the cylinder diameter D, the measured frequency of the vortex shedding f,  
 27 and the maximum velocity  $U_{max}$  at the inflow plane:

$$\begin{aligned} 28 \quad St &= \frac{fD}{U_{max}}. \\ 29 \end{aligned} \quad (5.44)$$

29 The characteristic frequency  $f$  is determined by a spectral analysis (Fast Fourier Transform -  
 30 FFT) of time series of the fluid pressure. Table 5.2 shows that the Strouhal numbers computed  
 31 from LBM simulations have a very good agreement with FVM results obtained by Breuer et al.  
 32 (2000). This shows the ability of LBM-LES in capturing unsteady flow dynamics.

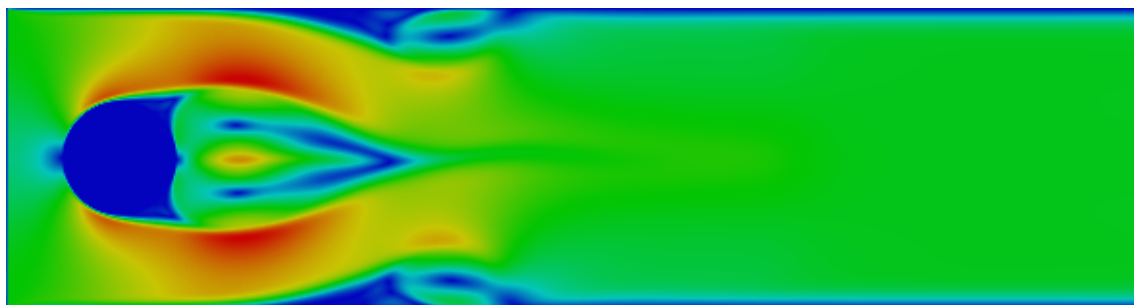
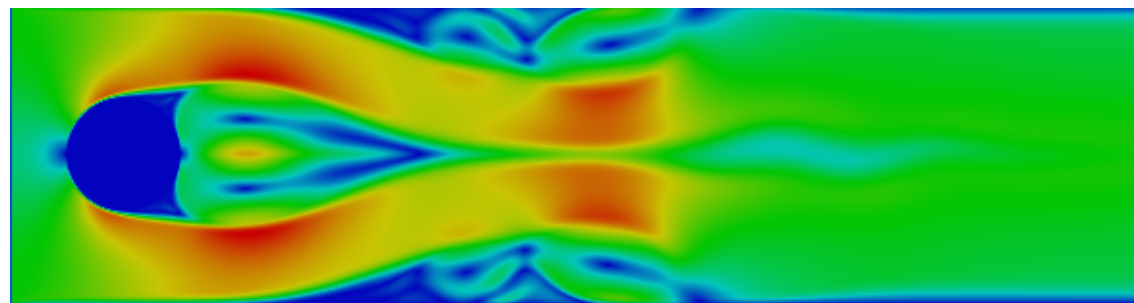
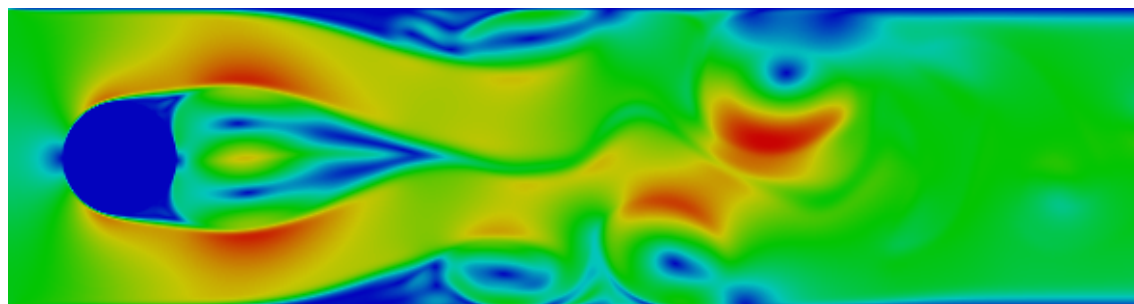
(a)  $\text{Re} = 55$ (b)  $\text{Re} = 75$ (c)  $\text{Re} = 112$ 

Figure 5.12 Kármán vortex street

Table 5.2 Computed Strouhal number for fluid flows with different Reynolds number

Reynolds number	Strouhal number	
	LBM	FVM
55	0.117	0.117
75	0.128	0.129
112	0.141	0.141

\* FVM results are from [Breuer et al. \(2000\)](#)

## 1 5.4 Coupled LBM and DEM for fluid-grain interactions

2 Modelling fluid–grain interactions in submarine landslides requires the ability to simulate  
 3 the interactions at the dynamic fluid – solid boundaries. In principle, the conventional FE  
 4 and FVM based approaches for solving the Navier-Stokes equations with moving boundaries  
 5 and/or structural interaction ([Bathe and Zhang, 2004](#)) can be applied to particle fluid interaction  
 6 problems. The common feature of these approaches is to model the interaction between the  
 7 fluid and the solid to a high degree of accuracy. However, the main computational challenge  
 8 is the need to continuously generate new geometrically adapted meshes to circumvent severe  
 9 mesh distortion, which is computationally very intensive ([Han et al., 2007b](#)).

10 The lattice Boltzmann approach has the advantage of accommodating large particle sizes  
 11 and the interaction between the fluid and the moving grains can be modelled through relatively  
 12 simple fluid - grain interface treatments. Further, employing DEM to account for the grain/grain  
 13 interaction naturally leads to a combined LB – DEM solution procedure. The Eulerian nature  
 14 of the lattice Boltzmann formulation, together with the common explicit time step scheme of  
 15 both LBM and DEM makes this coupling strategy an efficient numerical procedure for the  
 16 simulation of fluid – grain systems.

17 LBM – DEM technique is a powerful predictive tool for gaining insights into many fun-  
 18 damental physical phenomena in fluid-solid systems. Such a coupled methodology was first  
 19 proposed by ([Cook et al., 2004](#)) for simulating fluid-grain systems dominated by fluid-grain  
 20 and grain-grain interactions. To capture the actual physical behaviour of the fluid-grain system,  
 21 it is essential to model the boundary condition between the fluid and the grain as a non-slip  
 22 boundary condition, i.e. the fluid velocity near the grain should be similar to the velocity of  
 23 the grain boundary. The soil grains in the fluid domain are represented by lattice nodes. The  
 24 discrete nature of the lattice will result in stepwise representations of the surfaces, which are  
 25 otherwise circular, this is neither accurate nor smooth, unless sufficiently small lattice spacing  
 26 is adopted.

## Modified bounce back rule

To accommodate the movement of solid particles in the commonly adopted bounce-back rule (see section 5.1.3), Ladd (1994) modified the ‘no-slip’ rule for a given boundary link  $i$  to be

$$f_i(\mathbf{x}, t + \Delta t) = f_i(\mathbf{x}, t_+) - \alpha_i e_i \cdot v_b \quad (\alpha_i = 6w_i \rho / C_s^2), \quad (5.45)$$

where  $f_i(\mathbf{x}, t_+)$  is the post collision distribution at the fluid or solid boundary node  $\mathbf{x}$ , and  $v_b$  is the velocity at the nominal boundary point at the middle of the boundary link  $i$

$$\mathbf{v}_b = \mathbf{v}_c + \boldsymbol{\omega} \times (\mathbf{x} + e_i \Delta t / 2 - \mathbf{x}_c), \quad (5.46)$$

in which  $v_c$  and  $\boldsymbol{\omega}$  are the translational and angular velocities at the mass centre of the solid particle, respectively.  $\mathbf{x}_c$  and  $\mathbf{x} + e_i \Delta t / 2$  are the coordinates of the centre and the nominal boundary point, respectively. The impact force on the soil grain from the link is defined as

$$\mathbf{F}_i = 2[f_i(\mathbf{x}, t_+) - \alpha_i e_i \cdot v_b] / \Delta t. \quad (5.47)$$

The corresponding torque  $\mathbf{T}_i$ , produced by the force with respect to the centre of the particle is computed as

$$\mathbf{T}_i = \mathbf{r}_c \times \mathbf{F}_i (\mathbf{r}_c = \mathbf{x} + \mathbf{e}_i \Delta t / 2 - \mathbf{x}_c). \quad (5.48)$$

Then the total hydrodynamic force and torque exerted on the particle can be calculated by summing up the forces and torques from all the related boundary links:

$$\begin{aligned} \mathbf{F} &= \sum_i \mathbf{F}_i \\ \mathbf{T} &= \sum_i \mathbf{T}_i. \end{aligned} \quad (5.49)$$

Ladd and Verberg (2001) described a methodology that minimises the oscillations resulting from soil grains crossing lattices at a very high speed. The methodology involves combining several extensions for the fluid simulation like the treatment of moving curved boundaries with the scheme of Yu et al. (2003) and a fluid/grain force interaction method with the momentum exchange method of Ladd and Verberg (2001). The simulation of the moving curved grain surfaces results in the intersection of links between two nodes at arbitrary distances (Iglberger et al., 2008). These distance values are referred to as delta values:

$$\delta = \frac{\text{Distance between fluid node and soil surface}}{\text{Distance between fluid node and soil node}} \in [0, 1]. \quad (5.50)$$

1 For each pair of a fluid and grain node, a delta value has to be calculated. Delta values of zero  
 2 are not possible as the nodes on the surface are considered as solid nodes. The algorithm for  
 3 computation of the  $\delta$  value is presented in [Iglberger et al. \(2008\)](#). Figure 5.13 shows the three  
 4 possible situations for delta values between 0 and 1. The fluid particles in LBM are always  
 5 considered to be moving at the rate of one lattice per time step ( $\delta\mathbf{x}/\delta t$ ), for delta values smaller  
 6 than 0.5. For  $\delta$  values larger than 0.5, the fluid particles would come to rest at an intermediate  
 7 node  $\mathbf{x}_i$ . In order to calculate the reflected distribution function in node  $\mathbf{x}_f$ , an interpolation  
 8 scheme has to be applied. The linear interpolation scheme of [Yu et al. \(2003\)](#) is used in the  
 9 present study, which uses a single equation, irrespective of the value of  $\delta$  being smaller or  
 10 larger than 0.5, to the reflected distribution function that is computed as

$$\begin{aligned} 11 \quad f_{\bar{\alpha}}(\mathbf{x}_f, t + \delta t) = & \frac{1}{1 + \delta} \cdot [(1 - \delta) \cdot f_{\alpha}(\mathbf{x}_f, t + \delta t) + \delta \cdot f_{\alpha}(\mathbf{x}_b, t + \delta t) \\ 12 \quad & + \delta \cdot f_{\bar{\alpha}}(\mathbf{x}_{f2}, t + \delta t) - 2w_a \rho_w \frac{3}{c^2} e_a \cdot \mathbf{u}_w], \end{aligned} \quad (5.51)$$

14 where  $w_{\alpha}$  is the weighting factor,  $\rho_w$  is the fluid density in node  $\mathbf{x}_f$ , and  $\mathbf{u}_w$  is the velocity at the  
 15 bounce-back wall. In order to couple the fluid-grain interaction, the LBM approach is extended  
 16 by adopting a force integration scheme, to calculate the fluid force acting on the grain surface,  
 17 and the momentum exchanged method described earlier. The physical force acting on grain  
 18 agglomerates is calculated as the sum over all fluid/grain node pairs, resulting in

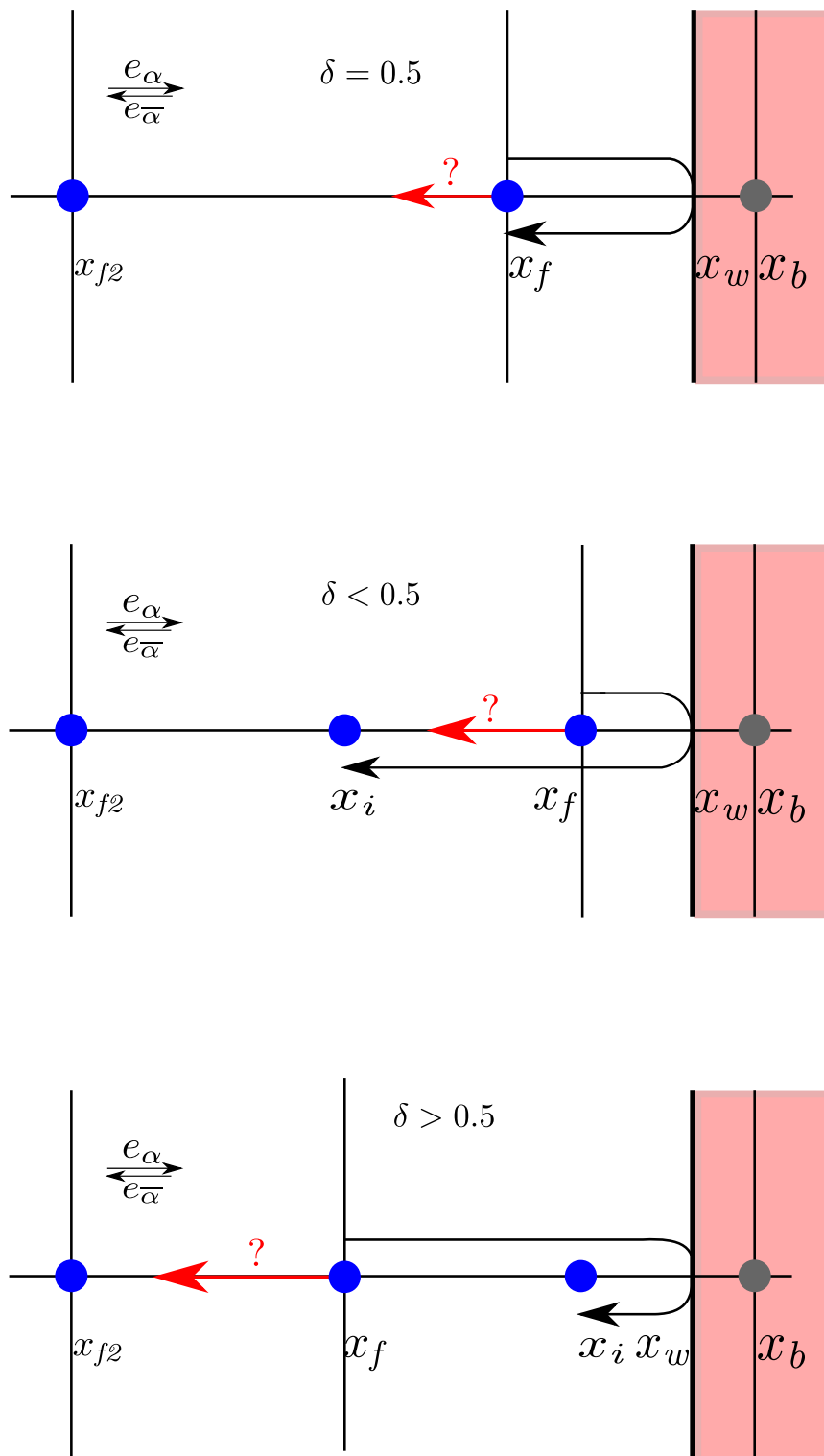
$$19 \quad F = \sum_{\mathbf{x}_b} \sum_{\alpha=1}^{19} \mathbf{e}_{\alpha} [f_{\alpha}(\mathbf{x}_b, t) + f_{\bar{\alpha}}(\mathbf{x}_f, t)] \delta\mathbf{x}/\delta t. \quad (5.52)$$

20 After the force calculations, the coupled rigid body physics can be simulated in order to move  
 21 the grains / grain-agglomerates according to the applied forces. The total hydrodynamic forces  
 22 and torque exerted on a grain can be computed as ([Cook et al., 2004](#); [Noble and Torczynski,](#)  
 23 [1998](#))

$$24 \quad \mathbf{F}_f = Ch \left[ \sum_n \left( \beta_n \sum_i f_i^m e_i \right) \right] \quad (5.53)$$

$$25 \quad \mathbf{T}_f = Ch \left[ \sum_n (\mathbf{x}_n - \mathbf{x}_c) \times \left( \beta_n \sum_i f_i^m e_i \right) \right]. \quad (5.54)$$

27 The summation is over all lattice nodes covered by the soil grain, and  $\mathbf{x}_n$  represents the  
 28 coordinate of the lattice node  $n$ .

Figure 5.13 Bounce back boundaries for different values of  $\delta$

When grains are not in direct contact among themselves, but are driven by the fluid flow and body force, i.e. gravity, their motion can be determined by Newton's equation of motion

$$m\mathbf{a} = \mathbf{F}_f + m\mathbf{g} \quad (5.55)$$

$$J\ddot{\theta} = \mathbf{T}_f, \quad (5.56)$$

where  $m$  and  $J$  are respectively the mass and the moment of inertia of a grain,  $\ddot{\theta}$  is the angular acceleration,  $\mathbf{g}$  is the gravitational acceleration,  $\mathbf{F}_f$  and  $\mathbf{T}_f$  are respectively the hydrodynamic forces and torque. The equation can be solved numerically by an explicit numerical integration, such as the central difference scheme.

The interaction between the soil grains, and the soil grains with the walls are modelled using the DEM technique. To solve the coupled DEM–LBM formulation, the hydrodynamic force exerted on soil grains and the static buoyancy force are considered by reducing the gravitational acceleration to  $(1 - \rho/\rho_s)\mathbf{g}$ , where  $\rho_s$  is the density of the grains. When taking into account all forces acting on an element, the dynamic equations of DEM can be expressed as

$$m\mathbf{a} + c\mathbf{v} = \mathbf{F}_c + \mathbf{F}_f + m\mathbf{g}, \quad (5.57)$$

where  $\mathbf{F}_c$  denotes the total contact forces from other elements and/or the walls, and  $c$  is a damping coefficient. The term  $c\mathbf{v}$  represents a viscous force that accounts for the effect of all possible dissipation forces in the system including energy lost during the collision between grains. Considering a linear contact model

$$\mathbf{F}_c = k_n\delta, \quad (5.58)$$

where  $k_n$  is the normal stiffness and  $\delta$  is the overlap, the critical time step associated with the explicit integration is determined as (He et al., 1997)

$$\Delta t_{cr} = 2(\sqrt{1 + \xi^2} - \xi)/\omega, \quad (5.59)$$

where  $\omega = \sqrt{k_n/m}$  is the local contact natural frequency and  $\xi = c/2m\omega$  is the critical damping ratio. The actual time step used for the integration of the Discrete Element equations is

$$\Delta t_D = \lambda \Delta t_{cr}. \quad (5.60)$$

The time step factor  $\lambda$  is chosen to be around 0.1 to ensure both stability and accuracy (He et al., 1997).

When combining the Discrete Element modelling of the grain interactions with the LB formulation, an issue arises. There are now two time steps:  $\Delta t$  for the fluid flow and  $\Delta t_D$  for the particles. Since  $\Delta t_D$  is normally smaller than  $\Delta t$ ,  $\Delta t_D$  is slightly reduced to a new value  $\Delta t_s$  so that  $\Delta t$  and  $\Delta t_s$  have an integer ratio  $n_s$

$$\Delta t_s = \frac{\Delta t}{n_s} \quad (n_s = [\Delta t / \Delta t_D] + 1). \quad (5.61)$$

This results in a sub-cycling time integration for the Discrete Element part. At every step of the fluid computation,  $n_s$  sub-steps of integration are performed for the Discrete Element Method (5.57) using the time step  $\Delta t_s$ . The hydrodynamic force  $\mathbf{F}_f$  is unchanged during the sub-cycling.

### 5.4.1 Draft, kiss and tumbling: Sedimentation of two grains

In multiphase flows, fundamental mechanisms of fluid – grain and grain – grain interactions are very important for accurately predicting the flow behaviours. The sedimentation of two circular grains in a viscous fluid serves as the simplest problem to study these two types of interactions, and many experimental and numerical studies have been carried out to investigate this behaviour (Komiwas et al., 2005; Wang et al., 2014). Fortes (1987) observed experimentally that in the sedimentation of two grains under gravity in a Newtonian fluid, the two grains would undergo the draft, kiss and tumbling (DKT) phenomenon.

The *draft*: grain 2 is first placed within the hydrodynamic drag above grain 1. As the hydrodynamic drag of grain 1 is a depression zone, grain 2 is attracted inside. The *kiss*: grain 2 increases its vertical velocity until it touches grain 1. The horizontal velocity of grain 1 increases and its vertical velocity decreases below that of grain 2. *Tumbling*: grain 2 having the same horizontal velocity and higher vertical velocity than grain 1, overtakes grain 1.

LBM-DEM simulation of two grains under gravity in a viscous Newtonian fluid reproduces the draft, kiss and tumble effect (see figure 5.14). They are in agreement with the experimental description of the DKT effect. For better understanding of the DKT effect, the time history of three distances between the grains (normalised to the diameter of the grain D) are tracked i.e., the difference in the transverse coordinates  $\delta_x/D$  and longitudinal coordinates  $\delta_y/D$  of the two grain centres, and the gap between the two surfaces  $\delta = \sqrt{\delta_x^2 + \delta_y^2} - 1$  (see figure 5.15c).

As shown in figure 5.14, grain 1 trails grain 2. As grain 2 approaches the depression zone, corresponding to negative fluid pressure behind grain 1, the velocity of the trailing grain increases as the grains approach closer, this is in agreement with the experimental description of the draft. Grain 2 increases its vertical velocity more than grain 1 until it touches grain 1. The kiss happens at a normalised time  $(t / \sqrt{(D/g)}) = 25$ . At this stage, the gap  $\delta$  between the

1 grains is zero, but the actual gap is about one lattice spacing for the LBM collision model. After  
 2 this time, the vertical velocity of grain 1 decreases and its horizontal velocity increases as the  
 3 grains tumble. At this stage, the grains still remain in contact, i.e., the gap remains unchanged  
 4  $\delta = 0$ . Subsequently, the two grains separate and move away from each other. Figure 5.15b  
 5 shows that the terminal velocities of the two grains are in good agreement with the terminal  
 6 velocity of a single grain found by an independent simulation and calculated using the empirical  
 7 Schiller and Nauman formula ([Komiwas et al., 2005](#)).

## 8 5.5 GP-GPU Implementation

9 Graphics Processing Unit (GPU) is a massively multi-threaded architecture that is widely  
 10 used for graphical and now non-graphical computations. Today's GPUs are general purpose  
 11 processors with support for an accessible programming interface. The main advantage of GPUs  
 12 is their ability to perform significantly more floating point operations (FLOPs) per unit time  
 13 than a CPU. General Purpose computations on GPUs (GPGPUs) often achieve speedups of  
 14 orders of magnitude in comparison with optimised CPU implementations.

15 A GPU consists of several *Streaming Multiprocessors* (SMs). Each SM contains 32 CUDA  
 16 processors. Each CUDA processor has a fully pipelined integer arithmetic logic unit (ALU)  
 17 and a floating point unit (FPU). The FPU complies with the IEEE 754-2008 industry standard  
 18 for floating-point arithmetic, capable of double precision computations. The SM schedules  
 19 work in groups of 32 threads called warps. Each SM features two warp schedulers and two  
 20 instruction dispatch units, allowing two warps to be issued and executed concurrently. Each  
 21 thread has access to both L1 and L2 caches, which improves the performance for programs  
 22 with random memory access.

23 The occupancy rate of the SPs, i.e. the ratio between the number of threads run and the  
 24 maximum number of executable threads, is an important aspect to take into consideration for  
 25 the optimisation of a CUDA kernel. Even though a block may only be run on a single SM, it is  
 26 possible to execute several blocks concurrently on the same SM. Hence, tuning the execution  
 27 grid layout allows one to increase the occupancy rate. Nevertheless, reaching the maximum  
 28 occupancy is usually not possible, as the threads executed in parallel on one SM have to share  
 29 the available registers ([Obrecht and Kuznik, 2011](#)).

30 Many-core processors are promising platforms for intrinsically parallel algorithms such as  
 31 the lattice Boltzmann method. Since the global memory for GPU devices shows high latency  
 32 and LBM is data intensive, the memory access pattern is an important issue for achieving good  
 33 performances. Whenever possible, global memory loads and stores should be coalescent and  
 34 aligned, but the propagation phase in LBM can lead to frequent misaligned memory accesses.

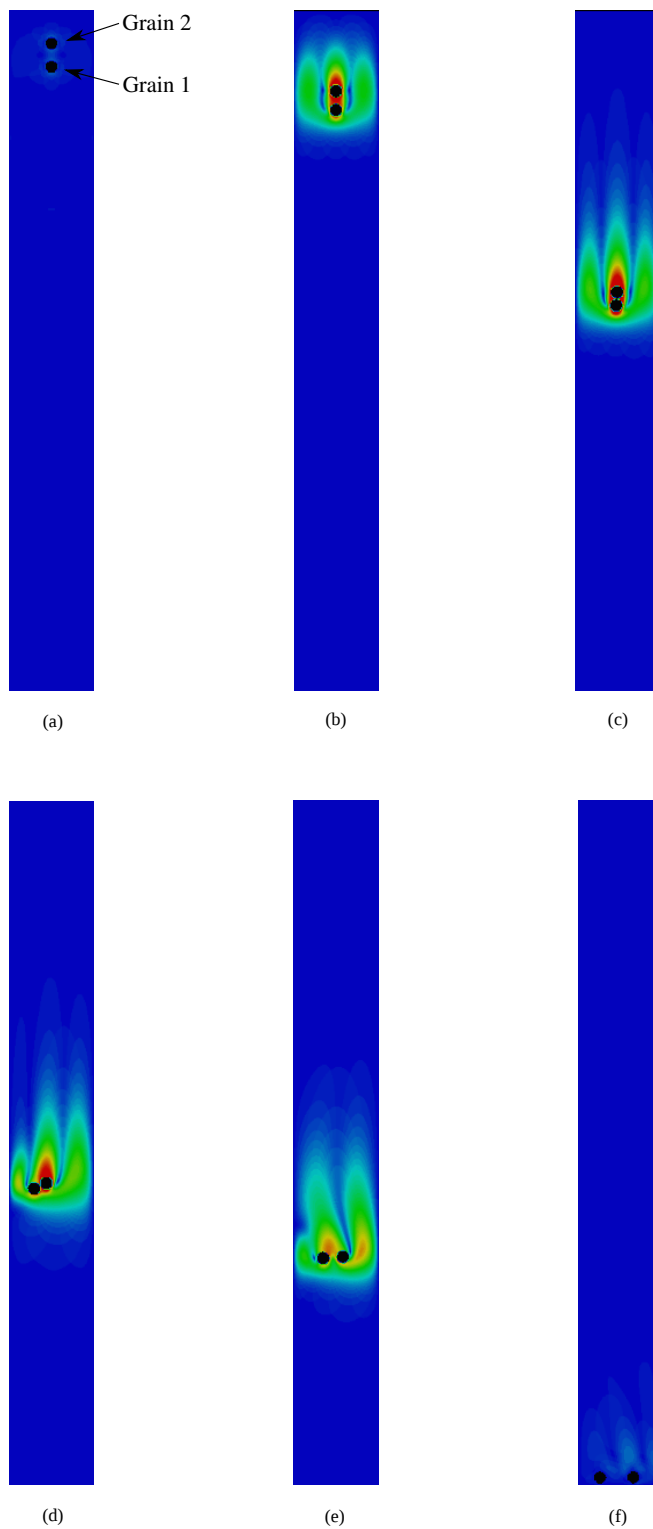


Figure 5.14 Time series of draft, kiss and tumble of two grains during sedimentation in a viscous fluid.

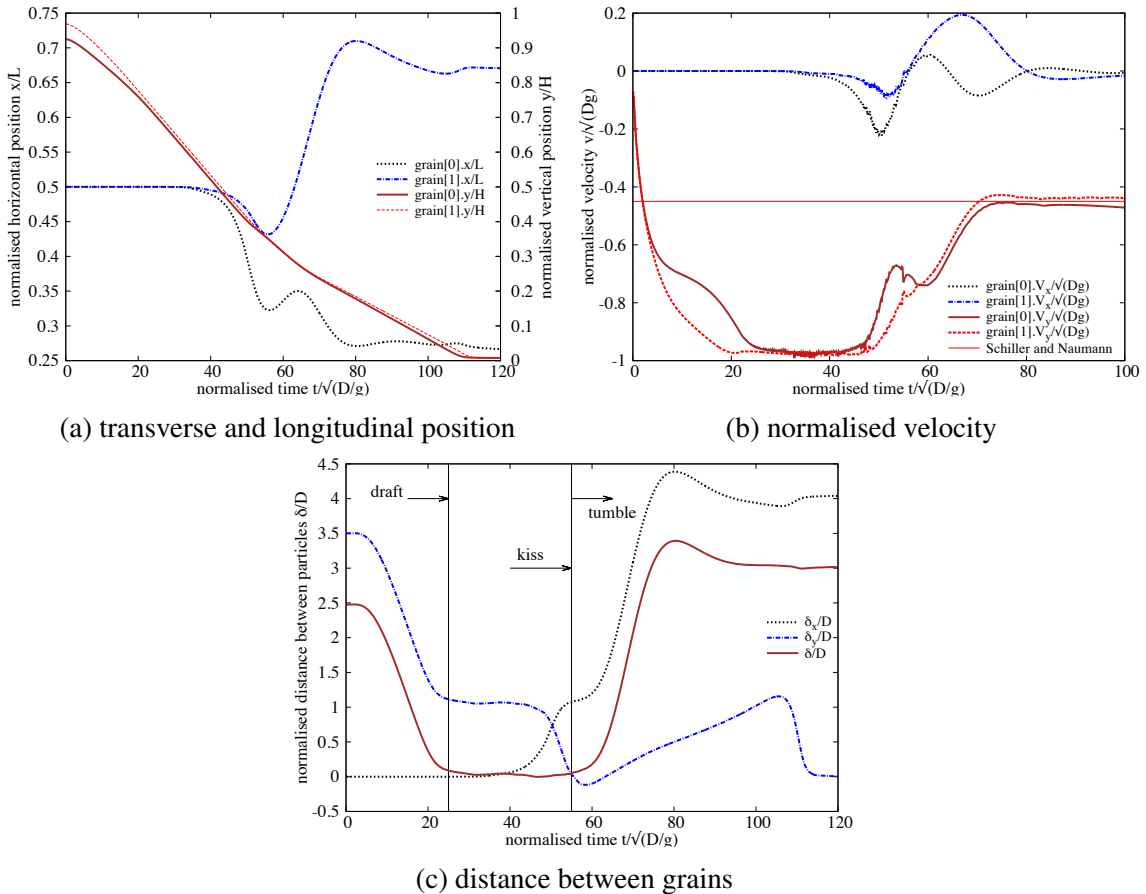


Figure 5.15 Time history of two circular grains during sedimentation.

Also, the data transfer between the host and the device is very expensive. In the present study, the LBM implementation follows carefully chosen data transfer schemes in global memory.

There are three ways to accelerate GPGPU applications: (a) Using ‘drop-in’ libraries, (b) using directives by exposing parallelism, and (c) using dedicated GPGPU programming languages. OpenACC (Open Accelerators) is an open GPU directives programming standard for parallel computing on heterogeneous CPU/GPU systems. Unlike conventional GPU programming languages, such as CUDA, OpenACC uses directives to specify parallel regions in the code and performance tuning works on exposing parallelism. OpenACC targets a host-directed execution model where the sequential code runs on a conventional processor and computationally intensive parallel pieces of code (kernels) run on an accelerator such as a GPU (see figure 5.16).

The original GPGPU LBM – DEM code was implemented in C using OpenACC API v1.0, which was released in November 2011. The current implementation in C++ uses OpenACC API v2.0a ([OpenACC-Members, 2013](#)) and has two compute constructs, the kernels construct and the parallel construct. LBM – DEM implementation predominantly uses the OpenACC gang and vector parallelism. The LBM – DEM code runs sequential and computationally less intensive functions on the CPU, OpenMP multi-threading is used when possible. Computationally intensive functions are converted to a target accelerator specific GPU parallel code. Schematics of a heterogeneous CPU/GPU system is shown in figure 5.16.

OpenACC offers kernel and parallel constructs to parallelise algorithms on CUDA kernels. The loop nests in a kernel construct are converted by the compiler into parallel kernels that run efficiently on a GPU. There are three steps to this process. The first is to identify the loops that can be executed in parallel. The second is to map that abstract loop parallelism onto a concrete hardware parallelism. In OpenACC terms, gang parallelism maps to grid-level parallelism (equivalent to a CUDA blockIdx), and vector parallelism maps to thread-level parallelism (equivalent to a CUDA threadIdx). The compiler normally maps a single loop across multiple levels of parallelism using strip-mining. Finally, in step three the compiler generates and optimizes the actual code to implement the selected parallelism mapping.

An OpenACC parallel construct creates a number of parallel threads that immediately begin executing the body of the parallel construct redundantly. When a thread reaches a work-sharing loop, that thread will execute some subset of the loop iterations, depending on the scheduling policy as specified by the program or at the runtime. The code generation and optimization for a parallel construct is essentially the same as for the kernel construct. A key difference is that unlike a kernel construct, the entire parallel construct becomes a single target parallel operation, aka a single CUDA kernel. Both constructs allow for automatic vectorization within the loops ([Wolfe, 2012](#)).

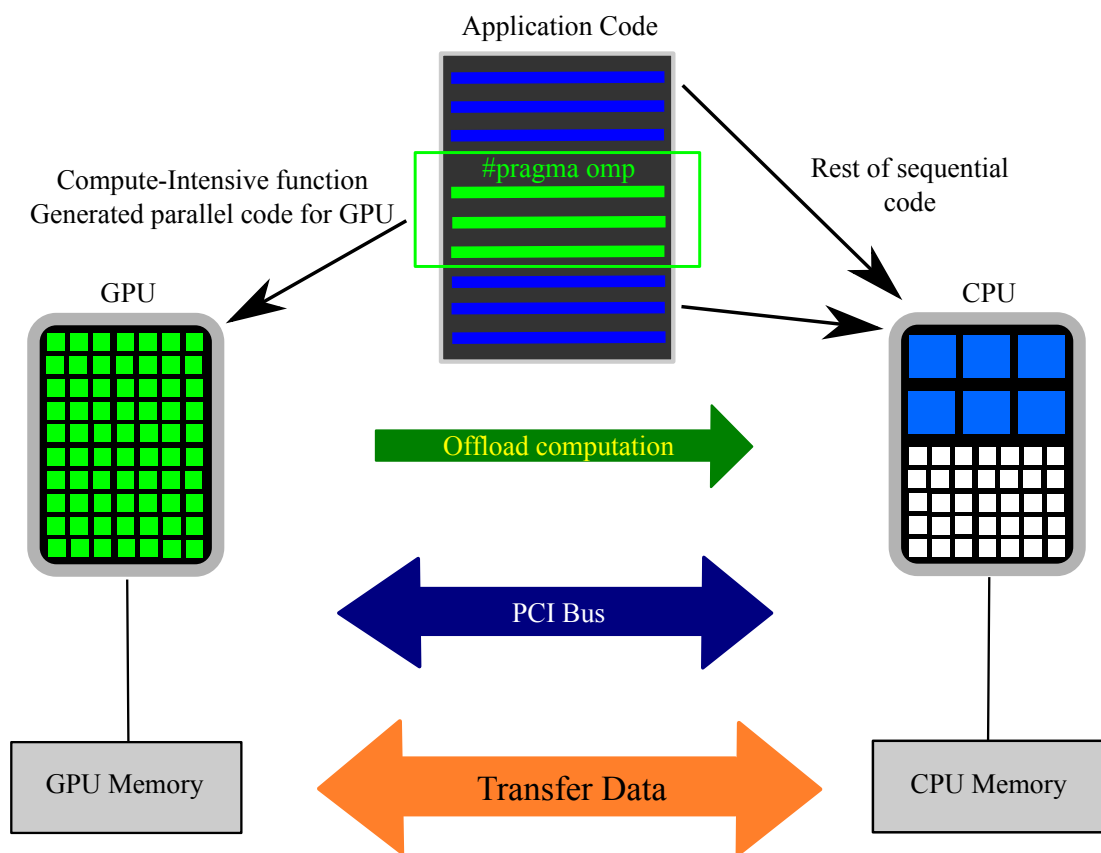


Figure 5.16 Schematics of a heterogeneous CPU/GPU system.

An excerpt from the LBM-DEM code showing the OpenACC GPU implementation of the hydrodynamic force computation is presented in Listing 5.1. The kernels loop construct tells the compiler to map the body of the following loop into an accelerator kernel. The GPU implementation uses a two-dimensional grid splitting the iterations across both the vector and gang modes. The kernel is mapped to a vector mode mapped (aligned with CUDA threadidx% $x$ ) with a vector length (thread block size) of 128. The kernel is also mapped to gang parallelism, aligned to CUDA blockidx% $x$ , to avoid partition camping by mapping the stride-1 loop to the  $x$  dimension. The compiler strip-mines the loop into chunks of 256 iterations, mapping the 256 iterations of a chunk in vector mode across the threads of a CUDA thread block, and maps the  $n/256$  chunks in gang mode across the thread blocks of the CUDA grid. The consecutive iterations ( $i$  and  $i+1$ ), which refer to contiguous array elements ( $f_{hf}[i]$  and  $f_{hf}[i+1]$ ), are mapped to adjacent CUDA threads in the same thread block, to optimize for coalesced memory accesses.

Listing 5.1 OpenACC GPU implementation of the hydrodynamic force computation.

```

1 //OpenACC Kernels copy data between the host and the device
2 #pragma acc kernels
3 copyout(fhf1 [0: nbgrains ], f hf2 [0: nbgrains ], f hf3 [0: nbgrains ])
4 copyin(obst [0:][0:], g [0: nbgrains ], ey [0:], f [0:][0:][0:], ex [0:])
5 //Create individual threads for each DEM grain
6 #pragma acc parallel for
7 for ( i=0; i<nbgrains ;i++) {
8     // Reset hydrodynamic forces to zero at the start of time step
9     f hf1 [ i]=f hf2 [ i]=f hf3 [ i ]=0. ;
10    // Iterate through all lattice nodes
11    for (y=0; y<ly;y++) {
12        for (x=0; x<lx;x++) {
13            if (obst [x ][y]==i) {
14                // generate code to execute the iterations in parallel with
15                // no synchronization
16                #pragma acc for independent
17                for (iLB=1; iLB<Q; iLB++) {
18                    next_x=x+ex[iLB];
19                    next_y=y+ey[iLB];
20                    if (iLB<=half) halfq=half ;
21                    else halfq= -half;

```

```

1   22      if( obst[next_x][next_y]!=i) {
2   23          fnx=(f[x][y][iLB+halfq]+f[next_x][next_y][iLB])*ex[iLB+halfq];
3   24          fny=(f[x][y][iLB+halfq]+f[next_x][next_y][iLB])*ey[iLB+halfq];
4   25          fhf1[i]=fhf1[i]+fnx;
5   26          fhf2[i]=fhf2[i]+fny;
6   27          fhf3[i]=fhf3[i]-fnx*(y-(g[i].x2-wall_bottom_y)/dx)
7   28                  +fny*(x-(g[i].x1-wall_left_x)/dx);
8   29      }
9   30  }
10  31  }
11  32  }
12  33  }
13  34 }
```

Memory transaction optimisation is more important than computation optimisation. Registers do not give rise to any specific problem apart from their limited amount. Global memory, being the only one accessible by both the CPU and the GPU, is the critical path as it suffers from high latency. However, this latency is mostly hidden by the scheduler which stalls inactive warps until data are available. For data intensive LBM, this aspect is generally the limiting factor ([Obrecht and Kuznik, 2011](#)). To optimise the global memory transactions, the memory access is coalesced and aligned, as explained above. The memory transactions between the host and the target through a PCI bus are kept to a minimum.

A two-dimensional fluid – grain system, which consists of 7.2 million LBM nodes and 2500 DEM grains is used to demonstrate the ability of the GPGPU LBM – DEM code. The wall time required to compute 100 iterations of the given LBM – DEM problem is compared for executions running on a single CPU thread, multi-threaded CPU (using OpenMP) and the GPGPU implementations (see table 5.3). The speed-up of parallel implementations are measured against the single CPU thread execution time. OpenMP parallelised multi-threaded CPU execution running on 12 cores achieved a speed-up of 13.5x in comparison to a serial implementation. GPGPU implementation using OpenACC delivered an impressive 126x speed-up in comparison to a single thread CPU execution and about 10 times quicker than a CPU parallel code. In other words, a simulation that would have ordinarily taken 126 days to compute, could now be finished in a day using a GPU.

Scalability is an important criterion when developing high-performance computing codes. Scalability in GPUs is measured in terms of SM utilisation. It is important to distribute sufficient work to all SMs such that on every cycle the warp scheduler has at least one warp eligible to issue instructions. In general, sufficient warps on each SM should be available to

Table 5.3 GPU vs CPU parallelisation

Execution	Computational Time (s)	Speedup
CPU 1 OpenMP thread	2016	–
CPU 2 OpenMP threads	1035	1.5 x
CPU 4 OpenMP threads	660	3.0 x
CPU 12 OpenMP threads	150	13.5 x
GPU OpenACC	16	126.0 x

# Wall time for 100 iteration for 7.2 Million LBM nodes and 2500 DEM grains.

\* CPU OpenMP threads - 6 core Intel Xeon @ 3.3GHz

† GPU threads - GeForce GTX 580 - 512 CUDA cores

hide instruction and memory latency and to provide a variety of instruction types to fill the execution pipeline. Figure 5.17 shows the scalability of GP-GPU implementation as the LBM domain size is increased from 500,000 to 9 million nodes. With increase in LBM nodes the computation time increases linearly with a slope of about 2, which shows that the LBM-DEM implementation algorithm scales with the domain size.

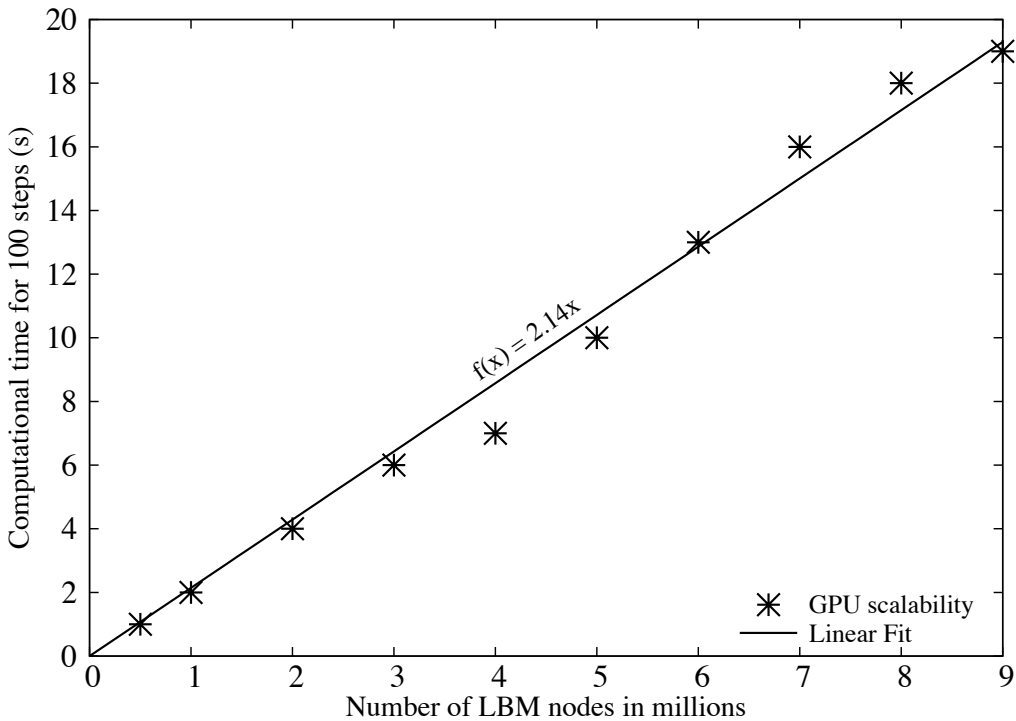


Figure 5.17 GPU scalability with increase in LBM nodes

A two-dimensional coupled LBM-DEM technique is developed to understand the local rheology of granular flows in fluid. The coupled LBM-DEM technique offers the possibility to

1 capture the intricate microscale effects such as the hydrodynamic instabilities. The Smagorinsky  
2 turbulence model is implement in LBM to capture the unsteady flow dynamics in underwater  
3 granular avalanches. The GPGPU implementation of the coupled LBM – DEM technique  
4 offers the capability to model large scale fluid – grain systems, which are otherwise impossible  
5 to model using conventional computation techniques. Efficient data transfer mechanisms that  
6 achieves coalesced global memory ensures that the GPGPU implementation scales linearly  
7 with the domain size.

# Chapter 6

## Underwater granular flows

### 6.1 Submarine granular flows down incline plane

The flow of dense granular material is a common phenomenon in engineering predictions, such as avalanches, landslides, and debris-flow modelling. Despite the huge amount of research that has gone into describing the behaviour of granular flows, a constitutive equation that describes the overall behaviour of a flowing granular material is still lacking. The initiation and propagation of submarine granular flows depend mainly on the slope, density, and quantity of the material destabilised. Although certain macroscopic models are able to capture the simple mechanical behaviours, the complex physical mechanisms that occur at the grain scale, such as hydrodynamic instabilities, the formation of clusters, collapse, and transport, have largely been ignored (Topin et al., 2011). The momentum transfer between the discrete and the continuous phases significantly affects the dynamics of the flow (Peker and Helvacı, 2007). Grain-scale description of the granular material enriches the macro-scale variables, which poorly account for the local rheology of the materials. In order to describe the mechanism of saturated and/or immersed granular flows, it is important to consider both the dynamics of the solid phase and the role of the ambient fluid (Denlinger and Iverson, 2001). In particular, when the solid phase reaches a high volume fraction, it is important to consider the strong heterogeneity arising from the contact forces between the grains, the drag interactions which counteract the movement of the grains, and the hydrodynamic forces that reduce the weight of the solids inducing a transition from dense compacted to a dense suspended flow (Meruane et al., 2010). The case of the collapse in presence of an interstitial fluid has been less studied. In this paper, we study the submarine granular flows in the inclined configuration. We study the effect of permeability, density and slope angle on the run-out evolution.

In this study, a 2D poly-disperse system ( $d_{max}/d_{min} = 1.8$ ) of circular discs in fluid was used to understand the behaviour of granular flows on inclined planes (see Figure 6.1). The soil

1 column was modelled using 1000 discs of density  $2650 \text{ kg m}^{-3}$  and a contact friction angle of  
 2  $26^\circ$ . The collapse of the column was simulated inside a fluid with a density of  $1000 \text{ kg m}^{-3}$  and  
 3 a kinematic viscosity of  $1 \times 10^{-6} \text{ m}^2 \text{ s}^{-1}$ . The choice of a 2D geometry has the advantage of  
 4 cheaper computational effort than a 3D case, making it feasible to simulate very large systems.  
 5 A granular column of aspect ratio ‘a’ of 0.8 was used. A hydrodynamic radius  $r = 0.9R$  was  
 6 adopted during the LBM computations. Dry analyses were also performed to study the effect  
 7 of hydrodynamic forces on the run-out distance.

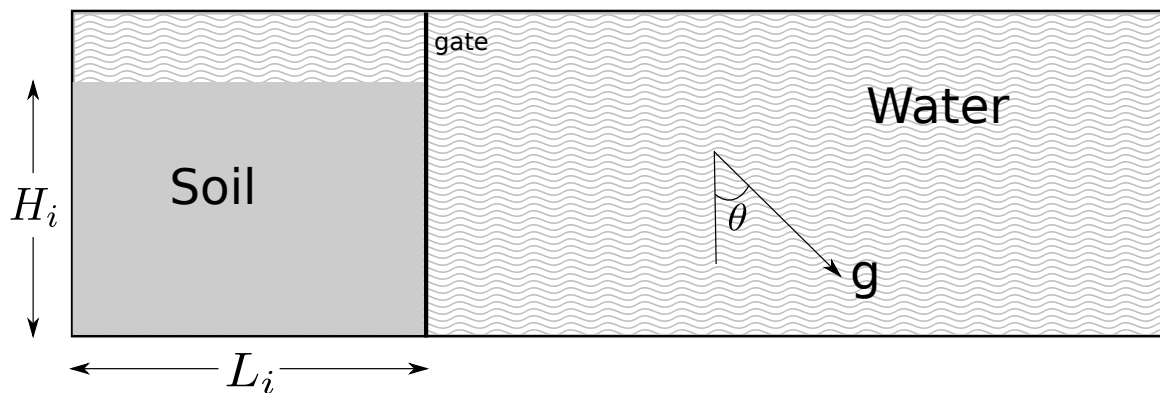


Figure 6.1 Underwater granular collapse set-up

### 8 6.1.1 Effect of initial density

9 The morphology of the granular deposits in fluid is shown to be mainly controlled by the initial  
 10 volume fraction of the granular mass and not by the aspect ratio of the column (Pailha et al.,  
 11 2008; Rondon et al., 2011). In order to understand the influence of the initial packing density  
 12 on the run-out behaviour, a dense sand column (initial packing density,  $\Phi = 83\%$ ) and a loose  
 13 sand column ( $\Phi = 79\%$ ) were used. The granular columns collapse and flow down slopes of  
 14 varying inclinations ( $2.5^\circ$ ,  $5^\circ$  and  $7.5^\circ$ ).

15 The evolution of run-out distances for a dense sand column with time in dry and submerged  
 16 conditions for varying slope inclinations are presented in figure 6.2. The run-out distance  
 17 is longer in submerged condition than the dry condition for a flow on a horizontal surface.  
 18 However, with increase in the slope angle the run-out in the fluid decreases.

19 Dense granular columns in fluid take a longer time to collapse and flow, due to the develop-  
 20 ment of large negative pore-pressure, as the dense granular material dilates during the initial  
 21 phase of the flow. The morphology of dense granular flows down slopes of varying inclinations  
 22 at the critical time ( $t = \tau_c = \sqrt{H/g}$ , when the flow is fully mobilised) are shown in figure 6.4.

23 It can be seen that the viscous drag on the dense column tend to predominate over the  
 24 influence of hydroplaning on the run-out behaviour. This influence can be observed in the

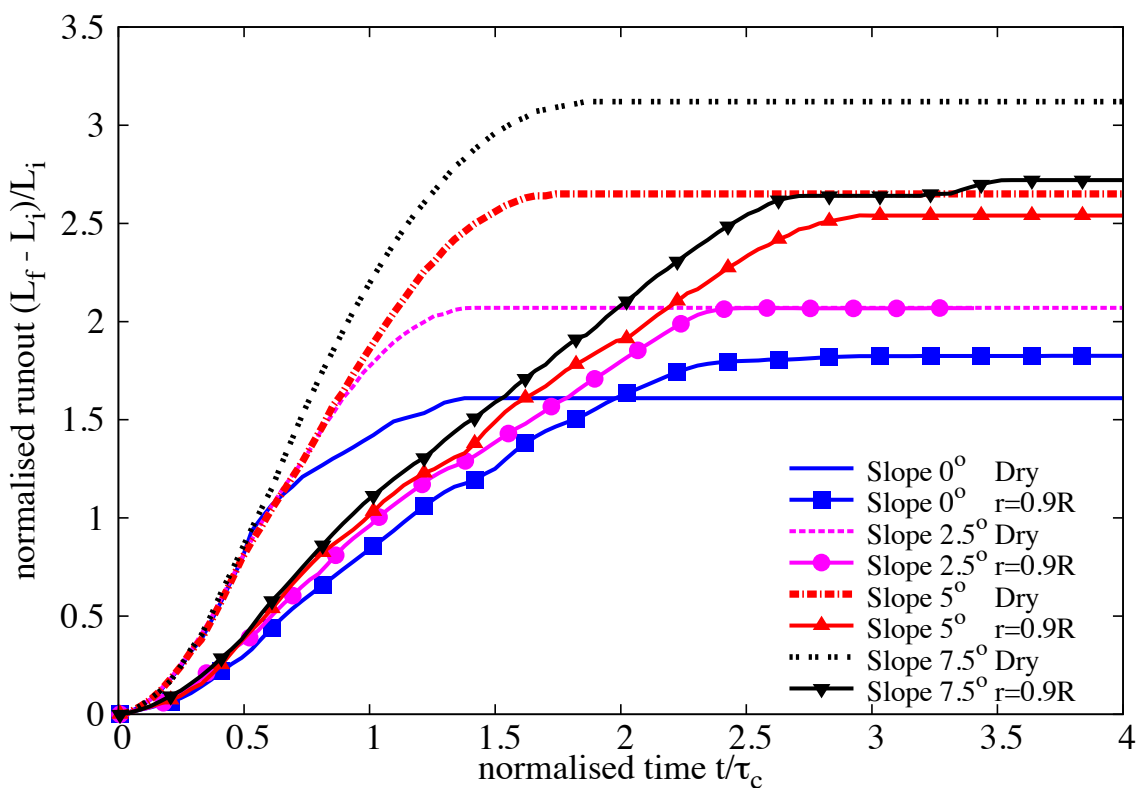


Figure 6.2 Evolution of run-out with time (dense)

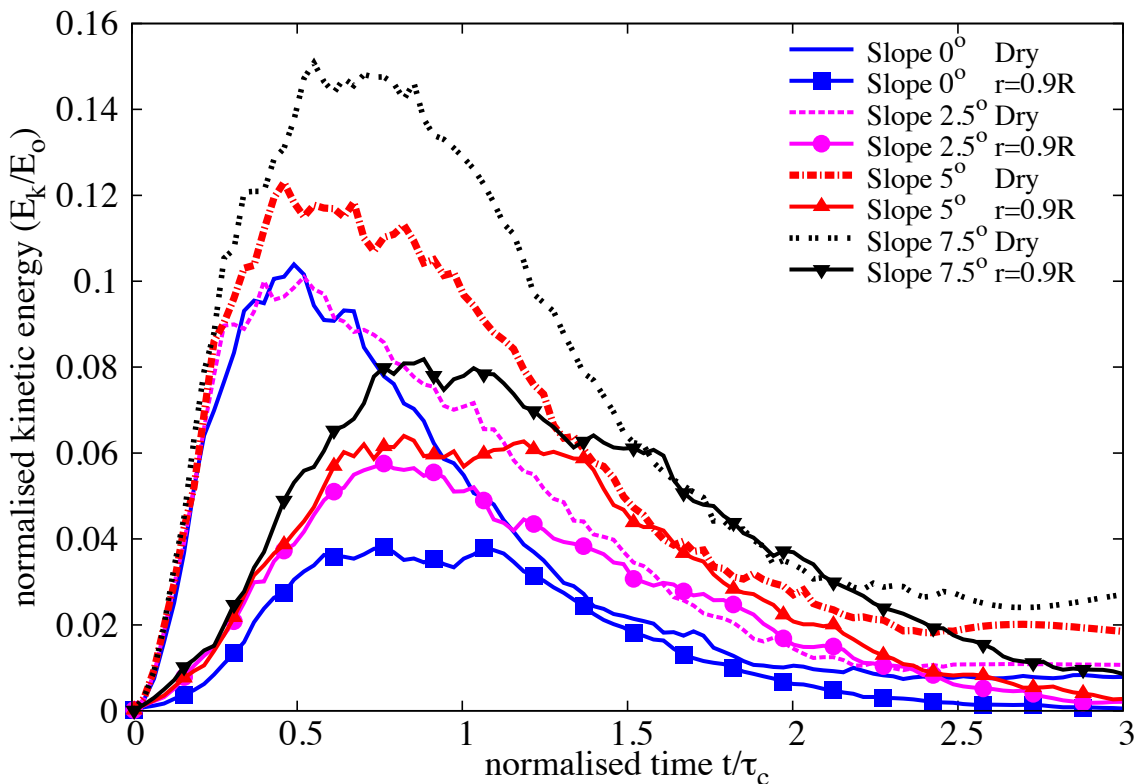
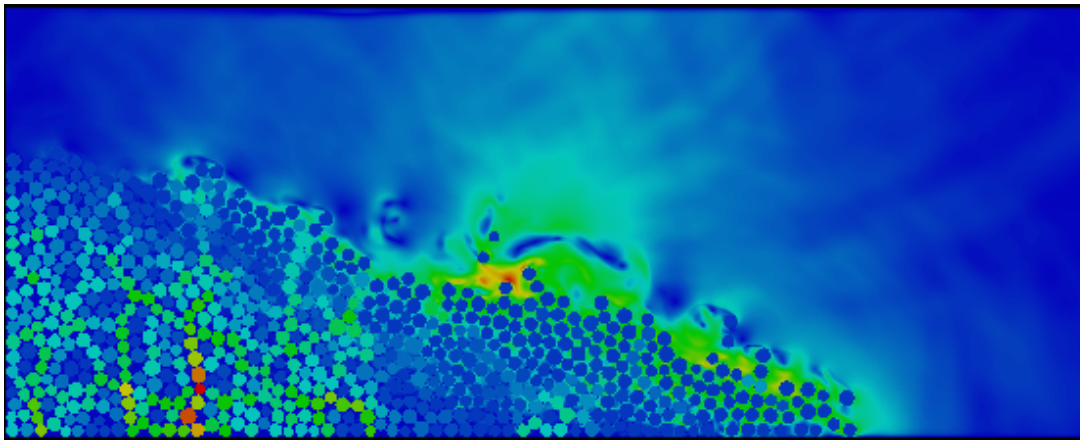


Figure 6.3 Evolution of Kinetic Energy with time (dense case)

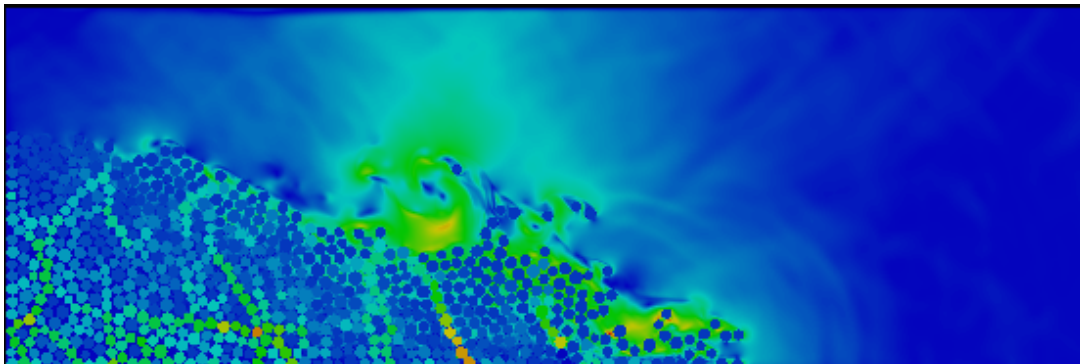
1 smaller peak kinetic energy for granular column in fluid compared to it's dry counterpart  
 2 (see Figure 6.3). With increase in slope angle, the volume of material that dilates increases.  
 3 This results in large negative pore pressures and more viscous drag on the granular material.  
 4 Hence, the difference in the run-out between the dry and the submerged condition, for a dense  
 5 granular assembly, increases with increase in the slope angle.

6 In contrast to the dense granular columns, the loose granular columns (relative density  
 7  $I_D = 30\%$ ) show longer run-out distance in immersed conditions (see Figure 6.5). The run-  
 8 out distance in fluid increases with increase in the slope angle compared to the dry cases.  
 9 Loose granular material tends to entrain more water at the base of the flow front, creating a  
 10 lubricating surface, which causes longer run-out distance (see Figure 6.6). The hydroplaning  
 11 effect causes an increase in the velocity the loose condition in comparison with the dense  
 12 condition (see Figure 6.7).

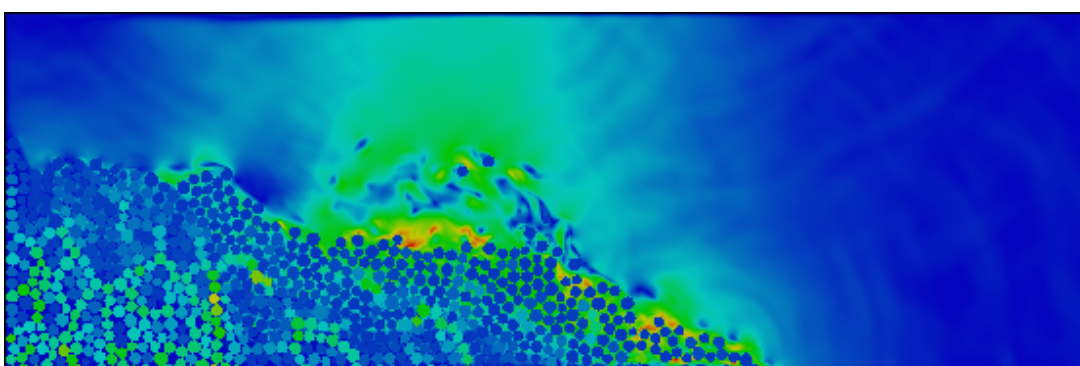
13 The evolution of packing density (see Figure 6.8) shows that dense and the loose conditions  
 14 reach similar packing density. This indicates that the dense granular column dilates more  
 15 and is susceptible to higher viscous drag forces. Whereas in the loose condition, a positive



(a) Slope 2.5



(b) Slope 5.0



(c) Slope 7.5

Figure 6.4 Flow morphology at critical time for different slope angles (dense)

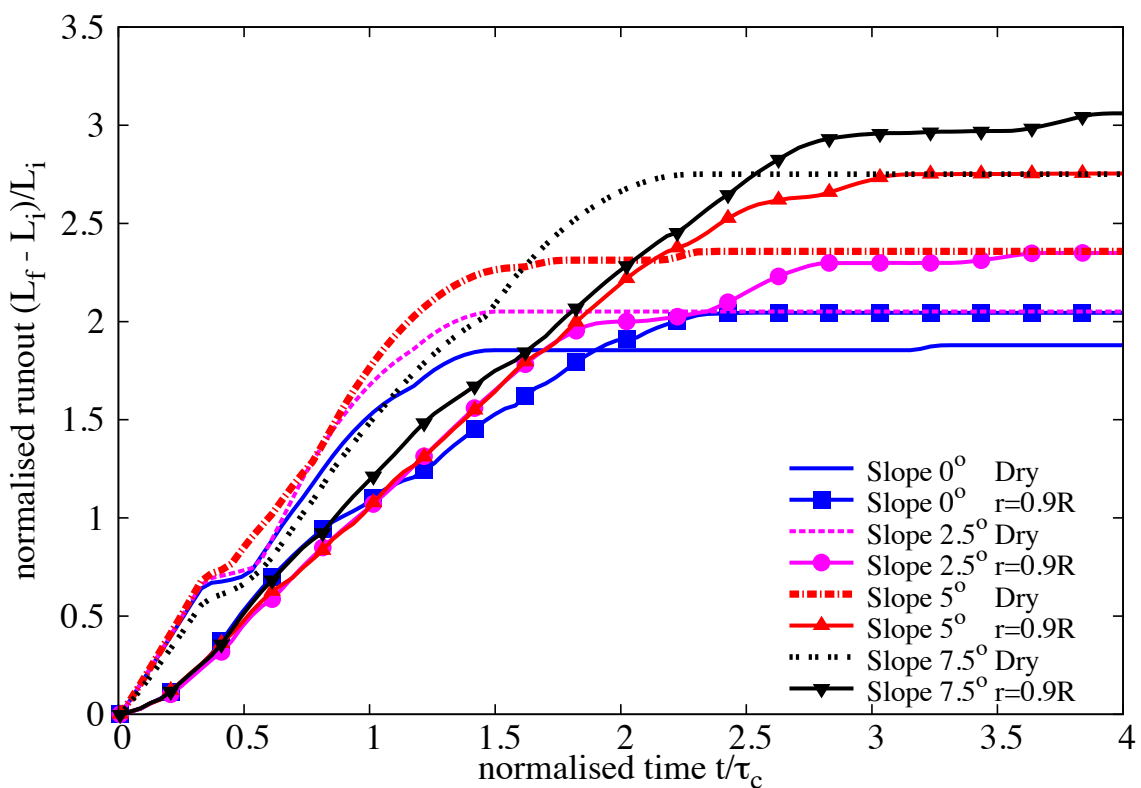
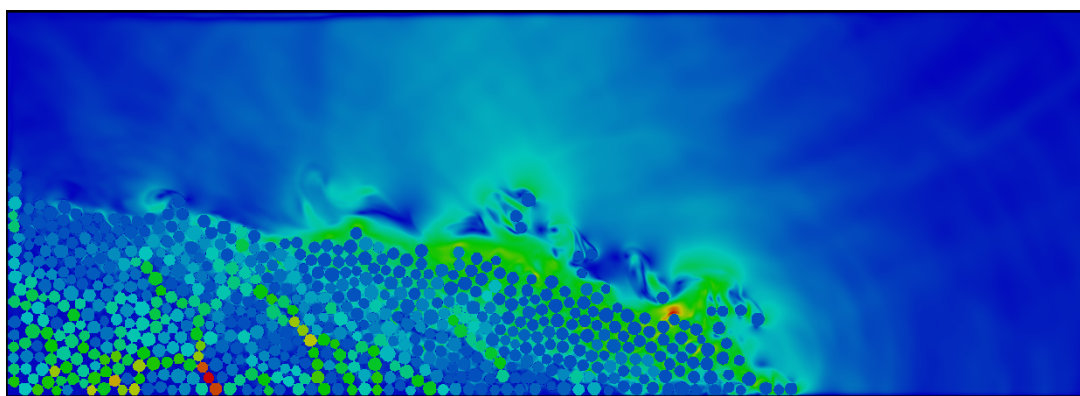
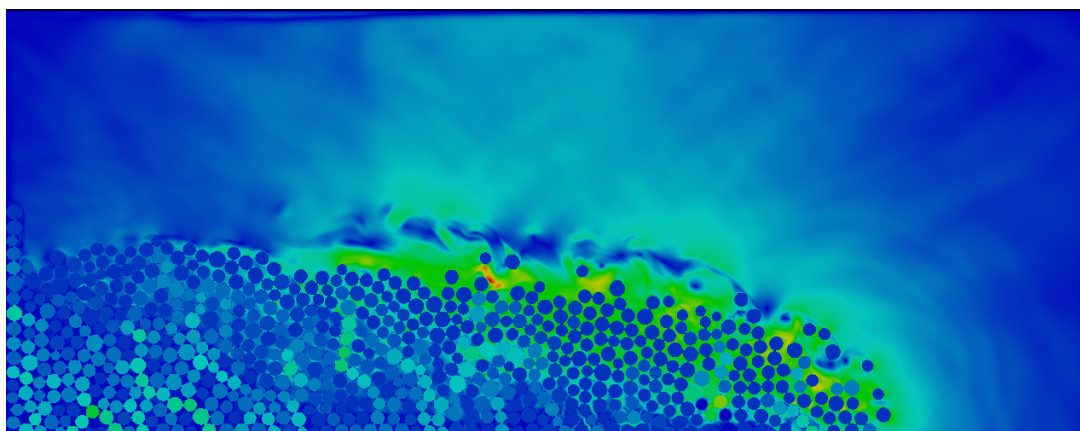


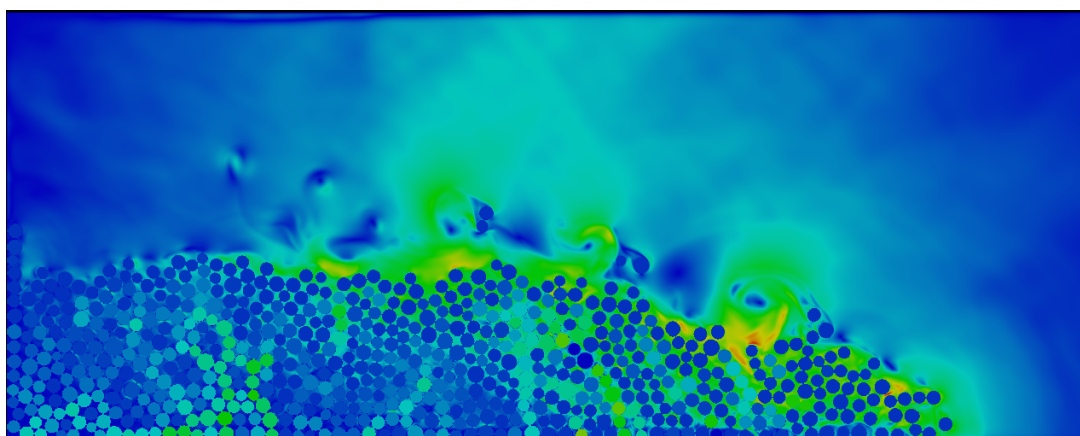
Figure 6.5 Evolution of run-out with time (loose)



(a) Slope 2.5



(b) Slope 5.0



(c) Slope 7.5

Figure 6.6 Flow morphology at critical time for different slope angles (loose)

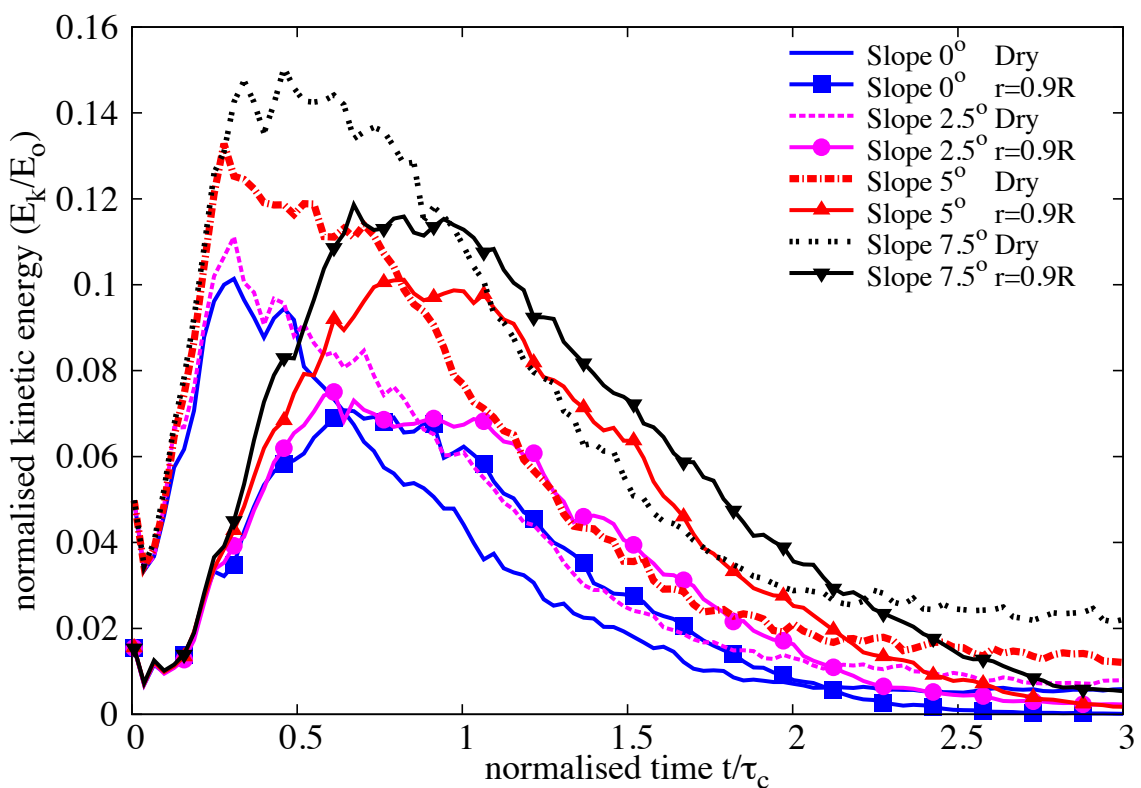


Figure 6.7 Evolution of Kinetic Energy with time (loose)

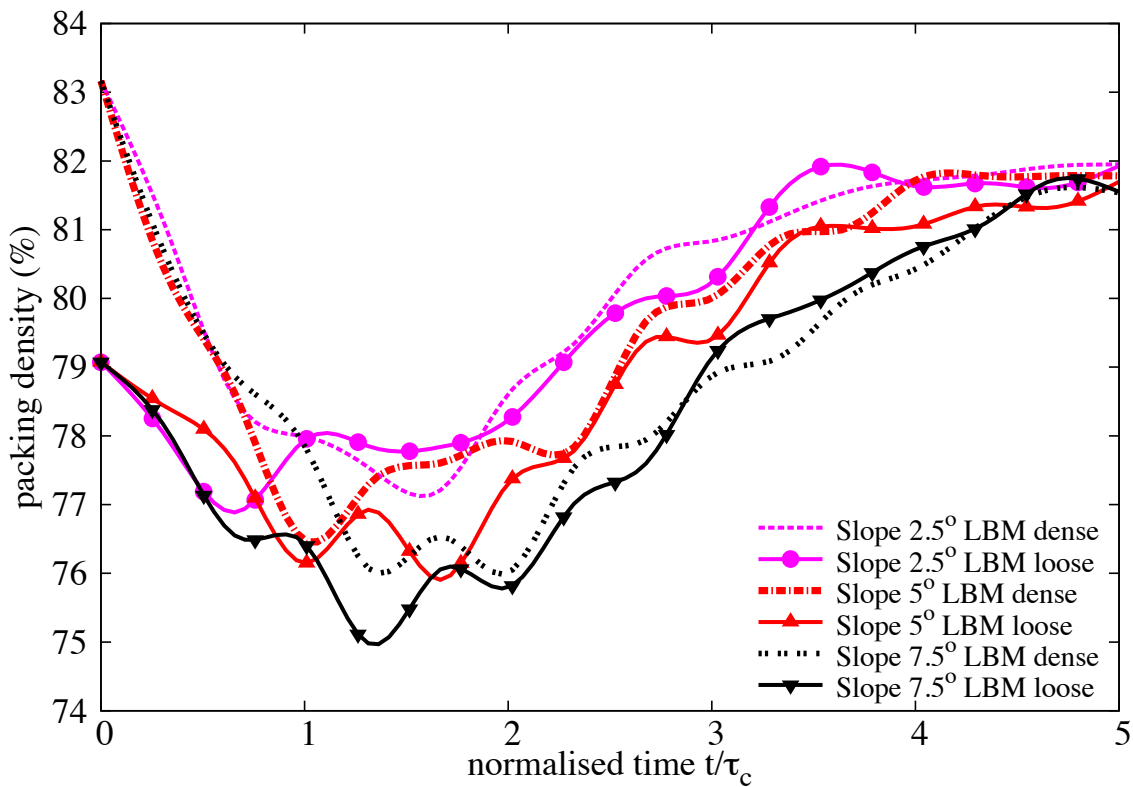


Figure 6.8 Evolution of packing density with time

pore-pressure is observed at the base of the flow, indicating entrainment of water at the base,  
i.e. hydroplaning resulting in longer run-out distance.

### 6.1.2 Effect of permeability

In DEM, the grain – grain interaction is described based on the overlap between the grains at the contact surface. In a 3D granular assembly, the pore spaces between grains are interconnected. Whereas in a 2-D assembly, the grains are in contact with each other that result in a non-interconnected pore-fluid space. This causes a no flow condition in a 2-D case. In order to overcome this difficulty, a reduction in radius is assumed only during the LBM computation phase (fluid and fluid – solid interaction). The reduction in radius allows interconnected pore space through which the surrounding fluid can flow. This technique has no effect on the grain – grain interactions computed using DEM. See Kumar et al. (2012) for more details about the relationship between reduction in radius and permeability of the granular assembly.

For a slope angle of 5°, the hydrodynamic radius of the loosely packed grains was varied from  $r = 0.7R$  (high permeability), 0.75R, 0.8R, 0.85R to 0.9R (low permeability). The run-out distance is found to increase with decrease in the permeability of the granular assembly

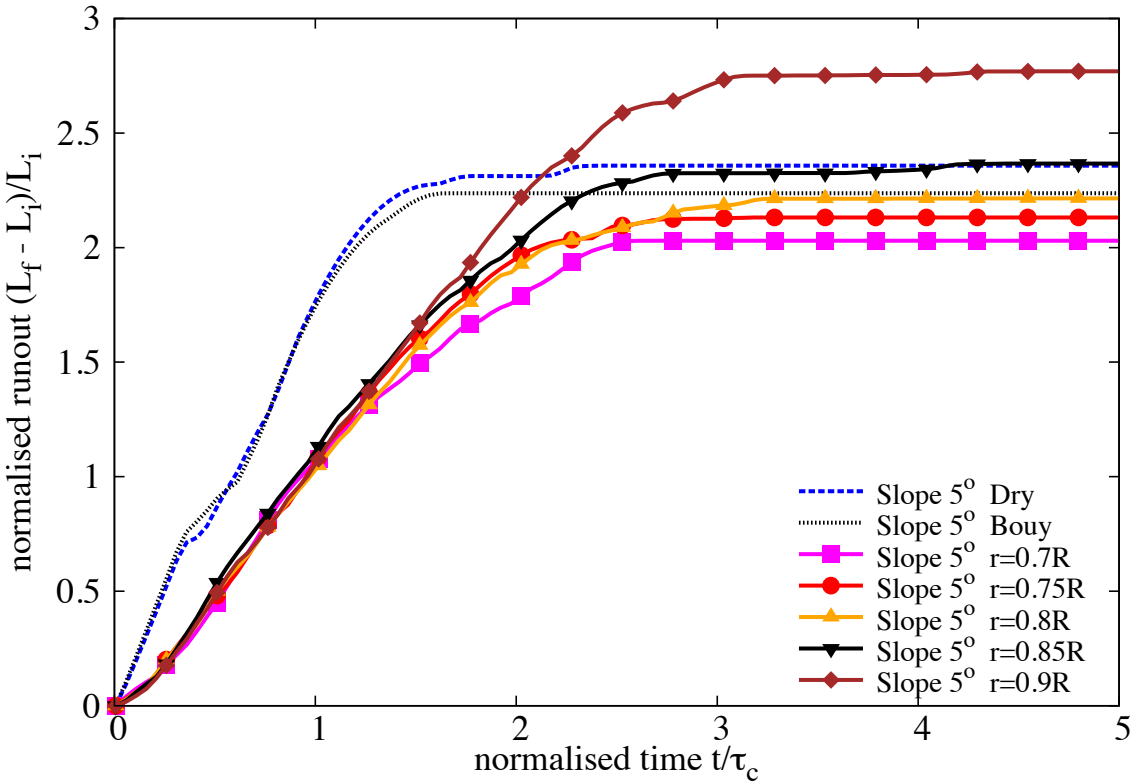


Figure 6.9 Evolution of run-out with time for different permeability (loose slope 5°)

(see Figure 6.9). The run-out distance for high permeable conditions ( $r = 0.7R - 0.8R$ ) were lower than their dry counterparts. Although, decrease in permeability resulted in an increase in the run-out distance, no significant change in the run-out behaviour was observed for a hydrodynamic radius of up to 0.8R.

With further decrease in permeability ( $r = 0.85R$  and  $0.9R$ ), the run-out distance in the fluid was greater than the run-out observed in the dry condition. At very low permeability ( $r = 0.9R$ ), granular material started to entrain more water at the base, which causes a reduction in the effective stress accompanied by a lubrication effect on the flowing granular media. This can be seen as a significant increase in the peak kinetic energy and the duration of the peak energy, in comparison with dry and high permeable conditions (see Figure 6.11).

The permeability of the granular column did not have an influence on the evolution of height during the flow. However, dry granular column tends to collapse more than the immersed granular column (see Figure 6.10).

Positive pore-pressure generation at the base of the flow was observed for low permeable conditions. Inspection of the local packing density showed entrainment of water at the base of the flow, which can also be observed by the steep decrease in the packing density (see Fig-

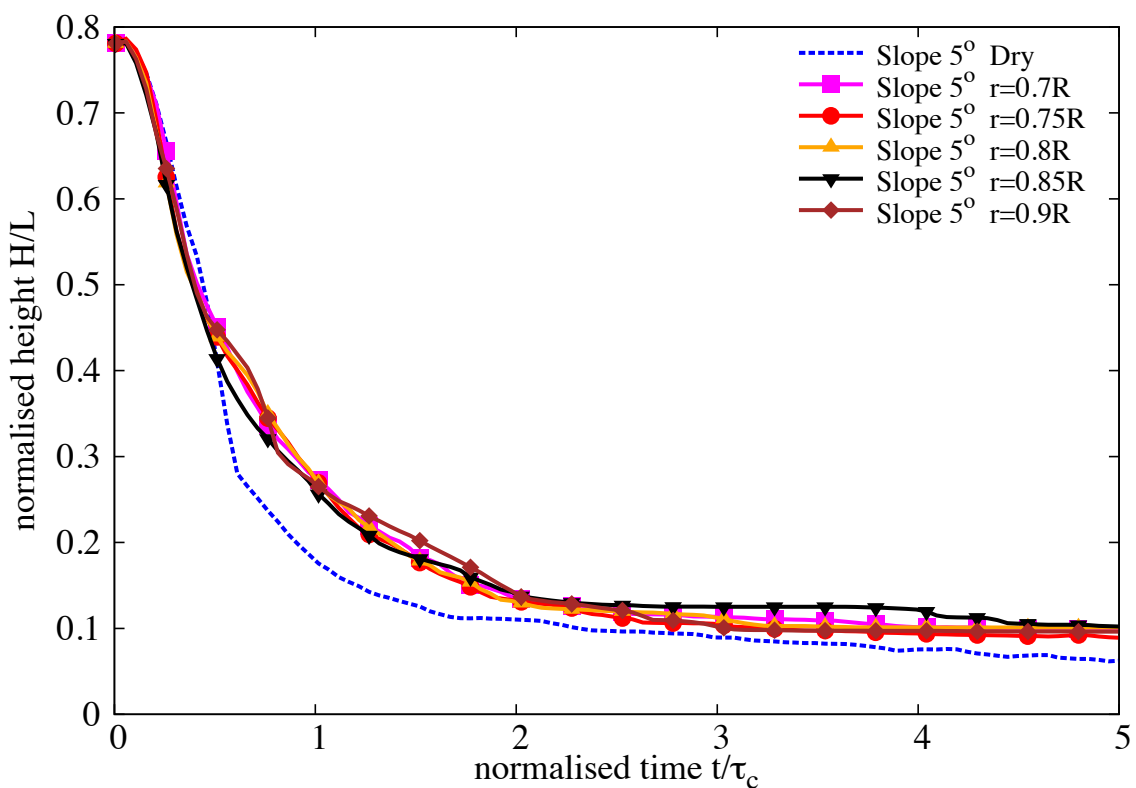


Figure 6.10 Evolution of height with time for different permeability (loose slope 5°)

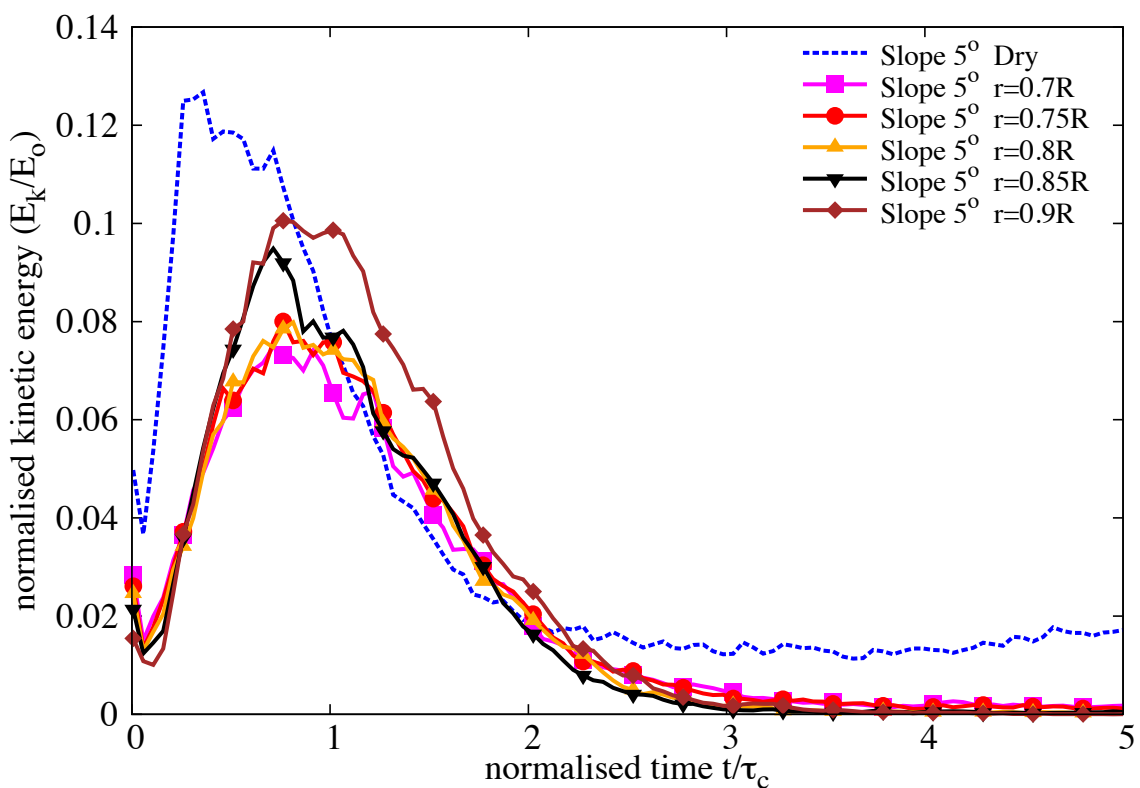


Figure 6.11 Evolution of Kinetic Energy with time for different permeability (loose slope 5°)

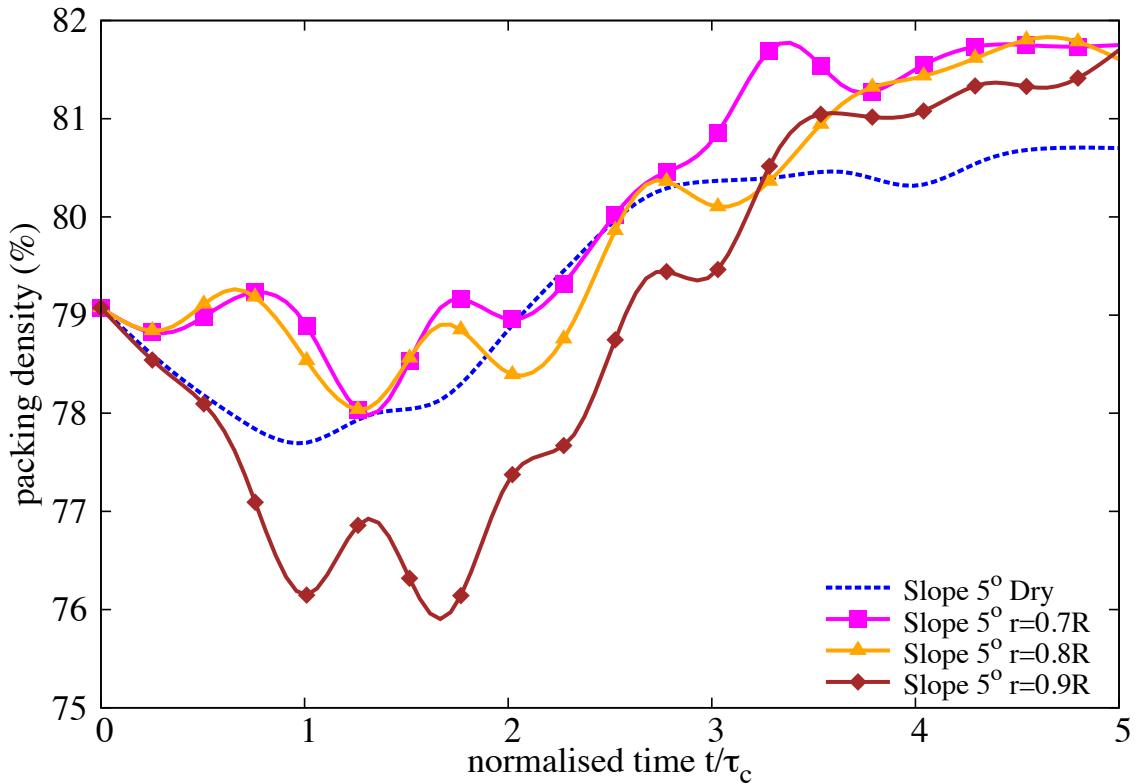


Figure 6.12 Evolution of packing density with time for different permeability (loose slope 5°)

ure 6.12) for the very low permeability condition ( $r = 0.9R$ ). At the end of the flow ( $t \geq 3 \times \tau_c$ ), the excess pore-pressure dissipates and the granular material, irrespective of their permeability, reaches almost the same packing density.

### 6.1.3 Summary

Two-dimensional LB-DEM simulations were performed to understand the behaviour of submarine granular flows. Unlike dry granular collapse, the run-out behaviour in fluid is dictated by the initial volume fraction. Granular columns with loose packing tend to flow longer in comparison to dense columns, due to entrainment of water at the base resulting in lubrication. The loose column when it starts flowing expands and ejects liquid, leading to a partial fluidization of the material. However, with increase in the slope angle, the run-out in fluid is influenced by the viscous drag on the granular materials. The run-out distance in fluid increases with decrease in permeability. More research work is required to characterise the flow behaviour of granular materials, especially in submerged conditions.

Draft - v1.0

Friday 12<sup>th</sup> September, 2014 – 18:12

# References

- Aidun, C., Lu, Y., and Ding, E. (1998). Direct analysis of particulate suspensions with inertia using the discrete Boltzmann equation. *Journal of Fluid Mechanics*, 373(-1):287–311. 1  
2  
3
- Balmforth, N. J. and Kerswell, R. R. (2005). Granular collapse in two dimensions. *Journal of Fluid Mechanics*, 538:399–428. 4  
5
- Bandara, S. (2013). *Material Point Method to simulate Large Deformation Problems in Fluid-saturated Granular Medium*. PhD thesis, University of Cambridge. 6  
7
- Bathe, K. and Zhang, H. (2004). Finite element developments for general fluid flows with structural interactions. *International Journal for Numerical Methods in Engineering*, 60(1):213–232. 8  
9  
10
- Breuer, M., Bernsdorf, J., Zeiser, T., and Durst, F. (2000). Accurate computations of the laminar flow past a square cylinder based on two different methods: lattice-Boltzmann and finite-volume. *Journal of Heat and Fluid Flow*, 21(2):186–196. 11  
12  
13
- Capecelatro, J. and Desjardins, O. (2013). An Euler–Lagrange strategy for simulating particle-laden flows. *Journal of Computational Physics*, 238(0):1–31. 14  
15
- Chen, S. and Doolen, G. G. D. (1998). Lattice Boltzmann method for fluid flows. *Annual review of fluid mechanics*, 30(1):329–364. 16  
17
- Cook, B., Noble, D., and Williams, J. (2004). A direct simulation method for particle-fluid systems. *Engineering Computations*, 21(2/3/4):151–168. 18  
19
- Daerr, A. and Douady, S. (1999). Two types of avalanche behaviour in granular media. *Nature*, 399(6733):241–243. 20  
21
- Denlinger, R. and Iverson, R. (2001). Flow of variably fluidized granular masses across three-dimensional terrain, ii: Numerical predictions and experimental tests. *J. Geophys. Res.*, 106(B1):553–566. 22  
23  
24
- Du, R., Shi, B., and Chen, X. (2006). Multi-relaxation-time lattice Boltzmann model for incompressible flow. *Physics Letters A*, 359(6):564–572. 25  
26
- Durst, F., Ray, S., Unsal, B., and Bayoumi, O. (2005). The development lengths of laminar pipe and channel flows. *Journal of fluids engineering*, 127:1154. 27  
28
- Estrada, N., Taboada, A., and Radjai, F. (2008). Shear strength and force transmission in granular media with rolling resistance. *Physical Review E*, 78(2):021301. 29  
30

- <sup>1</sup> Feng, Y. T., Han, K., and Owen, D. R. J. (2007). Coupled lattice Boltzmann method and discrete element modelling of particle transport in turbulent fluid flows: Computational issues. *International Journal for Numerical Methods in Engineering*, 72(9):1111–1134.
- <sup>4</sup> Fortes, A. (1987). Nonlinear mechanics of fluidization of beds of spherical particles. *Journal of Fluid Mechanics*.
- <sup>6</sup> Frisch, U. and Kolmogorov, A. (1995). *Turbulence: the legacy of AN Kolmogorov*. Cambridge University Press.
- <sup>8</sup> Guilkey, J., Harman, T., Xia, A., Kashiwa, B., and McMurtry, P. (2003). An Eulerian-Lagrangian approach for large deformation fluid structure interaction problems, Part 1: algorithm development. *Advances in Fluid Mechanics*, 36:143–156.
- <sup>11</sup> Han, K., Feng, Y., and Owen, D. (2007a). Coupled lattice Boltzmann and discrete element modelling of fluid-particle interaction problems. *Computers & Structures*, 85(11-14):1080–1088.
- <sup>14</sup> Han, S., Zhu, P., and Lin, Z. (2007b). Two-dimensional interpolation-supplemented and Taylor-series expansion-based lattice Boltzmann method and its application. . . . in *Nonlinear Science and Numerical Simulation*, 12(7):1162–1171.
- <sup>17</sup> He, X. and Luo, L. L.-S. (1997a). Theory of the lattice Boltzmann method: From the Boltzmann equation to the lattice Boltzmann equation. *Physical Review E*, 56(6):6811.
- <sup>19</sup> He, X. and Luo, L.-S. (1997b). A priori derivation of the lattice Boltzmann equation. *Physical Review E*, 55(6):R6333–R6336.
- <sup>21</sup> He, X., Zou, Q., Luo, L. S., and Dembo, M. (1997). Analytic solutions of simple flows and analysis of nonslip boundary conditions for the lattice Boltzmann BGK model. *Journal of Statistical Physics*, 87(1):115–136.
- <sup>24</sup> Iglberger, K., Thurey, N., and Rude, U. (2008). Simulation of moving particles in 3D with the Lattice Boltzmann method. *Computers & Mathematics with Applications*, 55(7):1461–1468.
- <sup>26</sup> Jean, M. (1999). The non-smooth contact dynamics method. *Computer Methods in Applied Mechanics and Engineering*, 177(3-4):235–257.
- <sup>28</sup> Komiwas, V., Mege, P., Meimon, Y., and Herrmann, H. (2005). Simulation of granular flow in a fluid applied to sedimentation. *Granular Matter*, 8(1):41–54.
- <sup>30</sup> Kumar, K., Soga, K., and Delenne, J.-Y. (2012). *Discrete Element Modelling of Particulate Media*. Special Publication. Royal Society of Chemistry, Cambridge.
- <sup>32</sup> Lacaze, L. and Kerswell, R. R. (2009). Axisymmetric Granular Collapse: A Transient 3D Flow Test of Viscoplasticity. *Physical Review Letters*, 102(10):108305.
- <sup>34</sup> Ladd, A. J. (1994). Numerical simulations of particulate suspensions via a discretized Boltzmann equation. Part 1. Theoretical foundation. *Journal of Fluid Mechanics*, 271:285–309.
- <sup>36</sup> Ladd, A. J. C. and Verberg, R. (2001). Lattice-Boltzmann Simulations of Particle-Fluid Suspensions. *Journal of Statistical Physics*, 104(5):1191–1251.

- Lajeunesse, E., Mangeney-Castelnau, A., and Vilotte, J. P. (2004). Spreading of a granular mass on a horizontal plane. *Physics of Fluids*, 16(7):2371. 1  
2
- Liu, S. H., Sun, D. A., and Wang, Y. (2003). Numerical study of soil collapse behavior by discrete element modelling. *Computers and Geotechnics*, 30(Compindex):399–408. 3  
4
- Lube, G., Huppert, H. E., Sparks, R. S. J., and Freundt, A. (2005). Collapses of two-dimensional granular columns. *Physical Review E - Statistical, Nonlinear, and Soft Matter Physics*, 72(4):1–10. 5  
6  
7
- Mei, R., Shyy, W., Yu, D., and Luo, L.-S. (2000). Lattice Boltzmann Method for 3-D Flows with Curved Boundary. *Journal of Computational Physics*, 161(2):680–699. 8  
9
- Meruane, C., Tamburrino, A., and Roche, O. (2010). On the role of the ambient fluid on gravitational granular flow dynamics. *Journal of Fluid Mechanics*, 648:381–404. 10  
11
- Moreau, J. J. (1993). New computation methods in granular dynamics. In *Powders & Grains 93*, page 227, Rotterdam. A. A. Balkema. 12  
13
- Noble, D. and Torczynski, J. (1998). A lattice-Boltzmann method for partially saturated computational cells. *International Journal of Modern Physics C-Physics and Computer*, 9(8):1189–1202. 14  
15  
16
- Obrecht, C. and Kuznik, F. (2011). A new approach to the lattice Boltzmann method for graphics processing units. *Computers & Mathematics* .... 17  
18
- Oda, M. and Iwashita, K. (1999). *Mechanics of granular materials: an introduction*. Taylor & Francis. 19  
20
- OpenACC-Members (2013). The OpenACC Application Programming Interface Version 2.0 (June, 2013; Corrected: August, 2013). Technical report, OpenMP Standard Group. 21  
22
- Pailha, M., Pouliquen, O., and Nicolas, M. (2008). Initiation of Submarine Granular Avalanches: Role of the Initial Volume Fraction. *AIP Conference Proceedings*, 1027(1):935–937. 23  
24
- Pan, C., Luo, L., and Miller, C. (2006). An evaluation of lattice Boltzmann schemes for porous medium flow simulation. *Computers & fluids*, 35(8-9):898–909. 25  
26
- Peker, S. and Helvacı, S. (2007). *Solid-liquid two phase flow*. Elsevier. 27
- Radjai, F. and Dubois, F. (2011). *Discrete-element modeling of granular materials*. ISTE Wiley, London; Hoboken, N.J. 28  
29
- Radjai, F. and Richéfeu, V. (2009). Contact dynamics as a nonsmooth discrete element method. *Mechanics of Materials*, 41(6):715–728. 30  
31
- Rondon, L., Pouliquen, O., and Aussillous, P. (2011). Granular collapse in a fluid: Role of the initial volume fraction. *Physics of Fluids*, 23(7):073301–073301–7. 32  
33
- Schaefer, D. G. (1990). Instability and ill-posedness in the deformation of granular materials. *International Journal for Numerical and Analytical Methods in Geomechanics*, 14(4):253–278. 34  
35  
36

- <sup>1</sup> Smagorinsky, J. (1963). General circulation experiments with the primitive equations. *Monthly weather review*, 91(3):99–164.
- <sup>3</sup> Staron, L., Radjai, F., and Vilotte, J. P. (2005). Multi-scale analysis of the stress state in a granular slope in transition to failure. *The European physical journal. E, Soft matter*, 18(3):311–20.
- <sup>6</sup> Succi, S. (2001). *The lattice Boltzmann equation for fluid dynamics and beyond*. Oxford University Press.
- <sup>8</sup> Succi, S., Foti, E., and Higuera, F. (1989). Three-Dimensional Flows in Complex Geometries with the Lattice Boltzmann Method. *Europhysics Letters (EPL)*, 10(5):433–438.
- <sup>10</sup> Sukop, M. and Thorne, D. (2006). *Lattice Boltzmann modeling: An introduction for geoscientists and engineers*. Springer Verlag.
- <sup>12</sup> Sun, X., Sakai, M., and Yamada, Y. (2013). Three-dimensional simulation of a solid–liquid flow by the DEM–SPH method. *Journal of Computational Physics*, 248(0):147–176.
- <sup>14</sup> Topin, V., Dubois, F., Monerie, Y., Perales, F., and Wachs, A. (2011). Micro-rheology of dense particulate flows: Application to immersed avalanches. *Journal of Non-Newtonian Fluid Mechanics*, 166(1-2):63–72.
- <sup>17</sup> Topin, V., Monerie, Y., Perales, F., and Radjaï, F. (2012). Collapse Dynamics and Runout of Dense Granular Materials in a Fluid. *Physical Review Letters*, 109(18):188001.
- <sup>19</sup> Wang, L., Guo, Z., and Mi, J. (2014). Drafting, kissing and tumbling process of two particles with different sizes. *Computers & Fluids*.
- <sup>21</sup> Willis, A., Peixinho, J., Kerswell, R., and Mullin, T. (2008). Experimental and theoretical progress in pipe flow transition. *Philosophical Transactions of the Royal Society A: Mathematical, Physical and Engineering Sciences*, 366(1876):2671.
- <sup>24</sup> Wolfe, M. (2012). PGInsider August 2012: OpenACC Kernels and Parallel Constructs.
- <sup>25</sup> Xiong, Q., Madadi-Kandjani, E., and Lorenzini, G. (2014). A LBM–DEM solver for fast discrete particle simulation of particle–fluid flows. *Continuum Mechanics and Thermodynamics*.
- <sup>28</sup> Yu, D., Mei, R., Luo, L., and Shyy, W. (2003). Viscous flow computations with the method of Lattice Boltzmann equation. *Progress in Aerospace Sciences*, 39(5):329–367.
- <sup>30</sup> Yu, H., Girimaji, S., and Luo, L. (2005). Lattice Boltzmann simulations of decaying homogeneous isotropic turbulence. *Physical Review E*, 71(1):016708.
- <sup>32</sup> Zhong, Q. and Olson, M. (1991). Finite element–algebraic closure analysis of turbulent separated-reattaching flow around a rectangular body. *Computer methods in applied mechanics and engineering*, 85(2):131–150.
- <sup>35</sup> Zhou, H., Mo, G., Wu, F., Zhao, J., Rui, M., and Cen, K. (2012). GPU implementation of lattice Boltzmann method for flows with curved boundaries. *Computer Methods in Applied Mechanics and Engineering*, 225-228(null):65–73.

Ziegler, D. (1993). Boundary conditions for Lattice Boltzmann simulations. *Journal of Statistical Physics*, 71(5):1171–1177. 1  
2

Zou, Q. and He, X. (1997). On pressure and velocity boundary conditions for the Lattice Boltzmann BGK model. *Physics of Fluids*, 9(6):1591–1598. 3  
4